

The P2 Experiment

A future high-precision measurement of the electroweak mixing angle at low momentum transfer

Dominik Becker^{1,2}, Razvan Bucoveanu^{1,3}, Carsten Grzesik^{1,2}, Kathrin Imai^{1,2}, Ruth Kempf^{1,2}, Matthias Molitor^{1,2}, Alexey Tyukin^{1,2}, Marco Zimmermann^{1,2}, David Armstrong⁴, Kurt Aulenbacher^{1,2,5}, Sebastian Baunack^{1,2}, Rakitha Beminiwatha⁶, Niklaus Berger^{1,2}, Peter Bernhard^{1,7}, Andrea Brogna^{1,7}, Luigi Capozza^{1,2,5}, Silviu Covrig Dusa⁸, Wouter Deconinck⁴, Jürgen Diefenbach^{1,2}, James Dunne⁹, Jens Erler¹⁰, Ciprian Gal¹¹, Michael Gericke¹², Boris Gläser^{1,2}, Mikhail Gorchtein^{1,2}, Boxing Gou^{1,2,5}, Wolfgang Gradl^{1,2}, Yoshio Imai^{1,2}, Krishna S. Kumar¹³, Frank Maas^{1,2,5,a}, Juliette Mammei¹², Jie Pan¹², Preeti Pandey¹², Kent Paschke¹¹, Ivan Perić¹⁴, Mark Pitt¹⁵, Sakib Rahman¹², Seamus Riordan¹⁶, David Rodríguez Piñeiro^{1,2,5}, Concettina Sfienti^{1,2,5,7}, Iurii Sorokin^{1,2}, Paul Souder¹⁷, Hubert Spiesberger^{1,3}, Michaela Thiel^{1,2}, Valery Tyukin^{1,2}, and Quirin Weitzel^{1,7}

¹ PRISMA Cluster of Excellence, Johannes Gutenberg-Universität Mainz, Germany

² Institute of Nuclear Physics, Johannes Gutenberg-Universität Mainz, Germany

³ Institute of Physics, Johannes Gutenberg-Universität, Mainz, Germany

⁴ College of William and Mary, Williamsburg, Virginia, USA

⁵ Helmholtz Institute Mainz, Johannes Gutenberg-Universität Mainz, Germany

⁶ Louisiana Tech University, Ruston, Louisiana, USA

⁷ Detector Laboratory, PRISMA Cluster of Excellence, Johannes Gutenberg-Universität Mainz, Germany

⁸ Thomas Jefferson National Accelerator Facility, Newport News, Virginia, USA

⁹ Mississippi State University, Mississippi State, MS, USA

¹⁰ Departamento de Física Teórica, Instituto de Física, Universidad Nacional Autónoma de México, CDMX, México

¹¹ University of Virginia, Charlottesville, Virginia, USA

¹² Department of Physics and Astronomy, University of Manitoba, Winnipeg, Canada

¹³ Department of Physics and Astronomy, Stony Brook University, Stony Brook, USA

¹⁴ Institute for Data Processing and Electronics, Karlsruhe Institute of Technology, Karlsruhe, Germany

¹⁵ Virginia Tech University, Blacksburg, Virginia, USA

¹⁶ Physics Division, Argonne National Laboratory, Argonne, USA

¹⁷ Physics Department, Syracuse University, Syracuse, USA

Received: date / Revised version: date

Abstract. This article describes the research and development work for the future P2 experimental facility at the upcoming MESA accelerator in Mainz. The facility is optimized for the detection of order 10^{-8} parity-violating cross section asymmetries in electron scattering. The physics program of the facility comprises indirect, high precision search for physics beyond the Standard Model, measurement of the neutron distribution in nuclear physics, single-spin asymmetries stemming from two-photon exchange and a possible future extension to the measurement of hadronic parity violation.

The first measurement of the P2 experiment for which the research and development work is most advanced is described here in detail. It aims for a high precision determination of the weak mixing angle $\sin^2 \theta_W$ to a precision of 0.14% at a four-momentum transfer of $Q^2 = 4.5 \times 10^{-3} \text{ GeV}^2$. The accuracy is comparable to existing measurements at the Z pole. It comprises a sensitive test of the standard model up to a mass scale of 50 TeV, extendable to 60 TeV. This requires a measurement of the parity violating cross section asymmetry $\langle A^{\text{exp}} \rangle = -39.94 \times 10^{-9}$ in the elastic electron-proton scattering with a total accuracy of $\Delta \langle A^{\text{exp}} \rangle_{\text{Total}} = 0.56 \times 10^{-9}$ (1.4%) in 10 000 h of 150 μA polarized electron beam impinging on a 60 cm ℓH_2 target allowing for an extraction of the weak charge of the proton which is directly connected to the weak mixing angle $\sin^2 \theta_W$. Contributions from γZ -box graphs become small at the small beam energy of $E_{\text{beam}} = 155 \text{ MeV}$.

The P2 asymmetry is smaller than any asymmetry measured so far in electron scattering with an unprecedented goal for the accuracy. The use of a solenoid-spectrometer with 100% ϕ -acceptance as well as an atomic H trap polarimeter are some new features, which have never before been used in parity-violation experiments, and which we describe among others, here. In order to collect the enormous statistics required for this measurement, the new Mainz Energy Recovery Superconducting Accelerator (MESA) is under construction. The plans on the associated beam control system and the polarimetry is described in this article as well. A new ℓH_2 high-power target design with an enormously low noise level of 10 ppm needs to be constructed. We report here in addition on the conceptual design of the P2 spectrometer, its Cherenkov detectors, the integrating read-out electronics as well as the ultra-thin, fast tracking detectors. There has been substantial theory work done in preparation of the determination of $\sin^2 \theta_W$. The further physics program in particle and nuclear physics is described here as well.

PACS. 11.30.Er Charge conjugation, parity, time reversal, and other discrete symmetries – 12.15.Lk Electroweak radiative corrections – 13.85.Dz Elastic scattering – 13.88.+e Polarization in interactions and scattering – 25.30.Bf Elastic electron scattering – 29.20.Ej Linear accelerators – 29.27.Hj Polarized beams – 29.40.Gx Tracking and position-sensitive detectors – 29.40.Ka Cherenkov detectors

Contents

| | | |
|---|---|----|
| 1 | Introduction and physics motivation | 2 |
| 2 | Determining the Weak Mixing Angle from Parity Violating Electron Scattering | 4 |
| 3 | The MESA Accelerator | 10 |
| 4 | High Power Liquid Hydrogen Target | 20 |
| 5 | The P2 Spectrometer | 25 |
| 6 | Theory input | 48 |
| 7 | Further physics programme | 51 |
| 8 | Conclusions and Outlook | 57 |
| 9 | Acknowledgements | 58 |
| A | Nucleon form factor fit parameters | 58 |

1 Introduction and physics motivation

In the Standard Model of Elementary Particle Physics (SM) the weak interaction is the only force that violates parity. Over the past 30 years, the measurement of parity violation in weak interactions has been a well established experimental technique in atomic as well as particle and nuclear physics. The violation of parity had been postulated by the theoreticians Lee & Yang in 1956 [1]. It was proven to be an experimental fact in nuclear physics in 1957 in the course of the Wu experiment [2] by a careful analysis of the beta-decay of ^{60}Co . In addition Garwin, Lederman and Weinrich had shown that the μ -decay violates parity [3]. As first pointed out by Zeldovich in 1959 [4], the existence of a neutral partner of the charged weak interaction responsible for β -decay, should lead to observable parity violation in atomic physics and in electron scattering. These ideas preceded the development of the electroweak theory, and were confirmed experimentally by Prescott in electron scattering at SLAC [5] and in cesium atoms by Bouchiat [6]. In the rest of this article we concentrate on parity violation in electron scattering.

Since then, many parity-violating electron scattering experiments have been performed, all summarized in Fig. 1. Prescott’s experiment was followed by an experiment of the Mainz group of Otten and Heil [7] and another one at MIT-Bates on a ^{12}C target [8]. Their experimental techniques were pioneering and are used still today. They were also ground-breaking in establishing parity-violation and making the first measurements of SM parameters from electron scattering (see the green points in Fig. 1 labeled “Pioneering”).

It was first pointed out by Kaplan and Manohar in 1988 [9] that one can get access to a possible contribution of strange quarks to the electromagnetic form factors of the nucleon by measuring its weak electric and magnetic form factors in parity-violating electron scattering. This triggered a whole series of parity-violation electron scattering experiments at the MIT-Bates accelerator [10, 11, 12, 13, 14, 15], at the MAMI accelerator in Mainz [16, 17, 18, 19, 20, 21, 22, 23, 24, 25, 26] as well as at JLab’s CEBAF in Newport News [27, 28, 29, 30, 31, 32, 33, 34, 35, 36, 37, 38, 39, 40] (see in addition [41, 42, 43, 44, 45] for review articles,

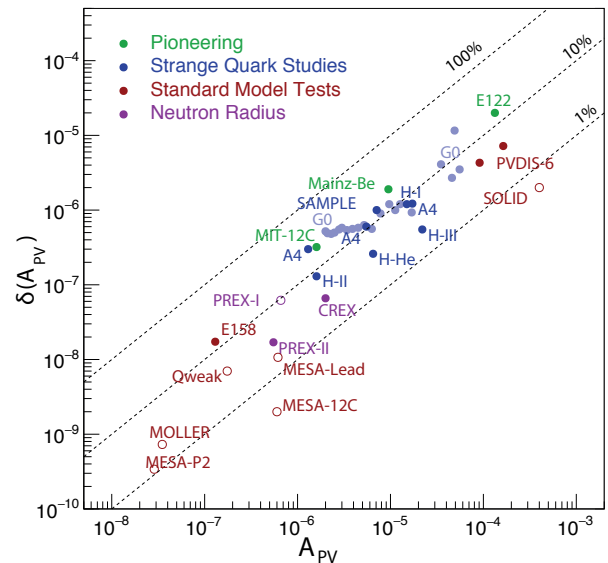


Fig. 1. Overview over past (full points) and future (open circles) electron scattering experiments. From the very early measurements at SLAC, at Bates and in Mainz up to today, parity-violating electron scattering has become a well established technique to explore hadron physics, nuclear physics and particle physics, depending on kinematics and target. The point labelled MESA-P2 is the P2 experiment at the MESA accelerator employing a ℓH_2 -Target. The point labeled MESA-12C denotes the P2 experimental facility with a ^{12}C target.

blue points in Fig. 1 labeled “Strange Quark Studies”). An accurate measurement of the neutron distribution in heavier nuclei and especially the so called “neutron skin” can be obtained from parity-violating electron scattering on heavy nuclei like lead [46, 47]. The associated parity-violation experiments are labeled “Neutron Radius” in Fig. 1. In recent years, experiments have been performed and new proposals have been worked out to measure the weak charge of the proton or of the electron, or the ratio of quark charges. Those are labeled “Standard Model Tests” in Fig. 1 [48, 49, 50, 51, 52]. The parity-violating electron scattering experiments at the new Mainz MESA accelerator [53] are the subject of this manuscript.

In the P2 experiment, parity-violation in elastic electron-proton scattering at low momentum transfer, Q^2 , will provide experimental access to the proton’s weak charge $Q_W(p)$, the analog of the electric charge which determines the strength of the neutral-current weak interaction. In the SM, $Q_W(p)$ is related to the electroweak mixing angle, $\sin^2 \theta_W$. The weak charge of the proton is particularly interesting, compared to that of other nuclei, since it is suppressed in the SM and therefore sensitive to hypothetical new physics effects. The SM also provides a firm prediction for the energy-scale dependence of the running of $\sin^2 \theta_W$. This scale dependence, defined in the $\overline{\text{MS}}$ scheme, is shown in Fig. 2 together with the anticipated sensitivity of the measurement of the weak mixing angle at P2 compared to other forthcoming determinations (blue points) and existing measurements (red points).

^a Corresponding author, maas@uni-mainz.de

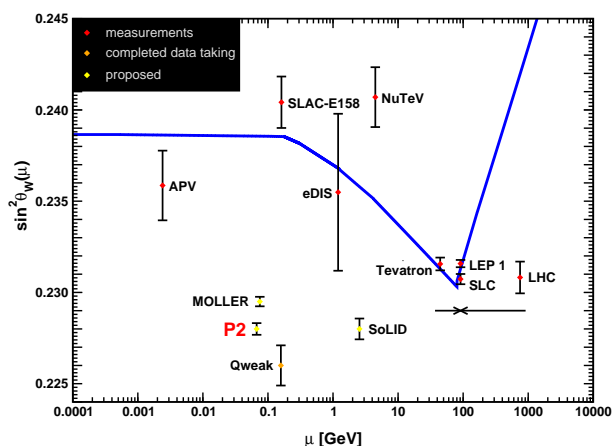


Fig. 2. Scale dependence of the weak mixing angle, $\sin^2 \hat{\theta}_W(\mu)$ compared with existing and forthcoming measurements. The anticipated QWeak point is shown with error bars obtained with the full data set, but moved to an arbitrary position next to the anticipated MOLLER and P2 points [54].

A precise measurement of the weak charge provides, therefore, a precision test of the SM and its predictions. The envisaged measurement of the P2 experiment at low momentum transfer will complement other high-precision determinations, like those of the LEP and SLC experiments at the Z pole. The P2 experiment may thus help to resolve differences between previous measurements, or find interesting new effects.

Extensions of the SM lead to modified predictions for various observables, visible only in high-precision measurements. For example, models with dark photons predict a small shift of the running weak mixing angle at low mass scales, i.e., a change of $\sin^2 \theta_W$ visible at P2, but not at the Z -pole measurements. Other models, like supersymmetry, lead to characteristic deviations for different observables and only a combined analysis can reveal the type of new physics. A convenient way to compare the reach of different observables to the mass scale, Λ , of new physics is based on a description with effective 4-fermion operators. Following the convention that the relevant coupling constant is normalized by $g^2 = 4\pi$, one can estimate the reach by $\Lambda^2 = 8\pi\sqrt{2}/(G_F\Delta Q_W)$ where G_F is the Fermi constant and ΔQ_W the precision for the measurement of the weak charge. At P2, the measurement of the weak charge of the proton is expected to reach mass scales close to 50 TeV [55]. Other targets, like ^{12}C may increase this limit even further.

Our understanding of the electroweak interactions will improve considerably by the forthcoming high-precision experiments. The measurement of the weak charge is expected to improve by a factor of 3 compared to the anticipated precision achieved by the QWeak collaboration at JLab [54]. Similarly, the MOLLER experiment at JLab will provide us with a factor of 5 improvement of the determination of the weak charge of the electron, compared with the result of the E158 experiment at SLAC. Also the ratio of u - and d -quark weak charges will be measured

more precisely than before at the SOLID experiment at JLab. If completed, the combination of these experiments will offer us a handle to distinguish extensions of the SM, which contribute in different ways to these experiments.

The Mainz MESA electron accelerator with the P2 experimental facility for parity-violation experiments opens a door to a rich parity-violation measurement program including different targets and kinematics. This is partly described in the Sect. 7. This research program has its roots in discussions at a workshop at MIT, organised by MIT, JLab, and Mainz in 2013. For more information, see [53].

The second experimental facility at MESA is MAGIX. It will be equipped with two magnetic spectrometers and a hydrogen cluster jet target. MAGIX has a rich program in nucleon and nuclear physics, including measurements of the proton radius, the electromagnetic form factors of the nucleon, measurements of nuclear cross sections relevant for open questions in astrophysics, and dark photon searches in scattering and in a beam dump experiment. Also the MAGIX research program was discussed at the aforementioned MIT workshop.

This manuscript is organized as follows: In Section 2 we describe how – and how accurate – we can extract the weak mixing angle from the measurement of the parity-violating cross section asymmetry. In Section 3 we describe the new MESA accelerator which will be installed in a new accelerator hall from 2020 on. This Section also describes the polarimetry at MESA as well as the control of helicity-correlated and uncorrelated beam fluctuations. For the measurement proposed here, a liquid hydrogen target with the lowest possible level of density fluctuations (10 ppm in 4 ms) from boiling in the volume of the ℓH_2 or from other sources will represent one of the centerpieces. The design approach, the method to calculate the density fluctuations beforehand and the experience from the design of the ℓH_2 target at the former QWeak experiment are described in Sect. 4. The P2 spectrometer, consisting of the ℓH_2 target, the large solenoid magnet, the results of the full Geant4 simulations of the spectrometer, the integrating Cherenkov detectors, the high-resolution ADC system for the read-out as well as the tracking detector is presented in Sect. 5. The new level of experimental accuracy required in the past, and still requires, corresponding theory efforts in order to get effects from QED corrections, box graph and hadronic uncertainties and other electroweak radiative corrections under control. The relevant recent theory work is described in Sect. 6. The P2 experimental facility for parity-violating electron scattering allows for a rich measurement program, like an additional backward-angle measurement to further reduce the uncertainty from the axial form factor and the contribution from strangeness to the magnetic form factor. Both are not sizeable quantities, but still have large error bars. Another example is an additional measurement with a ^{12}C target. This allows for an even more sensitive search for beyond Standard Model physics. A very sensi-

tive measurement of the neutron skin thickness in lead is possible with the P2 spectrometer as well. This exciting further physics program at the P2 experimental facility is described in Sect. 7. The manuscript presented here closes with a summary.

2 Determining the Weak Mixing Angle from Parity Violating Electron Scattering

In this chapter, the experimental method for measuring the proton's weak charge $Q_W(p)$ is presented and the achievable precision in the determination of the electroweak mixing angle $\sin^2 \theta_W$ is discussed.

2.1 Experimental method

For the P2 experiment, MESA will provide a beam of longitudinally polarized electrons. The beam energy will be

$$E_{\text{beam}} = 155 \text{ MeV} \quad (1)$$

and the beam current is scheduled to be

$$I_{\text{beam}} = 150 \text{ } \mu\text{A}. \quad (2)$$

The helicity of the beam electrons will be switched with a frequency $f \sim 1 \text{ kHz}$. The beam electrons impinge on an unpolarized ℓH_2 -target with a length of $L = 600 \text{ mm}$ oriented along the beam direction. The electrons, which are scattered elastically off the protons, are detected in an azimuthally symmetric Cherenkov detector. Figure 3 illustrates the measurement principle. Since the luminosity

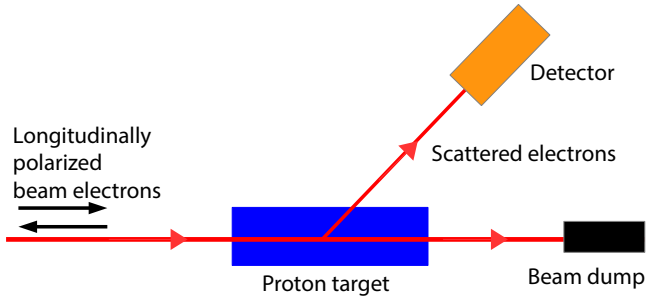


Fig. 3. Experimental method to be used in the P2 experiment: A longitudinally polarized beam of electrons is impinging on a long proton target. For each helicity state of the beam electrons the elastically scattered electrons are detected.

\mathcal{L} of the P2 experiment is projected to be

$$\mathcal{L} = I_{\text{beam}}/e \cdot \rho_{\text{part}} \cdot L = 2.38 \times 10^{39} \text{ cm}^{-2}\text{s}^{-1}, \quad (3)$$

where e is the elementary charge and ρ_{part} is the proton density in ℓH_2 , the total rate of the electrons scattered elastically off protons which needs to be detected is in the order of 0.1 THz. This makes an integrating measurement of the event rates necessary.

2.1.1 Parity-violating asymmetry in elastic electron-proton scattering

The main observable in the P2 experiment is the parity-violating asymmetry A^{PV} in elastic electron-proton scattering. It is an asymmetry in the cross section which may be defined by

$$A^{\text{PV}} \equiv \frac{d\sigma_{\text{ep}}^+ - d\sigma_{\text{ep}}^-}{d\sigma_{\text{ep}}^+ + d\sigma_{\text{ep}}^-}. \quad (4)$$

In this equation, $d\sigma_{\text{ep}}^\pm$ is the differential cross section for the elastic scattering of electrons with helicity $\pm 1/2$ off unpolarized protons.

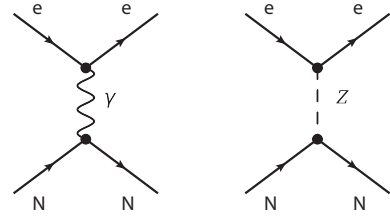


Fig. 4. Feynman diagrams showing the exchange of a virtual photon and Z-boson in the process of electron-nucleon scattering.

A^{PV} is due to the interference between the exchange of a virtual photon and a Z-boson in the scattering process, both of which are illustrated in Fig. 4. The differential cross section of the scattering process can be written

$$\left(\frac{d\sigma_{\text{ep}}^\pm}{d\Omega}\right) = \left(\frac{\alpha_{\text{em}}}{4m_p Q^2} \frac{E_f}{E_i}\right)^2 |\mathcal{M}_{\text{ep}}^\pm|^2, \quad (5)$$

where α_{em} is the electromagnetic coupling, m_p is the proton mass, and

$$Q^2 \approx 4E_i E_f \sin^2(\theta_f/2) \quad (6)$$

is the negative square of the 4-momentum transfer between electron and proton. Here, the electron mass can be neglected. E_i is the electron's initial state energy, E_f the energy of the scattered electron and θ_f the scattering angle with respect to the beam direction. $\mathcal{M}_{\text{ep}}^\pm$ is the transition matrix element, at leading order given by the Feynman diagrams shown in Fig. 4.

The resulting parity-violating helicity asymmetry is written as

$$A^{\text{PV}} = \frac{-G_F Q^2}{4\pi\alpha_{\text{em}}\sqrt{2}} [Q_W(p) - F(E_i, Q^2)], \quad (7)$$

where G_F is the Fermi coupling constant. Here, the weak charge of the proton, $Q_W(p)$, is defined as the limit of the asymmetry at zero-momentum transfer, normalized such that Eq. (7) holds, i.e., $F(E_i, Q^2 = 0) = 0$. At non-zero momentum transfer, the hadronic structure of the proton has to be taken into account, parametrized by the Q^2 - and energy-dependent function $F(E_i, Q^2)$. The function F is

often written as $F(E_i, Q^2) = Q^2 B(Q^2)$ and the energy-dependence not shown explicitly.

Based on a flavour decomposition of the matrix elements of the electromagnetic and weak neutral currents, the form factor contribution $F(Q^2)$ is usually written as a sum of three terms

$$F(E_i, Q^2) \equiv F^{\text{EM}}(E_i, Q^2) + F^{\text{A}}(E_i, Q^2) + F^{\text{S}}(E_i, Q^2), \quad (8)$$

where

$$F^{\text{EM}}(E_i, Q^2) \equiv \frac{\epsilon G_{\text{E}}^{\text{p},\gamma} G_{\text{E}}^{\text{n},\gamma} + \tau G_{\text{M}}^{\text{p},\gamma} G_{\text{M}}^{\text{n},\gamma}}{\epsilon (G_{\text{E}}^{\text{p},\gamma})^2 + \tau (G_{\text{M}}^{\text{p},\gamma})^2} \quad (9)$$

is given by the proton's electric and magnetic form factors $G_{\text{E}}^{\text{p},\gamma}$ and $G_{\text{M}}^{\text{p},\gamma}$ as well as the neutron's electric and magnetic form factors $G_{\text{E}}^{\text{n},\gamma}$ and $G_{\text{M}}^{\text{n},\gamma}$. $F^{\text{A}}(E_i, Q^2)$ depends on the proton's axial form factor $G_{\text{A}}^{\text{p},Z}$ and is denoted as

$$F^{\text{A}}(Q^2) \equiv \frac{(1 - 4 \sin^2 \theta_{\text{W}}) \sqrt{1 - \epsilon^2} \sqrt{\tau(1 - \tau)} G_{\text{M}}^{\text{p},\gamma} G_{\text{A}}^{\text{p},Z}}{\epsilon (G_{\text{E}}^{\text{p},\gamma})^2 + \tau (G_{\text{M}}^{\text{p},\gamma})^2}. \quad (10)$$

$F^{\text{S}}(Q^2)$ depends on the nucleon's strange electric and magnetic form factors G_{E}^{s} and G_{M}^{s} as well as the isospin-breaking form factors $G_{\text{E}}^{\text{u,d}}$ and $G_{\text{M}}^{\text{u,d}}$:

$$F^{\text{S}}(E_i, Q^2) \equiv \frac{\epsilon G_{\text{E}}^{\text{p},\gamma} G_{\text{E}}^{\text{s}} + \tau G_{\text{M}}^{\text{p},\gamma} G_{\text{M}}^{\text{s}}}{\epsilon (G_{\text{E}}^{\text{p},\gamma})^2 + \tau (G_{\text{M}}^{\text{p},\gamma})^2} + \frac{\epsilon G_{\text{E}}^{\text{p},\gamma} G_{\text{E}}^{\text{u,d}} + \tau G_{\text{M}}^{\text{p},\gamma} G_{\text{M}}^{\text{u,d}}}{\epsilon (G_{\text{E}}^{\text{p},\gamma})^2 + \tau (G_{\text{M}}^{\text{p},\gamma})^2}. \quad (11)$$

In these expressions we have used the abbreviations

$$\epsilon \equiv \left[1 + 2(1 + \tau) \tan^2 \left(\frac{\theta_{\text{f}}}{2} \right) \right]^{-1} \quad (12)$$

and

$$\tau \equiv \frac{Q^2}{4m_{\text{p}}^2}. \quad (13)$$

According to Eq. (7), A^{PV} is proportional to Q^2 . In Fig. 5 we show the dependence of A^{PV} on θ_{f} for $E_i = 155$ MeV, which equals the beam energy to be used in the P2 experiment. The picture also shows the separate contributions

$$\begin{aligned} A^{\text{Qw}} &\equiv \frac{-G_{\text{F}} Q^2}{4\pi\alpha_{\text{em}}\sqrt{2}} \cdot Q_{\text{W}}(\text{p}), \\ A^{\text{EM}} &\equiv \frac{G_{\text{F}} Q^2}{4\pi\alpha_{\text{em}}\sqrt{2}} \cdot F^{\text{EM}}, \\ A^{\text{A}} &\equiv \frac{G_{\text{F}} Q^2}{4\pi\alpha_{\text{em}}\sqrt{2}} \cdot F^{\text{A}}, \\ A^{\text{S}} &\equiv \frac{G_{\text{F}} Q^2}{4\pi\alpha_{\text{em}}\sqrt{2}} \cdot F^{\text{S}} \end{aligned} \quad (14)$$

to A^{PV} . One can see that at low Q^2 , A^{PV} is dominated by A^{Qw} , while the hadronic contributions are small. A measurement of A^{PV} at low Q^2 is therefore sensitive to the weak charge of the proton, $Q_{\text{W}}(\text{p})$.

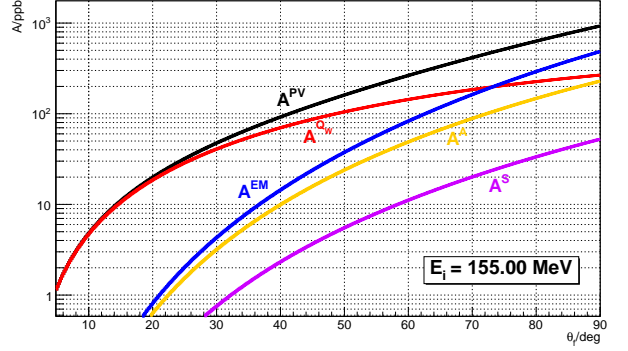


Fig. 5. Dependence of A^{PV} on θ_{f} for $E_i = 155$ MeV. Plotted are the absolute values of the asymmetry and the contributions by the proton's weak charge and the nucleon form factors to A^{PV} . For low values of Q^2 , A^{PV} is dominated by the weak charge contribution A^{Qw} . At the central scattering angle of the P2 experiment, $A^{\text{PV}}(\theta_{\text{f}} = 35^\circ) = -67.34$ ppb.

2.1.2 The proton's weak charge and the electroweak mixing angle

Neglecting radiative corrections, the tree-level expression for the proton's weak charge in (7) is

$$Q_{\text{W}}(\text{p}) = 1 - 4 \sin^2 \theta_{\text{W}}, \quad (15)$$

where θ_{W} is the electroweak mixing angle or Weinberg-angle. In the following we will often use the abbreviation $s_{\text{W}} = \sin \theta_{\text{W}}$. Since $\sin^2 \theta_{\text{W}} \approx 0.23$, $Q_{\text{W}}(\text{p})$ is small in the SM. From (15), using Gaussian error propagation, it follows that

$$\frac{\Delta \sin^2 \theta_{\text{W}}}{\sin^2 \theta_{\text{W}}} = \frac{1 - 4 \sin^2 \theta_{\text{W}}}{4 \sin^2 \theta_{\text{W}}} \cdot \frac{\Delta Q_{\text{W}}(\text{p})}{Q_{\text{W}}(\text{p})} \approx 0.09 \cdot \frac{\Delta Q_{\text{W}}(\text{p})}{Q_{\text{W}}(\text{p})}. \quad (16)$$

Therefore, a precise measurement of $Q_{\text{W}}(\text{p})$ will result in an approximately 10 times more precise determination of the electroweak mixing angle. The weak charge of the proton is therefore highly sensitive to the electroweak mixing angle.

Even small corrections to $\sin^2 \theta_{\text{W}}$ may modify $Q_{\text{W}}(\text{p})$ significantly. A wide range of beyond-SM effects can lead to such corrections. They need to be disentangled from SM radiative corrections. Higher-order corrections to A^{PV} will be discussed later in Sect. 6.

2.2 Achievable precision in the determination of the weak mixing angle

In order to predict the achievable precision in the determination of $\sin^2 \theta_{\text{W}}$, error propagation calculations based on the Monte Carlo method have been carried out. The goal of these calculations was to determine the achievable uncertainty Δs_{W}^2 as a function of the beam energy E_{beam} , the central electron scattering angle θ_{f} and the acceptance of the azimuthally symmetric detector in θ_{f} ,

denoted $\delta\theta_f \equiv [\bar{\theta}_f - \delta\theta_f/2, \bar{\theta}_f + \delta\theta_f/2]$. In the following, the method used to calculate Δs_{W}^2 will be discussed and results of the calculations will be presented. Based on these results, the beam energy and detector acceptance to be used in the P2 experiment are chosen.

2.2.1 Method to determine the achievable uncertainty of $\sin^2 \theta_{\text{W}}$

The analysis presented in this section is based on the leading-order prediction of A^{PV} . Therefore we use the generic symbol s_{W} for the sine of the weak mixing angle. Only if higher-order corrections are included, one will have to distinguish between the on-shell or the $\overline{\text{MS}}$ definitions of s_{W} and, in the latter case, specify its scale-dependence.

In a parity-violation electron scattering experiment, one measures the asymmetry

$$A^{\text{exp}} \equiv \frac{N^+ - N^-}{N^+ + N^-}, \quad (17)$$

which is determined by the total numbers N^\pm of detected scattering events for the two helicity states of the beam electrons. One can write

$$A^{\text{exp}} = P \cdot \langle A^{\text{PV}} \rangle_{L, \delta\theta_f} + A^{\text{app}}, \quad (18)$$

where P is the average polarization of the electron beam,

$$\langle A^{\text{PV}} \rangle_{L, \delta\theta_f} = \frac{\int_0^L dz \int_{\theta_f^{\text{min}}}^{\theta_f^{\text{max}}} d\cos\theta_f \left(\frac{d\sigma_{\text{ep}}^0}{d\Omega} \right) \cdot A^{\text{PV}}}{\int_0^L dz \int_{\theta_f^{\text{min}}}^{\theta_f^{\text{max}}} d\cos\theta_f \left(\frac{d\sigma_{\text{ep}}^0}{d\Omega} \right)} \quad (19)$$

is the expected value of A^{PV} after averaging over the target length L and the detector acceptance in θ_f . In addition, the polarization independent part of the differential cross section

$$\frac{d\sigma_{\text{ep}}^0}{d\Omega} = \frac{d\sigma^{\text{Mott}}}{d\Omega} \cdot \left[\frac{(G_{\text{E}}^{n,\gamma})^2 + \tau(G_{\text{M}}^{n,\gamma})^2}{1 + \tau} + 2\tau(G_{\text{M}}^{n,\gamma} \tan(\theta_f/2))^2 \right] \quad (20)$$

given by the Rosenbluth formula [56] is taken into account. Furthermore, A^{app} is an apparatusive asymmetry induced by helicity-correlated fluctuations of the electron beam's properties. In Eq. (19), the averaging over the target's length is done to include the mean energy loss of the beam electrons due to collision and radiation processes as they travel through the target volume. At leading-order, both $d\sigma_{\text{ep}}^0$ and A^{PV} may be regarded as functions of the electron's mean initial state energy $\langle E_i \rangle(z)$ and scattering angle θ_f . $\langle E_i \rangle(z)$ depends on the z -coordinate of the interaction vertex's position in the target and decreases with increasing penetration depth of the beam electrons.

To predict Δs_{W}^2 , Eq. (18) is solved for s_{W}^2 , and an error propagation calculation based on the resulting expression is performed. This expression has the general structure

$$s_{\text{W}}^2 = s_{\text{W}}^2(A^{\text{exp}}, P, E_{\text{beam}}, \bar{\theta}_f, \delta\theta_f, F(\{\kappa_k\}, Q^2), \square_{\gamma Z}), \quad (21)$$

where $F(\{\kappa_k\}, Q^2)$ represents parametrizations of the nucleon's form factors which depend on a set of independent, real parameters $\{\kappa_k\}$, and $\square_{\gamma Z}$ are the contributions from γZ -box graphs. Therefore, one may consider s_{W}^2 a function of a set of independent parameters $\{\lambda_i\}$:

$$s_{\text{W}}^2 = s_{\text{W}}^2(\{\lambda_i\}), \quad (22)$$

with

$$\lambda_i \in \{A^{\text{exp}}, P, E_{\text{beam}}, \bar{\theta}_f, \delta\theta_f, \{\kappa_k\}, \square_{\gamma Z}\}. \quad (23)$$

The Gaussian error propagation based on Eq. (22) is not straightforward, since the integrations in Eq. (19) cannot be done analytically.

Therefore, Monte Carlo based error propagation calculations have been carried out numerically. The idea is to treat the parameters λ_i as independent random variables and to calculate a distribution of s_{W}^2 values by inserting the randomized parameters into Eq. (22). The first step to achieve this is to assign a Gaussian probability distribution to each parameter λ_i by defining the distribution's mean value $\langle \lambda_i \rangle$ and standard deviation $\Delta \lambda_i$. One then samples a set of random values $\{\lambda'_i\}$ according to the assigned probability distributions using a random number generator. Substituting the randomized values into Eq. (22) leads to

$$(s_{\text{W}}^2)' = s_{\text{W}}^2(\{\lambda'_i\}). \quad (24)$$

Iterating this procedure leads to a distribution of $(s_{\text{W}}^2)'$ values, from which the expected value $\langle s_{\text{W}}^2 \rangle$ and standard deviation Δs_{W}^2 can be extracted. While the mean value is expected to match the input value of s_{W}^2 used to calculate A^{PV} , Δs_{W}^2 is in the following regarded as the achievable precision in the determination of the electroweak mixing angle.

The algorithm allows to calculate the contributions of individual parameters λ_i to Δs_{W}^2 by sampling only the parameter whose contribution is of interest while all other parameters are kept constant at their expected values. Furthermore, it is possible to compute the expected value $\langle \Delta s_{\text{W}}^2 \rangle$ and the uncertainty $\Delta(\Delta s_{\text{W}}^2)$ of Δs_{W}^2 by sampling a distribution of Δs_{W}^2 -values. This distribution is generated by repeatedly calculating values of Δs_{W}^2 for the same choice of $\{\langle \lambda_i \rangle\}$ and $\{\Delta \lambda_i\}$. From the resulting distribution of Δs_{W}^2 values, both the mean value $\langle \Delta s_{\text{W}}^2 \rangle$ and the standard deviation $\Delta(\Delta s_{\text{W}}^2)$ are extracted.

2.2.2 Input parameters to the calculation of Δs_{W}^2

The mean values and standard deviations of the parameters λ_i are chosen according to the projected experimental conditions of the experiment. Table 1 lists all parameter values related to the experimental conditions at the

| λ_l | $\langle \lambda_l \rangle$ | $\Delta \lambda_l$ |
|-------------------|-----------------------------|---------------------|
| E_{beam} | variable | 0.13 MeV |
| $\bar{\theta}_f$ | variable | 0° |
| $\delta\theta_f$ | variable | 0.1° |
| $\delta\phi_f$ | 360° | 0° |
| I_{beam} | 150 μA | 0.001 μA |
| P | 0.85 | 0.00425 |
| L | 600 mm | 0 mm |
| T | 1×10^4 h | 0 h |
| A^{app} | 0 | 0.1 ppb |

Table 1. Mean values and standard deviations chosen for performing the error propagation calculations. $\delta\phi_f$ denotes the azimuthal acceptance of the detector and T is the measuring time. Parameters for which $\Delta\lambda_l = 0$ is shown have been kept constant during the calculations.

MESA facility. A systematic scan of the mean values of $(E_{\text{beam}}, \theta_f, \delta\theta_f)$ has been performed in order to determine appropriate values for these parameters for the design of the experimental apparatus.

The expected value of the asymmetry $\langle A^{\text{exp}} \rangle$ is calculated by inserting the mean values of the relevant parameters into Eq. (18). As standard deviation ΔA^{exp} the statistical uncertainty of A^{exp} is chosen. Assuming Poisson-statistics and starting from Eq. (18), one finds that

$$\Delta A^{\text{exp}} \equiv \sqrt{\frac{1}{N}}, \quad (25)$$

where it has been assumed that

$$N \equiv N^+ + N^- \approx 2N^+ \approx 2N^-. \quad (26)$$

In addition to the uncertainty contributions to Δs_{W}^2 originating from the experiment-related parameters listed in Tab. 1, one expects a significant contribution from the γZ -box graph. At $E_i = 155$ MeV, one expects

$$\square_{\gamma Z} = 1.07 \times 10^{-3}, \quad (27)$$

$$\Delta \square_{\gamma Z} = 0.18 \times 10^{-3} \quad (28)$$

for the central value and the 1σ uncertainty of $\square_{\gamma Z}$ [57]. Details of the box-graph corrections and the definition of $\square_{\gamma Z}$ are discussed in Sect. 6.1.

It has been assumed in Eq. (21) that the nucleon form factors can be parametrized as functions $F(\{\kappa_k\}, Q^2)$, where $\{\kappa_k\} \subset \{\lambda_l\}$ is a set of independent, real parameters. In the following, we present the parametrizations of the nucleon form factors that have been used to carry out the error propagation calculations.

Electromagnetic form factors of the proton. The form factors $G_{\text{E}}^{\text{p},\gamma}$ and $G_{\text{M}}^{\text{p},\gamma}$ have been parametrized using the ‘‘Dipole \times Polynomial-Model’’, which has been developed

by Bernauer et al. [58]. In this model, the standard dipole term

$$G_{\text{dipole}}^{\text{std}}(Q^2) = \left(1 + \frac{Q^2}{0.71 \text{ GeV}^2}\right)^{-2} \quad (29)$$

is multiplied by a polynomial

$$G_{\text{E},\text{M}}^{\text{poly}}(Q^2) = 1 + \sum_{i=1}^8 \left(\kappa_i^{\text{E},\text{M}} \cdot Q^{2i}\right) \quad (30)$$

such that

$$G_{\text{E}}^{\text{p},\gamma}(Q^2) = G_{\text{dipole}}^{\text{std}}(Q^2) \cdot G_{\text{E}}^{\text{poly}}(Q^2),$$

$$G_{\text{M}}^{\text{p},\gamma}(Q^2) = \mu_{\text{P}}/\mu_{\text{N}} \cdot G_{\text{dipole}}^{\text{std}}(Q^2) \cdot G_{\text{M}}^{\text{poly}}(Q^2), \quad (31)$$

where $\mu_{\text{P}} = 2.792847356 \cdot \mu_{\text{N}}$ is the proton’s magnetic moment and $\mu_{\text{N}} = (e\hbar)/(2m_{\text{p}})$ is the nuclear magneton. In order to retrieve the parameters κ_l of the parametrization, Eq. (31) has been fitted to the data sets given in section K 2.2.3 of [58], leading to the parameter values listed in the Appendix, Tabs. 17 and 18.

Electromagnetic form factors of the neutron. The functions used to parametrize $G_{\text{E}}^{\text{n},\gamma}$ and $G_{\text{M}}^{\text{n},\gamma}$ have been chosen as in Ref. [59]. For $G_{\text{E}}^{\text{n},\gamma}$, a fit function according to Galster [60] has been used:

$$G_{\text{E}}^{\text{n},\gamma}(Q^2) = \frac{\kappa_1\tau}{1 + \kappa_2\tau} \cdot G_{\text{dipole}}^{\text{std}}(Q^2), \quad (32)$$

where $G_{\text{dipole}}^{\text{std}}(Q^2)$ is defined in Eq. (31) and τ in Eq. (13). The fit of Eq. (32) to the data set given in [59] leads to the parameter values listed in Tab. 19. In order to parametrize the neutron’s magnetic form factor $G_{\text{M}}^{\text{n},\gamma}$ a polynomial of degree 9 is used:

$$G_{\text{M}}^{\text{n},\gamma}(Q^2) = \sum_{i=0}^9 \kappa_i Q^{2i}. \quad (33)$$

Fitting Eq. (33) to the data given in [59] results in the parameters listed in Tab. 20.

Strangeness form factors. The experimental determination of the strangeness form factors G_{E}^{s} and G_{M}^{s} has been the subject of a comprehensive measurement program for 15 years in three major research facilities. Measurements with $Q^2 = 0.1 \text{ GeV}^2$, $Q^2 = 0.23 \text{ GeV}^2$ and $Q^2 = 0.63 \text{ GeV}^2$ have been carried out by the SAMPLE, HAPPEX, G0 and the A4 Collaborations [14, 35, 33, 37, 16, 24].

Like $G_{\text{E}}^{\text{n},\gamma}$, G_{E}^{s} has been parametrized using Eq. (32). Fitting this expression to the available world data leads to the parameter values presented in Tab. 21. For G_{M}^{s} , the parametrization

$$G_{\text{M}}^{\text{s}} = \kappa_0 + \kappa_1 \cdot Q^2, \quad (34)$$

which was taken from Ref. [61], has been used along with the parameter values given in Tab. 22.

In the following it is assumed that the uncertainties of G_E^s and G_M^s can be reduced by factors of 4 and 12, respectively, in the Q^2 region of relevance to the P2 experiment. This reduction can be achieved by an additional backward-angle measurement, see Sect. 7.3.

Axial form factor of the proton. The axial form factor of the proton $G_A^{p,Z}$ can be determined from results of parity-violation electron scattering experiments with ℓH_2 - and ℓD_2 -targets, which have been carried out at backward scattering angles at the same values of Q^2 . Appropriate measurements have been done by the SAMPLE, G0 and A4 Collaborations [15, 35, 37, 25].

For the purpose of the error propagation calculations presented in this section, $G_A^{p,Z}$ has been parametrized as suggested by Musolf et al. in Ref. [41]:

$$G_A^{p,Z}(Q^2) = \kappa_0 \cdot \left(1 + \frac{Q^2}{\kappa_1^2}\right)^{-2} \quad (35)$$

This parametrization is used together with the parameter values given in [41] and listed in Tab. 23.

For the error propagation calculations presented in this section it has been assumed that the global uncertainty of the parametrization given by Eq. (35) can be reduced by a factor of 10. This reduction can be achieved by a backward-angle measurement of $G_A^{p,Z}$ (see Sect. 7.3).

The requirement of reducing the uncertainties of G_E^s , G_M^s and $G_A^{p,Z}$ in order to achieve the envisaged precision in the determination of $\sin^2 \theta_W$ renders the form factor measurement within the scope of the P2 experiment mandatory.

Isospin breaking electromagnetic form factors. The parametrizations of the isospin-breaking form factors G_E^{ud} and G_M^{ud} have been done using the dataset quoted in the bachelor thesis of P. Larin [62]. Larin has extracted data from the predictions for the Q^2 -dependence of the form factors given in [63]. In order to parametrize G_E^{ud} and G_M^{ud} , polynomials of degree 4 have been used such that

$$G_{E,M}^{\text{ud}} = \sum_{i=0}^4 \kappa_i^{\text{E,M}} \cdot Q^{2i}. \quad (36)$$

The fits of these functions to the data given in Ref. [62] result in the parameter values collected in Tabs. 24 and 25.

2.2.3 Results of the error propagation calculations

An extensive scan in the mean values of E_{beam} , $\bar{\theta}_f$ and $\delta\theta_f$ has been performed using the input parameters discussed in the preceding section in order to determine suitable values of these variables to carry out the P2 experiment. In this section, selected results are presented and discussed.

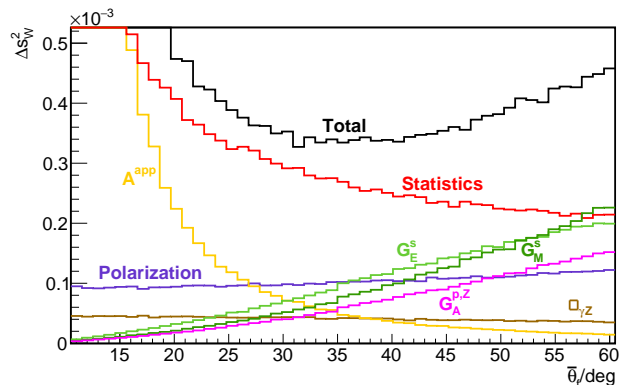


Fig. 6. Dependence of Δs_W^2 on the central scattering angle $\bar{\theta}_f$ for $E_{\text{beam}} = 155$ MeV and $\delta\theta_f = 20^\circ$. The total uncertainty Δs_W^2 of the electroweak mixing angle is shown in black and other dominating error contributions in color.

Figure 6 shows the dependence of Δs_W^2 on the central electron scattering angle $\bar{\theta}_f$ for $E_{\text{beam}} = 155$ MeV and $\delta\theta_f = 20^\circ$. For $17^\circ \leq \bar{\theta}_f \leq 55^\circ$, the total uncertainty is dominated by the statistical uncertainty of the measured asymmetry A^{exp} . For scattering angles $\bar{\theta}_f \geq 40^\circ$ the contributions from $G_{E,M}^s$ and $G_A^{p,Z}$ become more significant, because the form factors' contribution to the asymmetry increases with Q^2 . The increase of the form factor contributions and the decrease of the statistical error and the contribution stemming from A^{app} with increasing $\bar{\theta}_f$ lead to a minimum of Δs_W^2 at $\bar{\theta}_f \approx 35^\circ$, where $\Delta s_W^2 \approx 3.4 \times 10^{-4}$.

Figure 7 shows the dependence of Δs_W^2 on $\bar{\theta}_f$ for $E_{\text{beam}} = 155$ MeV and different choices of $\delta\theta_f$. In general, a larger value of $\delta\theta_f$ leads to a larger N and therefore to a smaller statistical uncertainty of A^{exp} . Since the statistical uncertainty of A^{exp} is the dominant contribution to Δs_W^2 , the achievable uncertainty in the electroweak mixing angle decreases with rising $\delta\theta_f$. The larger the acceptance, the smaller is the effect of increasing $\delta\theta_f$ on Δs_W^2 , because contributions by the nucleon form factors become more significant at larger scattering angles. To keep the nucleon form factors' contributions reasonably small, we have decided to use $\delta\theta_f \leq 20^\circ$.

Figure 8 shows the dependence of Δs_W^2 on E_{beam} and $\bar{\theta}_f$ for $\delta\theta_f = 20^\circ$. Values of $\Delta s_W^2 \leq 3.4 \times 10^{-4}$ can be achieved in the region marked by a black curve.

To carry out the P2 experiment within the envisaged measurement time of $T = 10 \times 10^4$ h, we have decided to use a beam energy of $E_{\text{beam}} = 155$ MeV, a central scattering angle of $\bar{\theta}_f = 35^\circ$ and a detector acceptance $\delta\theta_f = 20^\circ$. Table 2 lists the results of an error propagation calculation for this choice of kinematic parameters along with the error contributions stemming from the statistical uncertainty of A^{exp} , the contribution of the beam polarization as well as the contribution from helicity correlated beam fluctuations. In order to extract the electroweak mixing angle from the measured uncertainty, one has to take the

nucleon form factors and radiative corrections to the proton's weak charge into account. The expected contributions to Δs_W^2 due to uncertainties of the form factors and of $\square_{\gamma Z}$ are also listed in Tab. 2.

The expected value of the parity-violating asymmetry is

$$\langle A^{\text{exp}} \rangle = -39.94 \text{ ppb} \quad (37)$$

with an uncertainty of

$$\Delta A^{\text{exp}} = 0.56 \text{ ppb} \quad (38)$$

in 1×10^4 h of measurement time. This corresponds to a relative uncertainty of

$$\frac{\Delta A^{\text{exp}}}{\langle A^{\text{exp}} \rangle} = 1.40 \%. \quad (39)$$

The expected uncertainty for the weak mixing angle is

$$\Delta s_W^2 = 3.3 \times 10^{-4} \quad (40)$$

corresponding to a relative uncertainty of

$$\frac{\Delta s_W^2}{\langle s_W^2 \rangle} = 0.14 \% \quad (41)$$

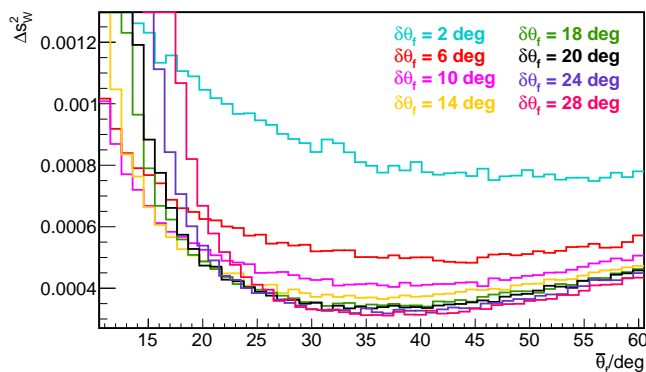


Fig. 7. Dependence of Δs_W^2 on $\bar{\theta}_f$ for $E_{\text{beam}} = 155$ MeV and several values of $\delta\theta_f$. The black curve represents an acceptance of $\delta\theta_f = 20^\circ$, which will be used in the P2 experiment.

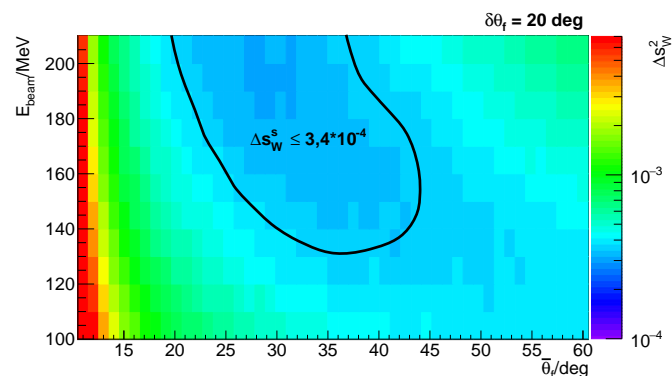


Fig. 8. Dependence of Δs_W^2 on $\bar{\theta}_f$ and E_{beam} for $\delta\theta_f = 20^\circ$. In the region marked by the black curve, values of $\Delta s_W^2 \leq 3.4 \times 10^{-4}$ are achievable.

| | |
|---|--|
| E_{beam} | 155 MeV |
| $\bar{\theta}_f$ | 35° |
| $\delta\theta_f$ | 20° |
| $\langle Q^2 \rangle_{L=600 \text{ mm}, \delta\theta_f=20^\circ}$ | $6 \times 10^{-3} (\text{GeV}/c)^2$ |
| $\langle A^{\text{exp}} \rangle$ | -39.94 ppb |
| $(\Delta A^{\text{exp}})_{\text{Total}}$ | 0.56 ppb (1.40 %) |
| $(\Delta A^{\text{exp}})_{\text{Statistics}}$ | 0.51 ppb (1.28 %) |
| $(\Delta A^{\text{exp}})_{\text{Polarization}}$ | 0.21 ppb (0.53 %) |
| $(\Delta A^{\text{exp}})_{\text{Apparative}}$ | 0.10 ppb (0.25 %) |
| $\langle s_W^2 \rangle$ | 0.231 16 |
| $(\Delta s_W^2)_{\text{Total}}$ | 3.3×10^{-4} (0.14 %) |
| $(\Delta s_W^2)_{\text{Statistics}}$ | 2.7×10^{-4} (0.12 %) |
| $(\Delta s_W^2)_{\text{Polarization}}$ | 1.0×10^{-4} (0.04 %) |
| $(\Delta s_W^2)_{\text{Apparative}}$ | 0.5×10^{-4} (0.02 %) |
| $(\Delta s_W^2)_{\square_{\gamma Z}}$ | 0.4×10^{-4} (0.02 %) |
| $(\Delta s_W^2)_{\text{nucl. FF}}$ | 1.2×10^{-4} (0.05 %) |
| $\langle Q^2 \rangle_{\text{Cherenkov}}$ | $4.57 \times 10^{-3} (\text{GeV}/c)^2$ |
| $\langle A^{\text{exp}} \rangle_{\text{Cherenkov}}$ | -28.77 ppb |

Table 2. Results of the error propagation calculation performed for the design parameters of the P2 experiment. $\langle Q^2 \rangle_{L=600 \text{ mm}, \delta\theta_f=20^\circ}$ is the expected value of Q^2 after averaging over the target's length L and the acceptance in the electron scattering angle θ_f and has been calculated in analogy to Eq. (19). The values given in round brackets are the relative errors with regard to the expected value. $\langle Q^2 \rangle_{\text{Cherenkov}}$ and $\langle A^{\text{exp}} \rangle_{\text{Cherenkov}}$ are the expected values obtained if electrons scattered with $\theta_f < \bar{\theta}_f - \delta\theta_f/2$ and hitting the Cherenkov detector are taken into account (see Sect. 5.1 for details).

for s_W^2 and

$$\frac{\Delta Q_W(p)}{Q_W(p)} = 1.83 \% \quad (42)$$

for the proton's weak charge.

2.2.4 Scattering off the target entry and exit windows

Beam electrons which scatter off the windows of the target cell are an additional source of uncertainty. This effect is briefly discussed here and will be included in the error propagation calculation (see Sect. 2.2.3).

Omitting all other sources of background and beam polarization, the measured asymmetry consists of two contributions:

$$A^{\text{exp}} = (1 - f) \cdot \langle A^{\text{PV}} \rangle + f \cdot \langle A^{\text{Alu}} \rangle \quad (43)$$

where A^{Alu} is the parity-violating asymmetry in eAl scattering and f is the dilution factor

$$f = \frac{Y_{\text{eAl}}}{Y_{\text{ep}} + Y_{\text{eAl}}} \quad (44)$$

Y_{eAl} and Y_{ep} is the yield of scattering events off aluminum and of elastic scattering off the proton, respectively. This equation can be solved for A^{PV} . Gaussian error propagation yields

$$\Delta\langle A^{\text{PV}} \rangle = \sqrt{\left(\frac{\Delta A^{\text{exp}}}{1-R}\right)^2 + \left(\frac{f\Delta\langle A^{\text{Alu}} \rangle}{1-f}\right)^2 + \left(\frac{A^{\text{exp}} - \langle A^{\text{Alu}} \rangle}{(1-f)^2}\Delta f\right)^2}. \quad (45)$$

Both the asymmetry of the aluminum scattering $\langle A^{\text{Alu}} \rangle$ and the dilution factor f need to be measured in the P2 experiment. For an estimation of the size of the effect we use measurements performed by the A4 experiment [16] and the QWeak experiment [64]. From the A4 measurements with an aluminum target which were performed at the same central scattering angle that is foreseen for P2, $\theta_f = 35^\circ$, but with higher electron energies from 570 MeV up to 854 MeV, we find a dilution factor of $f = 0.010$ for a P2 target with a 60 cm liquid hydrogen volume along the beam axis and a total thickness of $d_0 = 250 \mu\text{m}$ for the aluminum entry and exit windows. Other window thicknesses d_{Alu} can be calculated by simply applying the factor d_{Alu}/d_0 to this dilution factor. We plan to determine this dilution factor by measuring the detector yield with an empty target cell with an uncertainty of $\Delta f/f \leq 0.05$. The QWeak measurements with an aluminum target show that the asymmetry $\langle A^{\text{Alu}} \rangle$ is about one order of magnitude larger than the asymmetry $\langle A^{\text{PV}} \rangle$. We use this result to estimate $\langle A^{\text{Alu}} \rangle = 400$ ppb in our case. We plan to perform a 500 hour measurement with a 3 mm thick aluminum target. Based on our rate estimation, the expected uncertainty of this measurement is $\Delta\langle A^{\text{Alu}} \rangle = 6$ ppb. Based on these numbers we can perform the error calculation. Figure 9 shows the contribution from the target window scattering to the uncertainty of $\langle A^{\text{PV}} \rangle$ as a function of the total thickness of the target windows. For example, with a total thickness of $d_0 = 250 \mu\text{m}$ we obtain an error contribution of 0.20 ppb. It is of similar size as the error from the electron beam polarization and well below the anticipated statistical uncertainty.

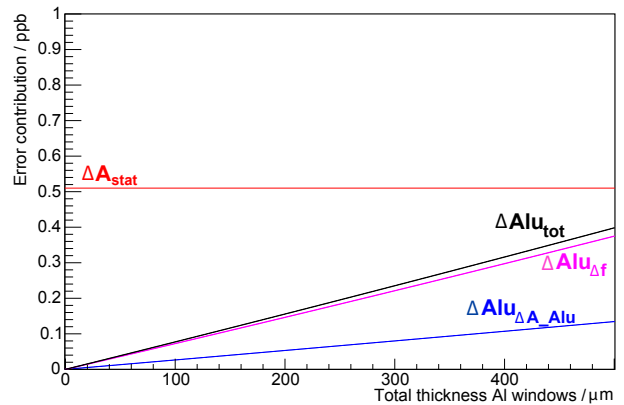


Fig. 9. Error contribution from scattering events of the aluminum windows of the target cell as a function of the total thickness of the entry and exit window. Shown is in blue the contribution arising from the uncertainty of the asymmetry in the eAl scattering $\Delta\langle A^{\text{Alu}} \rangle$ (in ppb) and in purple the contribution arising from the uncertainty in the dilution factor f . Here we assume $\Delta\langle A^{\text{Alu}} \rangle = 6$ ppb and $\Delta f/f = 0.05$. The black line shows the quadratic sum of both terms. For comparison, the expected statistical uncertainty of the P2 measurement $\Delta A^{\text{exp}} = 0.51$ ppb is shown in red.

3 The MESA Accelerator

The increased demand for experiments at the MESA accelerator has necessitated a new experimental hall which is currently being erected. The civil construction work will be finalized in 2020. Figure 10 shows the MESA accelerator layout with several components that are especially relevant for the P2 experiment. In P2, the beam will be extracted from the accelerator, directed towards the experiment and will be stopped afterwards in the heavily shielded beam dump building. The beam energy gain per pass is given by the acceleration capacity of the two cryomodules which are designed for 25 MeV each. After three passages through the cryomodules the beam energy at P2 reaches 155 MeV, (50 MeV per pass + 5 MeV from injector), lower energies are possible.

An 85% spin-polarized beam of 150 μA intensity is generated in a polarized source (described in Sect. 3.1) and then injected into the MESA Low-energy Beam Apparatus, MELBA. One of the main purposes of MELBA is spin manipulation. Due to $g - 2$ precession, the spin angle at P2 would not appear exactly longitudinal if no compensation by an additional spin rotation is provided. The additional spin angle can be achieved by a Wien-filter spin rotator of the type that is presently installed in MAMI [65]. A second Wien filter will be installed upstream of the compensating filter. The purpose of this installation is to rotate the (initially longitudinal) spin by 90° out of the accelerator plane. This spin rotation is kept fixed. Then a longitudinal magnetic field B_{long} that is created by a solenoid will rotate the spin towards transverse orientation in the accelerator plane and the second Wien filter compensates the $g - 2$ precession. By reversing the current of the solenoid, a 180° spin flip can be obtained with no first order change

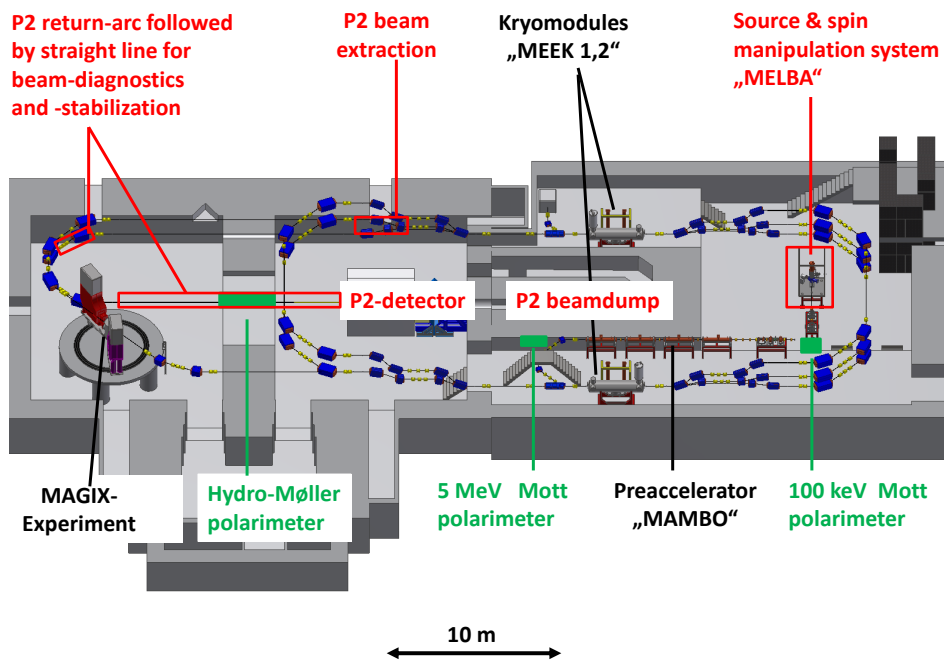


Fig. 10. View of the MESA accelerator. Areas of specific importance for P2 are indicated. Electron optical components are labelled in black colour, beam and spin control in red and polarimeters in green.

of electron optical properties of the solenoid - the focusing strength is $\propto \int B_{long}^2 dl$. This spin reversal is independent from the optical spin reversal that is generated by helicity switching at the source. The procedure serves to provide a further check for beam systematics. This method was developed for the parity experiments at JLab [66]. After spin manipulation the beam is directed via an α -magnet to the beam bunching and collimation system which prepares the beam for RF-acceleration in the pre-accelerator, the so-called MilliAmpere BOoster (MAMBO).

Space is available behind the α -magnet in order to install a double scattering Mott polarimeter. It operates at the source energy of 100 keV and will be reached by the beam after switching off the magnet. Behind MAMBO we will set-up a single scattering Mott polarimeter which uses a beam energy of 5 MeV. These polarimeters require transverse spin polarization which is provided by switching off the second Wien filter. The last polarimeter in the system, the Hydro-Møller, requires longitudinal polarisation which coincides with the experimental requirements. More details concerning polarimetry can be found in Sect. 3.2. Most of the components of MELBA, including the two Wien filters, are either ready for commissioning or already in operation in different test set-ups.

After three passages through the cryomodules the beam is extracted via a magnetic chicane towards the P2 beam-line. It should be noted that this part of MESA (together with two of the recirculation arcs) is located in the P2 experimental hall. Handling the radiation levels coming from the target seems feasible since only relatively robust accelerator components are installed in this region. More

demanding, but also feasible, is the task to shield all beam-line components from the magnetic fringe field of the P2 solenoid, which has a large aperture.

After extraction, the beam is directed away from the P2 experiment into the MAGIX hall. The main idea is to obtain a long straight line in front of the experiment for beam diagnostic and stabilization purposes - see Sect. 3.3 for details. The final 180° bend in front of the experiment can be used to create a large longitudinal dispersion which is needed for energy stabilization. The straight line will also contain the Hydro-Møller polarimeter that occupies ≈ 2.5 m of beam line by its cryostat. The cryostat can be installed in a rectangular opening (5 m width, 0.8 m height) in the wall between the MAGIX and the P2 hall, see Fig. 10.

3.1 Polarized source

Though a source has recently been put into operation that is capable to achieve the anticipated maximum beam currents of MESA of 10 mA [67], such a device is not mandatory and maybe not even advisable for P2, since it incorporates increased technological risks. On the other hand, the source developed for MAMI [68] represents a sufficient basis for the P2 experiment. This source has been operated for decades at the MAMI accelerator [69] and has produced beams with nearly 90% of polarization and currents well above the level needed for P2. An important factor is the operational lifetime that can be expected. The ability of the photocathode to convert light quanta into

electrons, the so-called quantum efficiency, decays due to radiation damage which in turn causes a finite operational lifetime of the source. Operation of the MAMI source at 200 μA [70] has revealed a charge lifetime of 200 C - that is 200 Coulombs of charge can be produced while the initial quantum efficiency drops to $1/e$, i.e. to about 37%, of its initial value. This can be handled even with the existing laser system of the polarized source at MAMI which is able to deliver 300 mW. A moderate quantum efficiency of 0.5% (corresponding to a photo-sensitivity of 3 mA/Watt at the operational wavelength of 778 nm) is assumed for the GaAs/GaAsP superlattice photocathode that has to be employed to achieve polarizations surpassing 85%. Then, after one lifetime, less than 200 mW of laser power on the cathode will be necessary. At this power level some improvement of heat transfer from the photocathode is needed in order to limit a temperature increase which reduces the lifetime. We consider this feasible, which will allow to maintain the 200 C of lifetime - this value was observed with a cathode of much higher initial quantum efficiency. Our estimation of the continuous operation during P2 is therefore more than 12 days. This is matching the run-time schedule foreseen for MESA which has a period of 2 weeks composed of 12 days of run-time + 2 days of maintenance. Since the photocathodes can be regenerated within a very short time [68], the long term operation of P2 with a design based on the MAMI source is feasible. The source has been built with several improvements concerning, in particular, a better vacuum system. It has been thoroughly tested and has indeed obtained improved lifetime parameters [71]. The source is currently used in a separate lab to investigate the double scattering Mott polarimeter foreseen for P2 and will be installed at the MESA site when the civil construction work for the experimental halls of MESA is finalized.

3.2 Polarimetry

The concept of polarimetry for P2 was sketched in [72]. A chain of three polarimeters will provide for three independent polarization measurements achieving an absolute accuracy of better than $\Delta P/P = 0.01$ with each polarimeter. The chain consists of a double Mott polarimeter at 100 keV beam energy, a single scattering Mott polarimeter at 5 MeV and a Møller polarimeter which is located directly in front of the P2 experiment. The latter, the so-called “Hydro-Møller” will have online capability. The others are invasive devices but will allow very fast measurements. Laser-Compton back-scattering which is a very expedient way of polarimetry at energies above 1 GeV is not promising in our case due to the small asymmetries caused by the low beam energy. We discuss the individual features and the status of the polarimeters in the following subsections.

3.2.1 Double scattering Mott polarimeter

An intriguing approach towards high precision polarimetry is to use double scattering. The idea is to measure

the effective analyzing power S_{eff} of a scattering experiment. All other types of polarimeters have to rely on (i) a theoretical determination of the analyzing power of the elementary scattering process and (ii) a careful determination of the deviations from the elementary process in the real experiment. The double scattering experiment does away completely with the first and offers considerable advantages with respect to the second aspect.

The method was thoroughly analyzed in a series of articles by the group of Prof. Kessler at University of Münster [73, 74, 75]. The measurement works in the following way. A first elastic scattering of an unpolarized beam produces a polarized scattered beam with a vertical polarization $P_{Scat} = S_{eff}$. This polarization is in general lower than the theoretical analyzing power of the process S_0 due to the spin diffusion in the target of finite thickness. This creates several of the systematic errors in conventional Mott polarimetry whereas it is - at least in principle - not important in this case. The secondary beam is directed under a given solid angle to an identical target where a scattering asymmetry is observed under the same solid angle. Provided that the two scatterings - notably the targets and the solid angles - can be made identical, the observed asymmetry A_{obs} is given by

$$A_{obs} = S_{eff}^2 \quad (46)$$

This is due to the equivalence of analyzing power and polarization power in elastic scattering. Then, S_{eff} is obtained by taking the square root of the observed asymmetry, the sign of the analyzing power is known from theory. A challenge in such an experiment is the control of false asymmetries since the spin in the second scattering cannot easily be reversed (the initial beam is unpolarized!). However, an ingenious scheme was designed in [73] from which a control of such asymmetries in the range of 0.1% can be achieved.

After this procedure the targets are calibrated and each of them can be used to analyze a polarized beam with the effective analyzing power S_{eff} . At 120 keV, an accuracy of $\Delta S_{eff}/S_{eff} = 0.24\%$ was claimed for the secondary target [74].

Kessler’s group used primary beams of up to 120 keV. This scheme cannot be extended to much higher energies due to the rapidly falling elastic cross section. The method is therefore restricted to energies typical for polarized sources and is, of course, invasive. The MESA source will be operated at 100 keV which is well suited to the application of the method. Once S_{eff} is determined, the polarized beam will be analyzed in single scattering, where measurements with statistical accuracies of $<1\%$ are possible within minutes. The beam current in such measurements is several orders of magnitude smaller than needed for P2. To make sure that the spin polarization of the electron beam does not change, we will make use of the large dynamic range of the 5 MeV Mott polarimeter discussed in the next section.

The apparatus of the Münster group was transferred to Mainz [72] where its applicability for the P2 experiment at the MESA accelerator is tested. It has been demonstrated

that the mechanically complicated apparatus can be operated very reliably together with the 100 keV polarized source of MESA. Statistical errors of $\Delta S_{eff,stat.}/S_{eff} < 0.5\%$ have been achieved, no indications of drifts of the apparatus during the several days long calibration procedure were observed. The extracted effective analyzing power is in satisfactory agreement with the values observed by the Münster group [74] but not with S_{eff} measurements by us and other groups that are based on polarized single scattering [76]. We will address this issue by a direct comparison of the two methods in the near future [77].

Double scattering offers another attractive feature that may allow to reduce the systematic error further. It was observed by Hopster and Abraham [78] that additional observables can be gained if a polarized primary beam is employed, provided that vertical beam polarization can be flipped while maintaining its absolute value. For the polarized source at MESA this is done by switching the circular polarization (σ^\pm) of laser light that excites the photocathode of the source. It is assumed that under this helicity flip the following condition holds for the vector of the electron beam polarization:

$$\mathbf{P}_{\sigma^+} \rightarrow -\mathbf{P}_{\sigma^-}. \quad (47)$$

The primary target is considered as an auxiliary target which does no longer have to have the same effective analyzing power as the second one (S_{eff}), but has a value S_T instead. The double scattering experiment with unpolarized beam now yields

$$A_1 = S_T S_{eff}. \quad (48)$$

One can also move the second target including its detection system into the primary beam path, then observing

$$A_2 = P_0 S_{eff}. \quad (49)$$

Scattering on the first target with the two input polarizations $\pm P_0$ yields different secondary beam polarizations $P_{\uparrow,\downarrow}$ which depend on S_T and on the depolarization factor of the auxiliary target α , a fact that was observed in Ref. [75]:

$$P_{\uparrow} = \frac{S_T + \alpha P_0}{1 + P_0 S_T}, \quad (50)$$

$$P_{\downarrow} = \frac{S_T - \alpha P_0}{1 - P_0 S_T}.$$

Taking this into account, more asymmetries can be measured by double scattering:

$$A_3 = P_{\uparrow} S_{eff}, \quad (51)$$

$$A_4 = P_{\downarrow} S_{eff}. \quad (52)$$

While measuring A_3, A_4 one can also monitor the scattered beam current from the auxiliary target which is nothing else than the single scattering asymmetry:

$$A_5 = P_0 S_T. \quad (53)$$

One finds that the extension proposed in [78] implies considerable advantages:

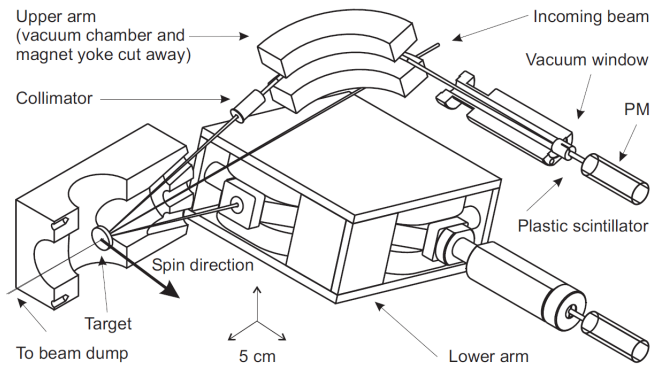


Fig. 11. Schematic set-up of the MAMI 3.5 MeV Mott polarimeter [79]. Backgrounds are suppressed by double-focusing magnetic spectrometers.

- The five observations A_1, \dots, A_5 depend on the four unknowns S_T, S_{eff}, P_0 , and α . They result in an over-determined system of equations hence allowing to extract the unknowns in five independent ways, providing systematic cross-checks.
- The condition of identical targets is revoked, but it is replaced by the symmetry condition expressed in Eq. (47). The equality of circular polarizations of the photo-exciting light can be determined very accurately ($<0.1\%$). In principle a solid state effect that would lead to significantly unequal spin densities after photo-absorption cannot be ruled out, but does not seem very likely.
- The set of double scattering observables also can help to check the validity of Eq. (47) for our experimental set-up. Note that the validity is implicitly assumed in virtually all polarized scattering experiments, including P2.

It was shown in [75] that the auxiliary target thickness can be varied by a factor eight without any observable influence on the extracted analyzing power of the second target at a level $<0.4\%$. The hard to achieve condition of identical target thicknesses is therefore not mandatory for precision polarimetry in double scattering.

3.2.2 Single scattering Mott polarimeter at 5 MeV

The design of the 3.5 MeV Mott polarimeter [79] at MAMI can be used at MESA with small adaptations since the beam energy will be similar. An advantage of the polarimeter is its compact size, see Fig. 11.

The calibration of the analyzer requires measuring the scattering asymmetry of targets of different thicknesses. The polarization is then determined by extrapolating the asymmetry to foil thickness zero (A_0) and then obtaining the beam polarization by using $P = A_0/S_0$, with S_0 being the theoretically calculated analyzing power of Mott

scattering on the single atom. The three major sources of uncertainty are (i) background (ii) the uncertainty of extrapolation and (iii) the theoretical uncertainty of S_0 . Based on the results from the 3.5 MeV polarimeter we can state that

- The background contribution can be reduced below 0.5% by dedicated experiments and improved Monte Carlo simulation.
- The spin diffusion which reduces the effective analyzing power with target thickness can nowadays be modelled quite accurately starting from first principles [80, 81]. It is therefore no longer necessary to rely on fits to the data which have always caused significant uncertainties since there is no good motivation to prefer a specific fit function. It is therefore possible to suppress the uncertainty associated with the extrapolation below 0.5%.
- The remaining factor is the theoretical uncertainty of the analyzing power (called Sherman-function, S_0). An energy of several MeV is well suited for precision calculations since neither the nuclear nor the electronic details of the atom contribute significantly [79, 82]. However, at multi-MeV energies and for high- Z targets, a possible contribution of radiative effects has to be addressed. Though our findings and those at Jefferson Lab [83] give reasons to assume that radiative effects are not important at the 1% level, no comprehensive theoretical treatment exists. Due to the revived interest in such calculations one can hope for improvement in the future. Progress has already been achieved in [82], where the contribution of vacuum polarization has been calculated to be less than 0.5%.

Overall one can expect that the absolute accuracy of our single-scattering device will be pushed to below 1%.

A virtue of the multi-MeV Mott is its dynamic range and good reproducibility. Figure 12 demonstrates that consistent results at the sub-percent level can be achieved while varying the current between 6 nA (order of magnitude intensity that is used for the double Mott) and 50 μ A which approaches the design current of P2. Note that targets were changed to thinner ones while increasing the current to avoid dead time corrections. Such measurements will serve to connect the results of the double Mott with the Hydro-Møller polarimeter which is discussed in the next section. Efficient measurements with this polarimeter are only possible at currents exceeding 20 μ A and, of course, current-dependent effects cannot be excluded also in this device, see for instance [84]. An illustration of the problem is the slight change of asymmetry at the largest beam currents (Fig. 12) that could be caused by heating up of the photocathode due to the high laser intensity but might also be related to changes of the local background due to space charge effects in the 3.5 MeV pre-accelerator. By comparing two polarimeters with high current capabilities such effects can be identified.

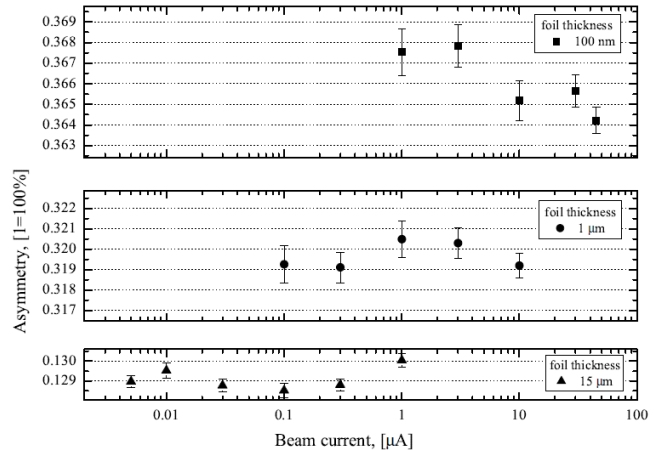


Fig. 12. Asymmetries in the MAMI 3.5 MeV Mott polarimeter as a function of the primary current. Variable target thicknesses are used to limit the count rate. (Figure from Ref. [79]).

3.2.3 Hydro-Møller target

We want to replace the ferromagnetic target of a conventional Møller polarimeter by trapped polarized hydrogen atoms, an idea that was proposed by Chudakov and Lupov [84]. Hydrogen atoms are injected into the fringe region of a solenoid with a magnetic field \mathbf{B} pointing along the beam direction. The hydrogen atoms carry a magnetic moment $\boldsymbol{\mu}$ which makes them experience a force $\mathbf{F} = -\nabla(\boldsymbol{\mu} \cdot \mathbf{B})$ which pushes the high field seeking hyperfine states $|a\rangle$ and $|b\rangle$ (see Eq. 54) towards the homogeneous field region. One of the injected states enters with both electron spin orientations, hence diluting the electronic spin polarization,

$$|a\rangle = \alpha |\downarrow, \uparrow\rangle + \beta |\uparrow, \downarrow\rangle, \quad (54)$$

$$|b\rangle = |\downarrow, \downarrow\rangle. \quad (55)$$

Here double arrows denote electron spins and the single-line arrows denote nuclear spin. The parameters $\alpha = \sin \theta$, $\beta = \cos \theta$ can be calculated via $\tan(2\theta) = 0.05/B[T]$. Note that θ varies between $\pi/4$ and $\pi/2$ when B changes from $0 \rightarrow \infty$. Since the relative density of particles in the ‘wrong’ state $|\uparrow\downarrow\rangle$ is $\propto \beta^2$, it is strongly reduced by the magnetic field. A large field will thus lead to an electron polarization of $|P_e| = 1 - 10^{-5}$ at 8 Tesla. This high-purity electronic spin ensemble represents the main advantage with respect to existing Møller polarimeters.

Figure 13 sketches the working principle. Hydrogen atoms are created, for instance, by a thermal dissociator and are injected into the fringe field of a strong solenoid. While entering the homogeneous part of the solenoid they are cooled by wall collisions to a temperature of ≈ 0.3 K so that they cannot escape in the axial direction anymore. Normally, the wall collisions would lead to adsorption and/or recombination of the hydrogen atoms, but

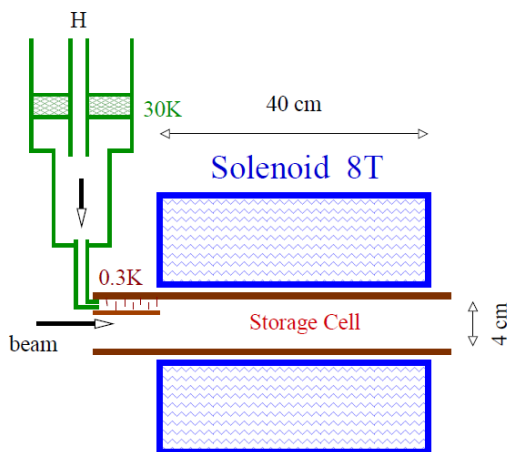


Fig. 13. Schematic of the Hydro-Møller atomic trap [84].

these effects are strongly suppressed when the wall is covered with a superfluid film of helium. It is for the same reason that hydrogen is efficiently stored since the particles are enclosed radially by the wall. A very low temperature of the helium film is required to keep the vapour pressure of helium low enough since helium adds unpolarized electrons to the target.

Traps of this type have been built and achieved target densities of nearly $3 \times 10^{15} \text{ cm}^{-3}$ in volumes of 100 cm^3 [85]. They have however never been operated with a high power electron beam so far.

The calculations in [84] lead to the conclusion that even when interacting with the $150 \mu\text{A}$ beam foreseen for P2, a target area density of 10^{16} cm^{-2} , and high spin purity can be maintained. To achieve this, a first task is the control of depolarizing resonances due to interaction with time varying magnetic fields from the beam time structure. This effect can be controlled by tuning the magnetic field in a way that the frequency of hyperfine transitions does not coincide with the beam harmonics. A more challenging issue is linked to the production of slow electrons or charged ions with at least one electron (H^- , H_2^- , H_2^+) within the beam profile. Scattering reactions from such electrons will dilute the Møller signal. In contrast to neutral hydrogen their diffusion out of the beam area is suppressed since they are bound within the cyclotron radius which is smaller than the beam radius. A possible solution is to add a small transverse electrical field ($E \approx 1 \text{ V/cm}$) in order to cause an $E \times B$ drift which removes the charged particles from the beam. It is technically challenging to provide the E -field, since insulated electrodes must be maintained at a temperature of 0.3 K while also covering them with superfluid helium. If this can be achieved, a contamination of unpolarized electrons of less than 0.01% is expected.

The low area density allows online operation since the beam is not significantly deteriorated by the target atoms. When the trap is irradiated with the full current of P2,

a statistical precision of $<0.5 \%$ within less than 1 hour could be achieved, if the solid angle of conventional Møller polarimeters is assumed.

The completely polarized target eliminates two main error sources of existing Møller polarimeters [86], namely the uncertainty of the target polarisation [86] and the enhancement of valence electrons in the detected sample of electron pairs by the Levchuk effect [87]. These represent about 80% of the error budget of the best existing Møller polarimeters [86], which opens the perspective to achieve accuracies well below $\Delta P/P = 0.5 \%$.

3.2.4 Status of the Hydro-Møller target

Generating the cryogenic environment for the Hydro-Møller is not easy for several reasons, some of the most important ones are:

- The trap must be open to let the beam pass which will expose the 0.3 K surfaces to thermal radiation. The apertures cannot be made arbitrarily small in order to avoid beam losses.
- Though the direct deposition of heat by the beam in the target is not a major issue [84], the main heat source is recombination of hydrogen atoms to H_2 (4.5 eV per molecule). Taking into account the planned densities and leaving some headroom for inefficiencies of the refrigerator and limited heat conduction towards the trap surface, we find that a cooling power of 60 mW at 0.25 K is needed.
- The hydrogen dissociator and the solenoid must be incorporated.
- The height of the refrigerator must not exceed 60 cm since, according to the present design of the P2 beamline, it has to be installed in a slit-shaped breakthrough between experimental halls (see Fig. 10). The horizontal orientation of the refrigerator components is especially challenging.
- The polarimeter will have to run for very long times continuously. Since maintenance and repair will be difficult once the polarimeter is integrated in the beamline, only very reliable components and procedures are recommendable. Glued interconnections and indium seals should be avoided. This leads to a large effort in prototyping of the many individual components.

Figure 14 shows a schematic of the device which is currently under construction. The design has been developed after a long series of consultations with cryostat experts from Dubna, JLab and CERN.

An optimized pre-cooling circuit based on evaporation of ^4He at 1.25 K will minimize the amount of liquid helium needed for operation to less than 10 l/hour . Concerning the mixing circuit, the desired cooling power requires a mass flow of 25 mmol/s of ^3He , the total amount of liquid ^3He will be $\approx 100 \text{ cm}^3$. Several parts have already been manufactured (see Fig. 15) and, based on these successful examples, we believe that assembly of the refrigerator can start early 2019. First test runs of the refrigerator are foreseen end of 2019 with the final objective to obtain a ready-to-operate target by end of 2020.

3.2.5 Hydro-Møller spectrometer

The Hydro-Møller target described above provides the opportunity to monitor the electron beam polarization in-situ with fractional accuracy well below 1%. The Hydro-Møller spectrometer must detect the electrons that result from the longitudinally polarized beam electrons scattering from the practically 100% longitudinally polarized target electrons. One can then monitor the electron beam polarization by constructing the asymmetry A_m

$$A_m = \frac{\sigma^{\uparrow\uparrow} - \sigma^{\uparrow\downarrow}}{\sigma^{\uparrow\uparrow} + \sigma^{\uparrow\downarrow}} = P_T P_B \frac{\sin^2 \theta (7 + \cos^2 \theta)}{(3 + \cos^2 \theta)^2} \quad (56)$$

where σ is the rate of scattered electrons. The first and second superscripts depict the sign of the beam and target electron helicities, respectively. P_T is the $\sim 100\%$ target electron polarization, P_B the beam polarization we seek to monitor and θ is the scattering angle in the electron-electron scattering center-of-mass frame.

In the following, we describe a conceptual design for the spectrometer. The analyzing power is maximum at a center-of-mass scattering angle of 90° , corresponding to a scattered electron momentum of 77.5 MeV and a scattering angle of approximately 5° in the laboratory frame. Due to the large field integral of the Hydro-Møller solenoid experienced by the scattered electrons, the traditional method of picking up a small solid angle byte around the 5° lab scattering angle followed by two dipoles is insufficient to sample the Møller electrons from the full length of the target. As we describe below, we have found that a focusing quadrupole centered on the beam axis, followed by a dipole chicane, will allow us to isolate the Møller electrons of interest in a region that can be instrumented with segmented detectors while allowing the primary beam to pass to the liquid hydrogen target in front of the main P2 solenoid.

Optics concept. An optics simulation was performed using a simulated superconducting solenoidal magnet with

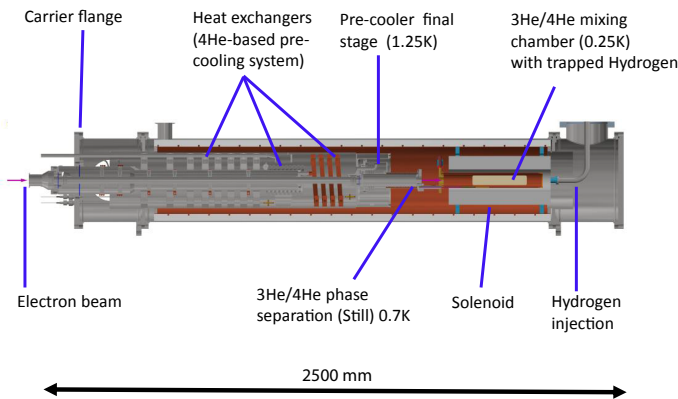


Fig. 14. Schematic of the refrigerator for the Mainz Hydro-Møller. Only positions of major components are indicated.

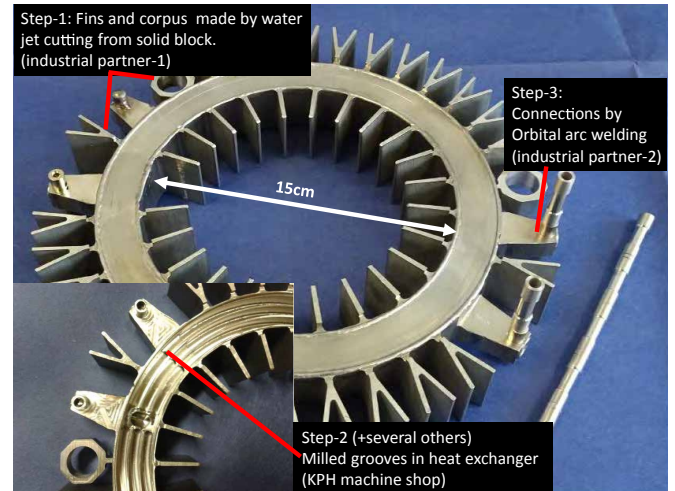


Fig. 15. All welded stainless steel heat exchanger disk for the pre-cooling circuit of the Hydro-Møller refrigerator. We indicate several techniques necessary to accomplish this component, illustrating the collaboration between external companies and our institute during the fabrication.

a simplified geometry and a maximum field of approximately 8 T. Azimuthal symmetry was assumed with a coil radius of 5 cm and axial length of 20 cm with no magnetic field-return components. The resulting 3-D field map was included into a Geant4 simulation which included an electron pair generator for a 140 MeV electron beam and a 20 cm long target. Events were generated uniformly along the target length with an energy and angles corresponding to Møller kinematics over the full center-of-mass phase space. It was empirically observed that there is an approximate linear correlation between the incident radial position at a transverse plane downstream of the target and the direction tangent to the radial direction for particles near the center-of-mass scattering angle of 90° . It was also observed that the azimuthal momentum component was small relative to the other components.

The particles therefore appear as if they were emanating from a point with no subsequent magnetic field interaction. This situation implies that to first order, a simple single-element optics designed for 77.5 MeV charged particles can be used to focus these particles into a narrow detector region. Particles which do not match these characteristics, such as lower or higher energy Møller electrons or electrons from non-radiative elastic proton scattering are naturally separated.

A quadrupole magnet with a focal length equal to its position downstream of the target center transforms the apparent point-emanating electron trajectories to a beam-parallel transport. These beam-parallel electrons can then be separated by dipole magnets and transported to a detector off-axis of the beam. A quadrupole doublet might possibly extend the azimuthal coverage beyond a single plane, though this remains to be studied.

Due to the small scattering angles, the particle envelope of interest will naturally only span several centimeters

transverse to the beam and should not require significant additional focusing. Such a concept can likely be adapted to a system with a dipole upstream of the quadrupole using a chicane configuration. The above ideas are incorporated to the conceptual schematic in Fig. 16

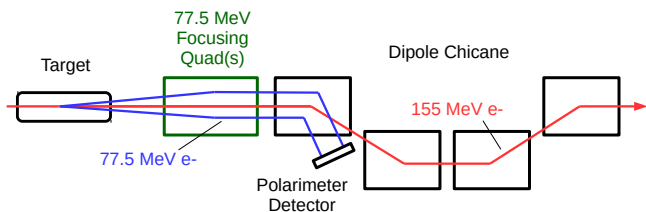


Fig. 16. An optics concept for separating and focusing 90° center-of-mass angle Møller electrons. For 77.5 MeV Møller-scattered electrons, the target’s 8 T solenoidal field induces a linear correlation (see text) that results in trajectories that appear as if originating from a point target.

Additional studies are ongoing to determine ideal field values and their tolerances, the appropriate collimation system, effects of radiative events from Møller and elastic proton scattering which contribute irreducible backgrounds, the detection of coincidence events, and anticipated rates and analyzing power. Preliminary studies indicate that, given the size of A_m is of the order of 0.5 to 0.6, it should be feasible to design a spectrometer, collimator, and detector system that will obtain a rate for the Møller electrons of interest $\sim 0.1 - 1$ kHz during production running. A fractional statistical uncertainty on A_m at the level of 0.1% then could be obtained within one hour. This will make feasible detailed systematic studies and careful monitoring of the variations in beam polarization so that a determination of the beam polarization integrated over the running period with a total systematic error $\sim 0.5\%$ should be possible.

3.3 Beam control

An apparatusive asymmetry A^{app} will arise from helicity correlations of the six beam parameters position x , y , angle x' , y' , intensity I , and energy E at the P2 target. Therefore an accurate, continuous measurement of the beam parameters is mandatory to determine A^{app} and correct for it. Such a correction should not exceed a certain fraction of the physics asymmetry A^{exp} and its uncertainty must not exceed $\Delta A^{\text{app}} = 0.1$ ppb as given in Tab. 1.

There are two possibilities to keep the correction small. First, beam parameter fluctuations can be actively suppressed by feedback systems. This was done successfully in the A4 experiment [88] at MAMI, using analog feedback loops for position, angle, intensity and a digital loop to stabilize the beam energy. However, this approach removes helicity-correlated as well as non-helicity correlated beam fluctuations. Since the latter are needed to decorrelate the individual contributions A_i^{app} to the total ap-

parative asymmetry, suppressing them can increase the uncertainty ΔA^{app} of the correction.

A second possibility is to measure the helicity-correlations of all beam parameters online. Then the helicity signal can be used for a feed-forward suppression of the helicity-correlated fluctuations.

In the following we will describe some of the technology and expertise that already exists from running the existing MAMI accelerator and the recent A4 parity violation experiment. We will then discuss dedicated tests with a new digital data acquisition and control system. From these results we will see that we can be confident to fulfil the requirements of the P2 experiment on the beam parameter stability and measurement.

3.4 Proposed beam control system

The operation of the existing MAMI accelerator and the former A4 parity-violation experiment rely on measuring the beam parameters with cavity beam monitors: beam current monitors (BCM) can be used for beam intensity and also for beam phase measurement, while beam position monitors (BPM) provide measurements of beam position and angle (from differences between two BPMs). Due to our experience and the good performance and reliability with cavity monitors we will also use them for instrumentation of the P2 beamline at MESA. The cavities for MESA will be based on the design of the cavities used at MAMI, but with resonance frequencies adapted to MESA (1.3 GHz or 2.6 GHz) and with enhanced vacuum properties (bakeable design) and better tuning capabilities.

Due to the tiny physics asymmetry A^{exp} we believe that a digital system for the beam monitors is mandatory. Such a system provides flexibility and can be adapted to the exact needs of the experiment. If all beam monitors of the accelerator and experiment beamline are read out digitally, all of these data will be available for diagnostics to both, the accelerator operator as well as to the experiment. This will be of great importance in the commissioning phase of the experiment.

3.5 Beam monitor tests at MAMI

In order to develop and test a new, digital data acquisition and control system for MESA we instrumented 20 m

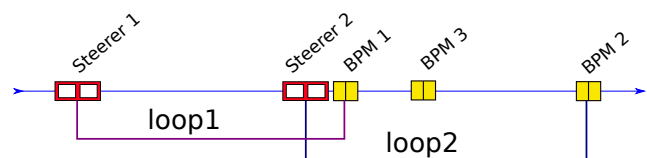


Fig. 17. Control system components in the beamline. Steerer 1 and BPM 1 form a first loop, which controls the position on BPM 1. Steerer 2 and BPM 2 form the second loop, which controls the position on BPM 2. This, in fact, controls the angle of the beam. BPM 3 is used as an unbiased observer.

of beamline at the existing MAMI accelerator with additional beam monitors and steering magnets. For feedback tests digital control loops have been arranged as shown in Fig. 17. The beam has an energy of 180 MeV which is close to the 155 MeV planned for the P2 experiment. We explored different techniques for down-conversion of the cavity monitor RF signals to baseband, employing direct down-conversion as well as IQ demodulation with and without employing an intermediate frequency. One advantage of IQ demodulation via an intermediate frequency would be the decrease of baseband noise/interference contributions collected on the signal path.

To gain significantly higher accuracy we use fast ADCs and DACs (both 125 MSa/s, 14 bits) as part of a control system that is established on an FPGA. This approach enabled us to control the beam in the classical feedback as well as in feed-forward loop. The flexibility of such a digital system allows for small remote modifications as well as for the implementation of new features in the system without the need for a redesign of electronics. To avoid the tedious development of the hardware consisting of FPGAs, ADCs, DACs, and periphery for communications (possibly even a CPU), we decided to use a commercially available board (RedPitaya) for the moment to carry out our measurements.

3.5.1 Accuracy results

A key issue is the achievable accuracy of our data acquisition system. A digital signal always carries information as well as noise stemming from variation in voltage supply, clock jitter, and the quantization error. The ADCs show 2.5 bits of noise and 11.5 bits of ENOB (effective number of bits) which corresponds to the effective resolution.

For the P2 experiment a beam position or beam current data rate of the order of few times the helicity flip rate is sufficient, far below the 125 MHz our ADCs provide. Therefore we can average over N samples, improving the effective resolution, and record only these average values with 16 bits resolution, of course, at a data rate decimated by the factor N . With 125 MHz sampling rate, a decimation factor of 8192 would give a data rate of about 15.2 kHz, which was used in our test measurements. The gain in effective resolution can also be calculated. For example to reduce the error σ by half one needs to increase the number of measurements N four times to $4N$:

$$\frac{\sigma}{\sqrt{4N}} = \frac{1}{2} \frac{\sigma}{\sqrt{N}} = \frac{\sigma}{\sqrt{4N}} \quad (57)$$

under the condition that the noise is white noise.

In the following paragraphs we discuss the different sources of noise contributing to the overall noise budget. We refer to beam monitor BPM 2 which revealed a sensitivity of 640 mV mm⁻¹ at 10 μ A beam current. At 150 μ A beam current the sensitivity would be 9.6 Vmm⁻¹. From the sensitivities one can convert each contribution to beam position uncertainty.

ADC effective resolution. We carried out measurements of the ADC noise without any further electronics attached. This allows to find out what the theoretically achievable resolution limit was, if none of the other components would add any noise. Table 3 shows the effective resolution of data acquisition in bits, as well as converted to the expected effective beam position resolution in nm at 150 μ A beam current.

| bits | W/ μ V | W/nm @150 μ A |
|------|------------|-------------------|
| 0.42 | 40.8 | 4.3 |

Table 3. Maximal possible resolution for a decimation of 8192 in number of bits and μ V. W stands for signal width. The measurement was taken with unplugged BPM electronics. The width in nm is the extrapolated contribution to the beam's uncertainty stemming from the effective resolution, if measured at 150 μ A.

Signal width without beam. Noise measurements with cavity beam monitors were performed without beam to determine the total noise of the full acquisition system. The signal width contains contributions coming from the electronic components of the IQ-demodulation, such as mixers, amplifiers, splitters, and connections. Reducing the distortions collected on the transfer path through the hall, we have carried the signals differentially. Table 4 summarizes the signal width without beam.

| bits | W/ μ V | W/nm @150 μ A |
|------|------------|-------------------|
| 0.97 | 59.8 | 6.2 |

Table 4. Signal width without beam for decimation of 8192. This data derives from a measurement with fully plugged electronics but switched off beam. Similar to the effective resolution the signal width in nm represents the extrapolated contribution to the beam width caused by electronic noise, if measured with 150 μ A.

Signal width with beam. Finally we discuss measurements of the beam position with a beam current of 5 μ A. During these measurements we also employed our digital feedback loop to stabilize the beam position and angle in our test beamline.

Evidently the beam position fluctuation creates a width that is 100 times larger than the electronic noise. One can therefore extrapolate the uncertainty of the beam position (or helicity-correlated beam position difference) to be of the order 0.3 nm after 10 000 h of data taking. For a perfectly symmetric P2 detector one can estimate the

| bits | W/mV @5 μ A | W/ μ m | W/nm @10 kh |
|------|--------------------|------------|----------------|
| 3.15 | 6.25 | 54.3 | 0.29 |

Table 5. Signal width and beam width of a stabilized 5 μ A beam measured with BPM3. The table shows results from measurements with a beam current of 5 μ A in V and nm as well as the estimated mean value of the width after 10 000 h measuring time. The control unit was the PID element of the FPGA.

resulting systematic error from this uncertainty taking into account only the geometry effect from the beam position fluctuations, neglecting magnetic field and detector properties. This gives an extremely small value, about 0.003 ppb. It is now necessary to fully model the experiment, including magnetic field, alignment errors of the beamline, beam monitors, and detector modules. This will allow to determine the sensitivity of the experiment on beam position fluctuations.

Beam current. Also a beam current monitor was read out with the new DAQ system. A Short Term Asymmetry (STA) can be determined straight from the beam current. STAs are calculated from quadruplets, a pattern of helicity states (either positive or negative) of 1 and 2 ms length in the following order: $+-+$ and $-++-$. Each of our quadruplets is 4 ms long and 9×10^9 quadruplets would correspond to 10 000 hours measuring time.

Table 6 shows the results for the uncertainty of the STAs. The measurements were carried out at a beam current of 10 μ A and the expected width for a current of 150 μ A was calculated. The validity of such an extrapolation is motivated by our evaluation of beam current monitor calibration data from the A4 experiment. The results in Tab. 6 show that the beam current stability at MESA has to be improved compared to MAMI.

From Tab. 6 one can read a projected precision of the beam current measurement for 10 000 h of 0.3 ppb at MAMI. For P2 at MESA this still needs to be improved by about a factor of ten. We believe that this is possible, because at MAMI the beamline between polarized electron source and injector LINAC contains a number of critical apertures. Therefore even small beam position fluctuations already cause significant beam current fluctuations. The design of the MESA low energy beam apparatus (MELBA) avoids such aperture limitations. In addition, for MESA a more sophisticated laser optics system for the polarized electron source will allow to keep beam position fluctuations much smaller in this critical part of the beamline.

Beam energy. For the beam energy stabilization the 180° P2 return-arc (see Fig. 10) with maximal longitudinal dispersion, along with two beam phase cavity monitors will be used. A similar concept has proven successful at

| W/mV @10 μ A | W/nA | Δ STA/ppm @150 μ A | Δ STA/ppb @10kh |
|---------------------|------|----------------------------------|---------------------------|
| 6.0 | 5.9 | 28 | 0.29 |

Table 6. Width of the beam current and extrapolation of the expected STA at 150 μ A beam current and the average after 10 000 h measuring time.

MAMI for A4. So far, our measurements at MAMI did not consider beam energy yet (we have not positioned our monitors at positions with large longitudinal dispersion so far). However, we have estimated the effect of helicity correlated beam energy fluctuations in terms of apparative asymmetry in comparison to A^{exp} as shown in Tab. 7. In the A4 experiment, for instance, the beam energy was very stable (with a feedback system) and the corresponding contribution to ΔA^{app} in 10 000 hours would be safely below 0.1 ppb. However, we believe this is due to the intrinsic stability and longitudinal self-focussing properties of MAMI, which can not be expected for MESA. Therefore any possible source of beam energy fluctuation (noise) in MESA should be kept as small as possible. One can see from Tab. 7 that energy stability at MAMI was not an issue for A4, while even a helicity correlated change (or its uncertainty when correcting for it) of 1 eV at MESA would lead to a 23% effect at P2. Beam energy (helicity correlation or even noise) will probably be the most critical beam parameter at MESA.

However, an uncertainty of 0.1 ppb would correspond to 14 meV in 10 000 h, which is more than 10^{10} helicity gates. This gives an upper limit on the uncertainty of a single energy measurement of about 1400 eV or about 10^{-5} relative uncertainty at 155 MeV. A longitudinal dispersion of $10 \text{ mm}/10^{-3}$ can be routinely achieved in a 180° arc in the beamline. Such an arc then leads to a change in the longitudinal path length of 0.1 mm for 10^{-5} relative energy change. This 0.1 mm corresponds to a RF phase difference of 0.14° at 1.3 GHz to be detected in a helicity window of 0.5 ms which seems feasible. Alternatively the transverse dispersion of a 90° arc of about $3 \text{ mm}/10^{-3}$ would require measuring a beam displacement of 0.3 nm in 10 000 h, which is possible as can be seen from Tab. 5.

| $E_{\text{beam}} / \text{MeV}$ | $A^{\text{app}} / \text{ppb/eV}$ | $A^{\text{PV}} / \text{ppb}$ |
|--------------------------------|----------------------------------|------------------------------|
| 855 | 2.0 | ≈ 5000 |
| 155 | 6.8 | ≈ 30 |

Table 7. Estimated apparative asymmetries from helicity correlated beam energy fluctuations for P2 at MESA.

Expected asymmetry uncertainties for P2 from beam position. Table 8 shows the summarized results for asymmetry uncertainties expected after 10 000 h of measuring time. We expect improvement of the results for the beam

position by further increasing the degree of averaging. Also increasing the beam intensity of MESA compared to MAMI will lead to higher monitor sensitivities.

| | Width/nm | $\Delta\text{STA/ppb}$ per quadr. | $\Delta\text{STA/ppb}$ @10 kh |
|-----------------|-------------------|--------------------------------------|----------------------------------|
| eff. resolution | 4.3 | 0.83 | 8.7×10^{-6} |
| electronics | 6.2 | 1.2 | 1.3×10^{-5} |
| stabilized beam | 5.4×10^4 | 1.0×10^4 | 0.11 |

Table 8. Uncertainties of the asymmetry projected from A4 to P2 for the data with a decimation of 8192.

3.6 BPM cavity design

Cavity BPMs have been chosen as the measuring element of the control system because of reliable and long experienced operation at MAMI as well as the fact that they fulfil the requirements for a high precision experiment with high current. The most appealing properties of cavity BPMs are the non-invasive measuring technique and the possibility to measure very low currents. This comprises the possibility of increasing precision with increasing beam current. The measuring principle is based on amplification via resonance: A bunch of electrons flying through excites a spectrum in the cavity that depends on the length of the bunch. The shorter the bunch, the more higher frequencies are excited. Due to the repetition of the bunches, only modes with a frequency of multiples of the bunch rate frequency are excited positively and build standing waves inside the cavity. The inner design of the cavity determines which modes will survive, so that different purposes, such as phase and energy measurements can be pursued. For a BPM the TM_{110} -mode is of interest which can be sensed with antennas coupled to the cavity. In our case, the cavity is designed for a resonance frequency of 2.6 GHz (first harmonic) to keep its transversal dimensions reasonably small.

Combining a BPM with a feedback system, one has to take into account the characteristics of the whole loop, when designing the cavity. A BPM resembles a low pass with a cut-off frequency, where its bandwidth ends, and at which the phase shift is 45° . This cut-off frequency is determined by the quality factor of the cavity. It is the target of the control loop designer to keep amplification below one at frequencies at which the 180° shift of the whole loop is hit. Phase shifts of all components in the loop sum up. In simple terms, the threshold comes closer to lower frequencies the more low passes you find in the loop and the lower their cut-off frequencies are. Therefore, the design of the cavity has to make a compromise between high signal and high bandwidth. We decided to confine the bandwidth to 250 kHz. This is equal to a loaded Q factor of 5200. The loaded Q factor is determined by the Q factor

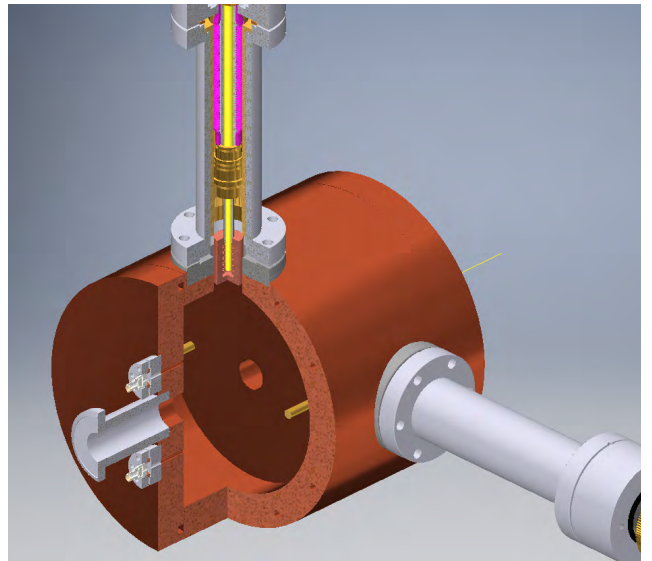


Fig. 18. Cavity design. The corpus is made of copper and all connections are of Conflat Standard, as the cavity must be bakeable to guarantee an ultra-high vacuum environment. The caps on each side are soldered to the corpus. The tuning pistons can be moved during operation to adjust the sensitivity of the BPM. Mode isolators inside the cavity suppress the TM_{110} -mode in perpendicular direction. Flanges with the antenna feedthroughs can be seen in front above and below the beam pipe. The outer diameter of the cylinder is 184 mm.

and the coupling β of the antennas:

$$Q = (\beta + 1)Q_L. \quad (58)$$

Simulations on a copper cavity show that the (unloaded) Q factor will be above 20000. The often used critical coupling of $\beta=1$, ensuring a high signal and high Q_L , is not sufficient here, instead the required bandwidth has to be approached by elongation of the antennas. As longer antennas decrease the resonance frequency, this has to be compensated with a tuning piston.

A picture of the current state of the design is shown in Fig. 18. The tuning pistons are attached perpendicular to the cavity and can change its volume. They can shift the resonance frequency within about 8 MHz. This can be used firstly to hit the exact frequency of 2.6 GHz and secondly to detune the frequency and damp the signal in order to save electronics, if high displacements are expected. The antennas are designed in pairs, as it is useful to subtract the two signals in order to double the outcome and annihilate remains of TM_{0x0} modes.

4 High Power Liquid Hydrogen Target

The P2 experiment requires a high luminosity liquid hydrogen (ℓH_2) target to measure a very small asymmetry with a very high precision. The cell geometry has to accommodate a full azimuthal angle about the electron beam direction and a polar angle range between 25° and 45°

Table 9. P2 target design parameters

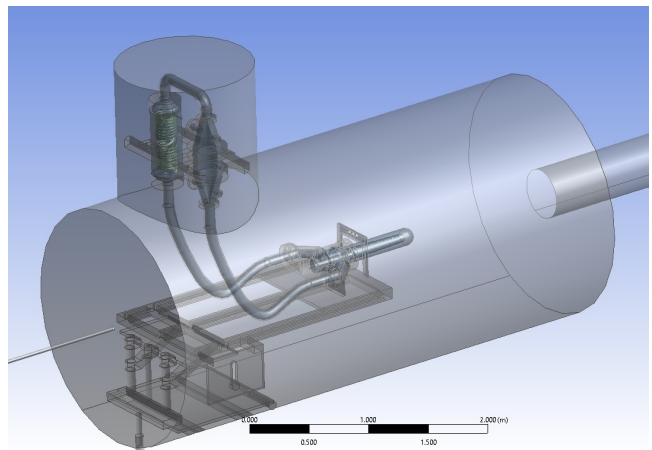
| | |
|---|-----------------------|
| Pressure/temperature | 2.4 bar / 20 K |
| Cell length | 60 cm |
| \dot{m} | < 2 kg/s |
| ℓH_2 pump head | < 0.1 bar |
| Beam area on target | 25 mm ² |
| HX cooling power | 4 kW |
| Target thickness | 4.3 g/cm ² |
| ℓH_2 ($\Delta\rho/\rho$) | < 2 % |
| ℓH_2 ($\delta\rho/\rho$) at 1 kHz | < 10 ppm |

Table 10. P2 target heat load

| Source | Value (W) |
|--------------------------------|-----------|
| Beam power in ℓH_2 | 3100 |
| Beam power in cell windows | 35 |
| Viscous heating | 275 |
| Radiative losses | 200 |
| Pump motor | 150 |
| Reserve heater power | 240 |
| Total heat load | 4000 |

along its full length with minimal materials in the path of scattered particles.

The total heat load of the target is estimated to be 4000 W, see Tab. 10. The heat deposited by the electron beam in the target cell materials can be calculated with the formula: $P = I\rho L(dE/dx)$, where I is the beam current in μA , ρ is the material density in beam in g/cm^3 , L is the material thickness in beam in cm, dE/dx is the collisional energy loss of electrons in the material in beam in $\text{MeV}/(\text{g/cm}^2)$ and P is the heating power in W. The electron beam will deposit 3135 W in the P2 target cell materials, which will make the P2 target the highest power ℓH_2 target in the world. A fluid target in a parity violation experiment produces two systematic effects that affect the PV asymmetry uncertainty: density reduction, denoted $\Delta\rho/\rho$ in Tab. 9, and density fluctuation, denoted $\delta\rho/\rho$ in Tab. 9. The density reduction effect is caused by the electron beam heating of the target fluid in the beam illuminated volume in the cell, which increases the temperature of the fluid and decreases its density. A 5 % ℓH_2 density reduction produces a 5 % luminosity reduction, which means that the experiment will have to run 5 % longer to achieve its proposed statistical uncertainty. The density fluctuation is a time dependent effect caused by the ℓH_2 density fluctuation due to the electron beam heating over time periods of the electron beam helicity. The ℓH_2 density fluctuation noise produces an enlargement of the PV asymmetry width [89], which increases the PV asymmetry systematic uncertainty. A 10 % increase in the PV asymmetry width due to ℓH_2 density fluctuation means a 20 % increase in the experimental running time to achieve the same systematic uncertainty as from a noiseless target. The P2 PV asymmetry is the smallest one that will have

**Fig. 19.** Configuration of the P2 target loop

been measured in all completed and proposed PVES experiments and with the smallest relative uncertainty too. In order to achieve this goal the P2 experiment requires a very high performance ℓH_2 target with no more than 2 % ℓH_2 density reduction and no more than 2 % PV asymmetry width enlargement or less than 10 ppm ℓH_2 density fluctuation noise over the time period of electron helicity reversal.

In order to satisfy the requirements of the P2 experiment a closed recirculating cryogenic ℓH_2 target loop will be designed, built and tested. The target will incorporate a control system to monitor, safely operate and control it during experimental commissioning and data acquisition periods. Hydrogen is a highly flammable gas in atmosphere in concentrations between 4 % and 74 % by volume and can produce explosions in concentrations between 18 % and 54 % by volume. Special safety measures will be taken in the design and control of the target system to mitigate hazards. The main components of the target loop are the ℓH_2 centrifugal pump, the heat exchanger (HX), the high power heater (HPH), and the target cell in beam. A model of the proposed ℓH_2 cryogenic P2 target loop can be seen in Fig. 19. In this configuration the 60 cm long ℓH_2 cell and its upstream manifold are supported on a table and placed inside the P2 solenoidal spectrometer. The supporting table will be instrumented with an all-metal 6 degrees of freedom alignment mechanism that will place the upstream and downstream windows of the long target cell within 0.5 mm each of their ideal positions respectively. The table will also be connected to a motion mechanism that will move the target cell in and out of the beam line and place solid targets in beam or no target in beam. The target cell manifold will connect with the rest of the target loop through stainless steel pipes that will have flexible sections in order to accommodate the target cell alignment in beam and the range of its motion mechanism. The HX, the HPH and the ℓH_2 pump will be supported inside of a vertical vacuum chamber but outside of the bore of the P2 magnet. These components of the cryogenic target loop will be thermally insulated from the shell of the vacuum chamber, which together with the vac-

uum in the chamber will reduce heat leaks and mitigate the target system cooling load. The target loop chamber and the P2 magnet will share vacuum space.

All previous PVES experiments or series of such experiments have designed, build, commissioned and operated their own target systems. Table 11 shows the design parameters of various PVES ℓH_2 targets. Before P2 the highest power ℓH_2 PVES target in the world was the QWeak target. The QWeak ℓH_2 target at Jefferson Lab was the first such target to be designed with Computational Fluid Dynamics (CFD). The QWeak target achieved all its design goals with a measured ℓH_2 density reduction of 0.8% and ℓH_2 density fluctuation of less than 50 ppm at 960 Hz. CFD-driven target design has been validated as the critical tool in the performance of the QWeak target. Currently the QWeak target is the highest power ℓH_2 target in the world and with the smallest noise figure. The P2 target will be 50% more powerful while being required to have five times less noise from ℓH_2 density fluctuation than the QWeak target. The design of the P2 target cryogenic loop components will be modelled after the successful targets for the QWeak and G0 experiments that ran at the Jefferson Lab. In addition, the performance of each component of the P2 target will be assessed with CFD.

Cooling requirement. The total heat load on the target is 4 kW, see Tab. 10 for a list of contributions to the target power load. Therefore, the target will require at least 4 kW of helium cooling from the MESA refrigerator in order to support 150 μA electron beam operations on target. The flow of He cooling needed can be calculated with the formula $\dot{m} = P/\Delta H$, where P is the total cooling power and ΔH is the He enthalpy variation between the inlet and the outlet of the HX. If the He inlet to the HX were at 10 atm, 14 K and the outlet were at 3 atm, 20 K, then 101 g/s He flow would be needed to provide 4 kW of cooling power. The same amount of cooling power could be provided by 40 g/s He delivered to the P2 HX at 3 atm, 4.5 K and returned from the HX at 1.5 atm, 20 K.

Heat exchanger. The heat exchanger will be used to liquefy the hydrogen gas and then provide enough cooling power to remove the total heat load from the target loop in order to keep the target stable. It will be modelled after the QWeak counter-flow HX, however, it will only require two layers of copper finned tube. The two layers will be wrapped around a central baffle to provide maximum heat transfer. At the midpoint of the heat exchanger the two layers of tubing will swap to equalize the pressure loss in each layer, see Fig. 20(a). The HX design will be assessed with CFD. The HX will be cold shocked and tested for leaks with a sensitive He leak detector under both vacuum and pressure in both the H_2 and He circuits.

High power heater. To mitigate the ℓH_2 density variations and relaxation time with electron beam trips the P2 target will be operated in constant heat load. In this mode

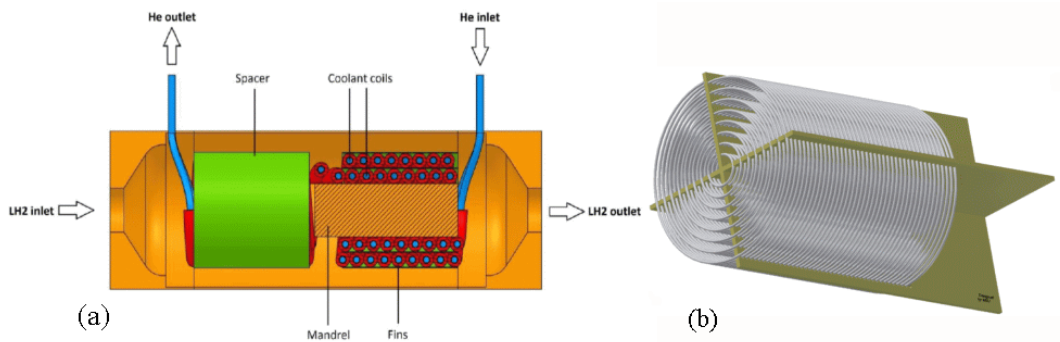
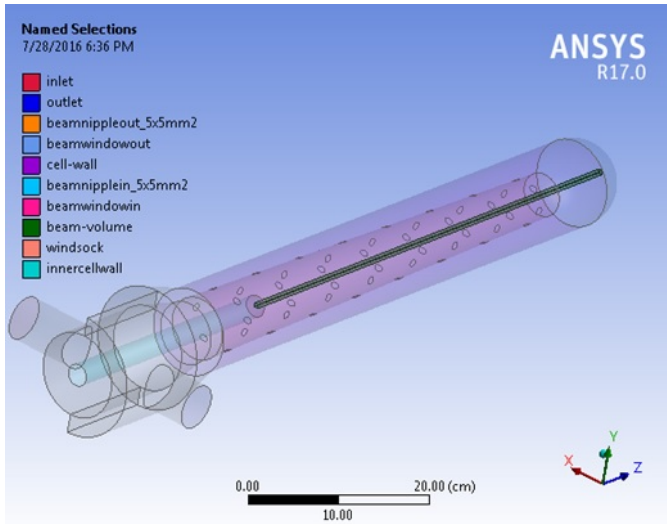
of operation the HPH power supply works in a feedback loop with the read-back of a temperature sensor embedded into the target fluid to keep the fluid temperature constant regardless of the presence of the electron beam. The heater is used to replace the beam heat load and regulate the loop temperature. The heater is designed to have eight layers of 18 Awg Nichrome wire wrapped around crossed G10 boards. The heater will reside in a section of loop pipe with conflat flanges. Heat transfer calculations were done assuming one can treat the heater as an array of cylinders or tubes in a flow. This assumption was largely confirmed for the QWeak heater by comparing the heat transfer calculations with CFD simulations. One major difference between this heater design and the QWeak design is that we plan to use a power supply with higher DC voltage and, of course, the heat load will be 50% more than the value used for QWeak, hence $P = 4000\text{ W}$. Therefore, the design calls for a greater than 4 kW, 250 V DC power supply which has a maximum current of 20 A. The ideal resistive load for this power supplies is 12.5 Ω , which provides a design constraint for the heater. A design of the HPH coils is shown in Fig. 20(b).

ℓH_2 pump. Comparing the P2 target design parameters with the QWeak target design parameters, it is expected that a centrifugal pump will be required for the P2 target. The QWeak ℓH_2 pump was designed in-house at Jefferson Lab for a volume displacement of 161/s at a rotational motor shaft frequency of 30 Hz. The QWeak ℓH_2 pump head was estimated with engineering calculations and corroborated with CFD simulations to be 0.077 bar. During commissioning of the QWeak target pump with ℓH_2 the pump head was measured to be (0.076 ± 0.007) bar at a rotational frequency of 30 Hz. The QWeak ℓH_2 pump achieved its design goals validating the engineering calculations and CFD simulations. Before ℓH_2 operations the QWeak pump underwent a series of tests at Jefferson Lab fully immersed in a liquid nitrogen (ℓN_2) bath. ℓN_2 is not expensive, is not flammable and its density is eleven times higher than ℓH_2 which makes it very useful in testing the performance of a cryogenic pump. The ℓN_2 tests resulted in several improvements to the pump system: optimized spacing on the motor shaft to accommodate the thermal contraction of various pump parts in cryogenic conditions without compromising performance, adequate bearings for cryogenic conditions and optimized pump controls. The P2 ℓH_2 pump will be designed to have less than 2 kg/s ℓH_2 mass flow or a volume rate of less than 281/s with a pump head of less than 0.1 bar, which is 36% higher than the QWeak ℓH_2 pump head. The impeller shape can be characterized using the specific speed ($N_s = N\sqrt{Q}/H^{0.75}$ where N is the rotational frequency, Q is the flow rate and H is the total head in the loop). Since the viscous heating is proportional to the 1.5th power of the pump head, the target loop geometry will need to be optimized while also trying to minimize the inventory of ℓH_2 in the target. Depending on the final geometry of the loop, it may be possible to have the pump motor outside the loop, hence reducing the overall heat load and mitigating the risk as-

Table 11. Parity-violation electron scattering ℓH_2 target parameters

| Experiment | Length <i>cm</i> | $P/I/E$ $W/\mu A/GeV$ | $\Delta\rho/\rho$ % | $\delta\rho/\rho$ ppm |
|------------|---------------------|--------------------------|------------------------|--------------------------|
| SAMPLE | 40 | 700/40/0.2 | 1 | < 1000 @ 60 Hz |
| HAPPEX | 20 | 500/35-55/3 | - | 100 @ 30 Hz |
| PV-A4 | 10 | 250/20/0.854 | 0.1 | 392 @ 50 Hz |
| E158 | 150 | 700/12/48 | 1.5 | < 65 @ 120 Hz |
| G0 | 20 | 500/40-60/3 | < 1.5 | < 238 @ 30 Hz |
| QWeak | 35 | 2500/180/1.1 | < 1.6 | < 50 @ 960 Hz |
| P2 | 60 | 4000/150/0.155 | < 2 | 10 @ 1000 Hz |
| MOLLER | 150 | 4500/75/11 | < 2 | 25 @ 1920 Hz |

P : beam power on target, I : maximum beam current, E : beam energy, $\Delta\rho/\rho$: target bulk density reduction, $\delta\rho/\rho$: size of target density fluctuation at given helicity reversal frequency.


Fig. 20. (a) CAD drawing of the P2 HX. (b) CAD drawing of the 8 layer P2 HPH

Fig. 21. G0 type cell design.

sociated with servicing the motor. The P2 pump will be assessed in ℓN_2 to optimize it. The pump housing will be pressure tested and leak checked.

ℓH_2 cell. To accommodate the experimental acceptance for scattered particles the target cell design will start with a G0-type cell geometry, shown in Fig. 21. The cell in this

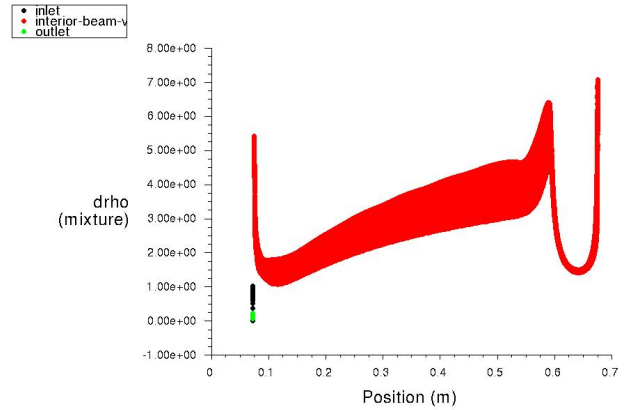

Fig. 22. Preliminary CFD simulations of the ℓH_2 density loss. The vertical axis is the absolute relative ℓH_2 density loss in (%) and the horizontal axis is the distance along the beam path from the beam entrance window of the cell to the downstream beam exit window.

figure is 10 cm in diameter with a hemispherical window at the downstream end. The cell has an internal conical flow diverter made of 0.075 mm thick aluminum foil with holes on its wall. The internal flow diverter, also called windsock, will be e-beam welded on a baffle that will sep-

arate the inlet ℓH_2 flow into the cell from the outlet flow. The 60 cm ℓH_2 length in beam will be defined between an upstream thin aluminum window and the downstream aluminum hemispherical cell window. The upstream aluminum window will be a vacuum window with a diameter of 12 mm and thickness of 0.125 mm. This window will be supported at the end of an aluminum tube manufactured on an aluminum conflat flange that will mate on the target manifold. This configuration keeps the asymmetric cell manifold completely outside of the experimental acceptance. The cell connects with the rest of the cryogenic loop through its manifold. The target cell and manifold will be made from an aluminum alloy. The cell will be manufactured on a conflat flange that will mate with the aluminum manifold. Preliminary structural engineering calculations show that a cell wall thickness of 0.25 mm will be sufficient to self support such a long cell. ℓH_2 enters the cell through the inner flow diverter and is accelerated and jetted at the aluminum beam exit window where it turns around and flows upstream in the annular space between the cell wall and the flow diverter wall towards the cell manifold, which directs it back into the target loop.

Figure 22 shows the ℓH_2 density loss from CFD simulations of the cell geometry in Fig. 21 [90]. The CFD simulations were done in steady state assuming the design parameters from Tab. 9 and the electron beam heating into ℓH_2 and aluminum windows from Tab. 10. These CFD simulations cover a temperature range of 20 K to 300 K for the heated fluid and the cell walls, properly accounting for ℓH_2 boiling and treating the fluid as a liquid-gas mixture wherever it undergoes phase change in the geometry. Turbulence is accounted for in these simulations through a model. The vertical spread at a specific location along the beam path shows the absolute relative ℓH_2 density loss in the square beam spot area of 25 mm². If the ℓH_2 density decreases by 6.7% the liquid reaches saturation at 23.7 K and is susceptible of boiling. The average ℓH_2 density loss over the beam volume for this model is predicted with CFD to be 3%. The QWeak target was the first PVES ℓH_2 target designed with CFD. The QWeak target group originally proposed using a G0-type cell, extended to 35 cm long, CFD modelling changed that design from a fully longitudinal flow to a fully transverse ℓH_2 flow to the beam path. Computational fluid dynamics technologies will be used to drive the design of the P2 target cell, starting from a G0-type cell, extended to 60 cm length aiming for a luminosity loss due to the target boiling of less than 2%. The thin-walled aluminum cells are structurally the weakest part of the cryogenic target loop. A safety testing protocol will be developed to verify that the ℓH_2 cells are safe for operations (pressure tests, leak checks etc.).

Density fluctuations. The parity-violation asymmetry will be measured experimentally by using quartet helicity-flip structures $+- -+$ and $-+ +-$. The time period of an asymmetry quartet is 4 ms. The quartet asymmetry is defined as $A_m = (N_+ - N_-)/(N_+ + N_-)$, where N_+ and N_- are the total number of scattered electrons, normalized to

the electron beam, in the two positive and the two negative helicity states in the quartet respectively. In the absence of other noise sources, A_m has a width, the counting statistics [89], given by $\sigma_0 = (N_+ + N_-)^{-0.5} = (f/4R)^{0.5}$, where f is the electron helicity frequency and R is the expected electron rate in the P2 main detector. The P2 counting statistics is estimated to be 50 ppm, four times smaller than QWeak's. The ℓH_2 target density fluctuation noise on the time period of the electron helicity is called boiling noise and adds in quadrature to the counting statistics to yield the measured asymmetry width $\sigma_m^2 = \sigma_0^2 + \sigma_b^2$. If the P2 target boiling noise contribution to the measured asymmetry width σ_m is capped at 2%, then $\sigma_b < 10$ ppm or five times smaller than the QWeak target boiling noise and twice smaller than the projected MOLLER ℓH_2 target boiling noise at Jefferson Lab. This design parameter makes the P2 target the most challenging PV ℓH_2 target in the world today. The QWeak ℓH_2 target underwent a thorough assessment of its performance in beam. The QWeak target noise was also measured at various electron beam helicity frequencies and found to vary like $\sigma_b \propto f^{-0.38}$. CFD simulations can reliably predict the ℓH_2 density reduction. A Facility for Computational Fluid Dynamics (CFDFAC) is being used to develop state of the art time-dependent simulations that aim to capture a ℓH_2 target cell's noise over various time scales. These simulations will be critical in the design of the MOLLER target cell [51]. The P2 target cell design will benefit from these design technologies. A fine tuning of the CFD P2 target cell design along with fine tuning of operational parameters like beam current, beam spot size, ℓH_2 pump frequency, ℓH_2 temperature and helicity frequency will achieve the design noise figure of the target of 10 ppm.

Solid targets. The solid target ladder will be attached to the hydrogen cell and will contain thick aluminum alloy foils (the same alloy as the cell) at the same positions along the beam axis as the cell windows. In addition, it will contain centering targets for beam steering/alignment and several carbon targets for optics studies. CFD will be used to assess the beam heating of these targets and establish beam current limits for safe operations.

Controls. Target controls include instrumentation, hardware and software to monitor, operate and control the target system. The target loop will be instrumented with electrical feed-throughs for temperature sensors, ℓH_2 pump motor and HPH. We plan to place temperature sensors at six locations around the loop, with two sensors at each location for redundancy, across the target cell manifold, across the HPH and across the HX. We also plan to place temperature sensors in the He circuit of the HX at inlet and outlet to the HX. All temperature sensors will be immersed in the fluid and calibrated. The locations of the sensors will allow us to measure the ℓH_2 pump performance, the HX cooling power and efficiency and measure and monitor the beam heating power. Redundancy of the sensors will mitigate the risk that some of them

will die in radiation. The solid targets ladder will be instrumented with up to six resistance temperature detectors (RTDs). The target electronics will be made rack mountable. These will include the temperature sensors monitors/controllers, the pump motor controller, the HPH power supplies (two identical supplies connected in parallel, one active, one redundant), vacuum gauge controllers, pressure monitors/transmitters, ADCs, DAQ cards, low level data acquisition computer or PLC. MESA plans to use EPICS as a software environment. The underlying software to monitor, control, operate and archive target parameters data will be written in EPICS. As appropriate other software, Python, C++ etc. will be used to control and monitor target parts.

Safety. The G0 target contained 6 liters of liquid hydrogen and ran safely for over five years at Jefferson Lab. The QWeak target contained 55 liters of liquid hydrogen and ran safely over two years at the same lab. The safety experience accumulated by previous PVES liquid hydrogen targets will be leveraged in the design, manufacturing and operations of the P2 target.

5 The P2 Spectrometer

The P2 spectrometer will use a large superconducting solenoid and is designed to perform different tasks. The first one is the detection of the elastically scattered electrons. Fast and radiation-resistant detectors are needed for this. Second, background processes such as Moller scattering and bremsstrahlung has to be suppressed. Here, a careful design of the detector layout performing Geant4 simulations is performed. Third, a measurement of the momentum transfer Q^2 has to be provided. A dedicated detector system for track reconstruction in the magnetic field is developed for this task. All these aspects are discussed in the following sections.

5.1 Monte Carlo simulations

In order to simulate the P2 experiment, a Geant4 [91,92,93] application has been developed. Geant4 is a software framework that allows to simulate the passage of particles through matter with a computer. The simulation of the physics processes involved is based on Monte Carlo methods, where the differential cross sections are interpreted as probability density distributions, which are used to sample the relevant kinematic variables of the particles.

The purpose of the experiment's simulation is to ensure the feasibility of the $Q_W(p)$ measurement with the foreseen apparatus. In this section, the main aspects of the Geant4 application will be discussed and results presented.

5.1.1 Geometry definition

The application employs an interface to Computer-Aided Design (CAD) software for defining the geometrical objects the experimental apparatus is comprised of. CAD software is a widely used designing and analyzing tool in engineering science. The simulation of the P2 experiment uses CADMesh [94] to import geometrical objects created with CAD software into Geant4. For this purpose, the surfaces of the objects under consideration are first parametrized by applying a tessellation procedure and then converted into a Geant4-native geometrical object. The big advantage of this procedure is that engineering studies can be performed using CAD applications and the resulting geometrical shapes may be directly imported into Geant4. Furthermore, implementing new and altering existing parts of the apparatus using realistic, complex geometrical shapes is possible with a minimum of programming effort this way. The downside of using CADMesh as compared to Geant4's standard method of defining geometry directly in the source code is that the runtime of the application is slightly increased due to the higher number of surfaces resulting from the tessellation procedure. However, the prolongation of runtime is a minor effect and easily outweighed by the benefits of the CAD interface, especially when using multiple CPU cores in parallel to perform the simulation.

Figure 23 shows a CAD drawing of the experimental setup, which has been implemented in the simulation using CADMesh. The beam electrons enter the scattering chamber's vacuum through the final part of the beamline and interact with the ℓH_2 target. Both target and scattering chamber are contained within a superconducting solenoid that generates a magnetic field of $B_z \approx 0.6\text{ T}$ along the beam axis. The beam electrons, which have been scattered off protons in the target, pass a Kevlar window which separates the vacuum of the scattering chamber from the helium filled chamber that contains the tracking detectors. The tracking detectors will be used to reconstruct the Q^2 of the detected electrons and are described in section 5.5. After passing the tracking system, the electrons are detected in a Cherenkov ring detector for the measurement of the parity-violating asymmetry.

5.1.2 Event generation

One of the simulation's central aspects is the realistic simulation of the interaction between the electron beam and the 600 mm long ℓH_2 target. Since the beam energy $E_{\text{beam}} = 155\text{ MeV}$ is rather small, energy loss and angular straggling of the beam in the target material due to collisions and bremsstrahlung cannot be neglected. While Geant4 is an excellent tool to simulate these processes, the simulation of elastic electron-proton scattering under large scattering angles is not foreseen in a manner that is coherent with the simulation of the energy loss processes. The reason for this is that the probability for scattering an electron elastically off a proton with $\theta_f \sim 35^\circ$ is in

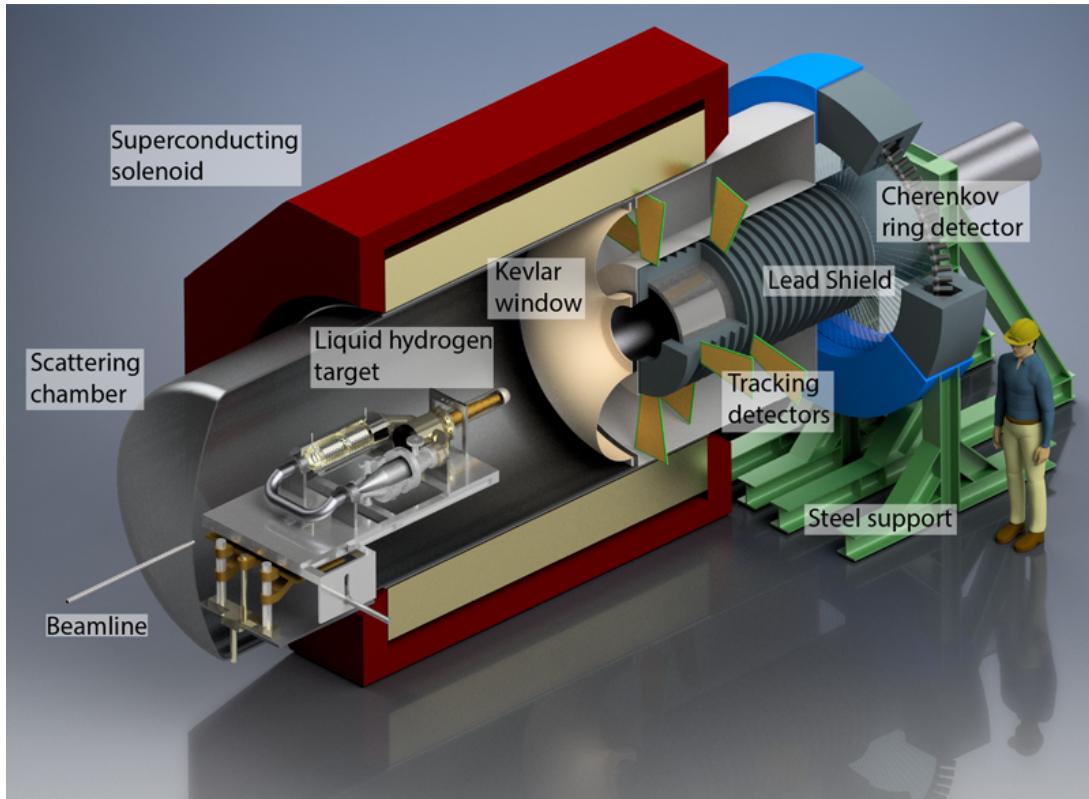


Fig. 23. CAD drawing of the experimental setup which has been implemented in the Geant4 simulation using CADMesh.

the order $\mathcal{O}(10^{-4})$ and therefore too low to simulate the process with its actual probability in an efficient way.

In order to enable an efficient simulation of the ep scattering process, a dedicated event generator has been developed. Initially, the passage of the beam electrons through the target volume is simulated by impinging electrons with $E_{\text{beam}} = 155 \text{ MeV}$ upon the target volume. The beam electrons are tracked inside the ℓH_2 volume, while the soft energy loss processes are simulated using Geant4 built-in process models. As the beam electrons travel through the target volume, initial states of the elastic ep scattering process are scanned at random positions along their trajectories without interfering with the simulation of the other physics processes. Figure 24 illustrates the principle. An initial state of elastic electron-proton scattering is defined by:

- The position of the vertex inside the target volume;
- The initial state energy E_i of the beam electron;
- The 3-momentum vector of the beam electron.

This method of sampling an ensemble of initial states of the ep scattering process is valid, because the beam electrons undergo very similar processes as they travel through the target volume so that each of the beam electrons' trajectories may be regarded as the mean of an ensemble of similar trajectories. This mean trajectory can be used to scan several initial states of elastic ep scattering. Figure 25 shows a sample distribution of initial states of the ep scattering process. As the beam electrons are propagated through the ℓH_2 volume, Geant4 gener-

ates secondary particles in the course of the simulation of the collision and bremsstrahlung processes. All of these particles are tracked through the target volume as well until they leave the volume. Once at this point, the particles' state is scanned, saved, and the particle is stopped and terminated in order to save CPU time. This leads to an ensemble of particle states stemming from background processes in the target volume, which are located on the target volume's surface. Such a state is defined by:

- The particle's type;
- The position of the particle on the target's surface;
- The 4-momentum vector of the particle.

Once calculated for a specific target geometry, both the initial state ensemble of the ep scattering process and the ensemble of background particle states may be re-used an arbitrary number of times to generate final state ensembles for the detector simulation. In order to be able to predict event rate distributions expected in the real experiment with the method described above, one has to normalize the simulated events properly.

For each of the initial states of elastic ep scattering, one final state is generated. For this purpose, a final state generator has been developed. The generator uses elastic kinematics and creates an electron and a proton in the final state of the scattering process. For this, the electron's scattering angles θ_f and ϕ_f are sampled using flat probability density distributions. The Rosenbluth formula (Eq. (20)) is used as a weighting factor for the sampled event. Figure 26 shows a comparison between the rate

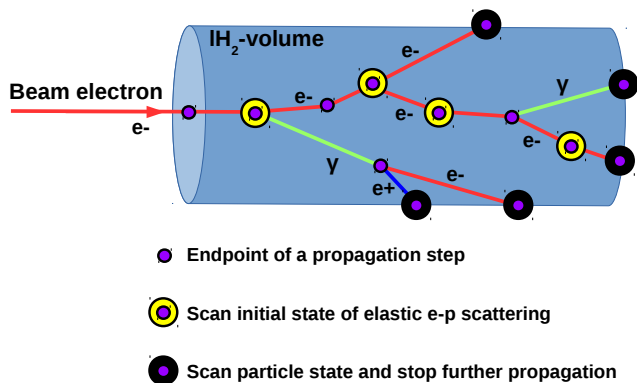


Fig. 24. Principle of generating ensembles of initial states of elastic e-p scattering and background particle states. The beam electrons are impinged upon the ℓH_2 -volume. In Geant4, all particles are propagated in spatial steps of finite length. The soft energy loss processes are simulated using the process models implemented in Geant4. Initial states of elastic e-p scattering are scanned at random positions along the beam electrons' trajectories without interfering with the simulation of the other physics processes. When a particle reaches the surface of the ℓH_2 -volume from its inside, the particle's state is scanned and the simulation of the particle's trajectory is terminated.

prediction of the event generator and one that is based on a numerical integration of the differential cross section. The event generator reproduces the rate prediction of the independent numerical integration to high accuracy. Furthermore, a prototype of a final state generator has been developed, which allows for a real photon in the final state of the scattering process. This final state generator will be

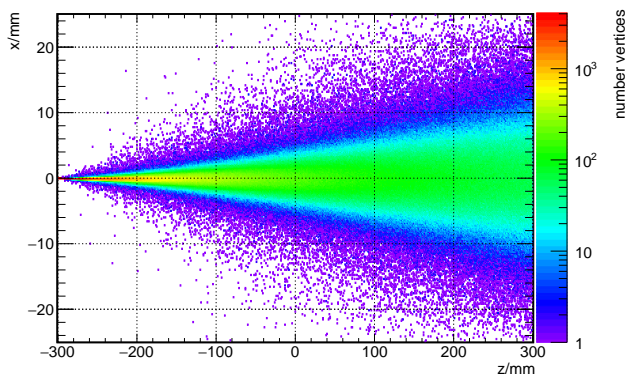


Fig. 25. Projection of the spatial distribution of sampled interaction vertices for the simulation of elastic electron-proton scattering to the x - z -plane. The cylindrical ℓH_2 volume stretches from $z = -300$ mm to $z = 300$ mm and has a radius of 25 mm. The electron beam enters the target volume from the left. One recognizes the widening of the beam profile due to collision processes with increasing z -coordinate.

available in addition to the currently used generator in the near future and make it possible to take the shifts in Q^2 into account, which are caused by the radiation of photons (see section 6.2).

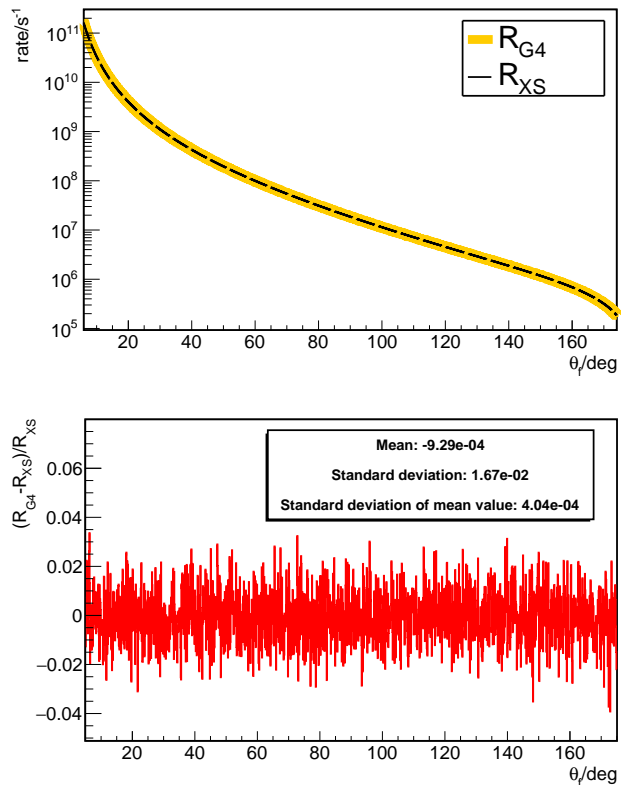


Fig. 26. Comparison of two predictions of the scattering rates expected in the P2 experiment at design luminosity. R_{G4} is the prediction made using the event generator implemented in the Geant4 simulation, and R_{XS} is the rate prediction based on a numerical integration of the Rosenbluth formula. The upper picture shows the dependence of R_{G4} (yellow thick line) and R_{XS} (thin black dashed line) on θ_f . The two curves shown in the upper picture do overlap each other. The lower picture shows the relative deviations between the two rates as a function of θ_f . The relative deviations scatter statistically around 0 for the considered values of $\theta_f \in [5^\circ, 175^\circ]$, which indicates that the event generator reproduces the expected rate distribution in θ_f correctly.

The states of the beam electrons and background particles that have been scanned during the passage of the beam electrons through the target volume are simply recreated after the simulation of elastic ep scattering has been completed. After their creation in the target volume, all particles' trajectories in the magnetic field of the superconducting solenoid are simulated.

5.1.3 Simulation of trajectories in the magnetic field

In order to be able to properly determine the positions of the tracking system, the Cherenkov ring detector and the

lead shielding, a realistic simulation of charged particles' trajectories in the magnetic field of the superconducting solenoid is indispensable. For this reason, the simulation enables the usage of realistic magnetic field maps to calculate the trajectories. In particular, the P2 Collaboration has studied the usability of the superconducting solenoid that has been used in the FOPI [95] experiment. The field-map of this magnet has been provided to the P2 Collaboration courtesy of the FOPI Collaboration. It is shown in Fig. 27.

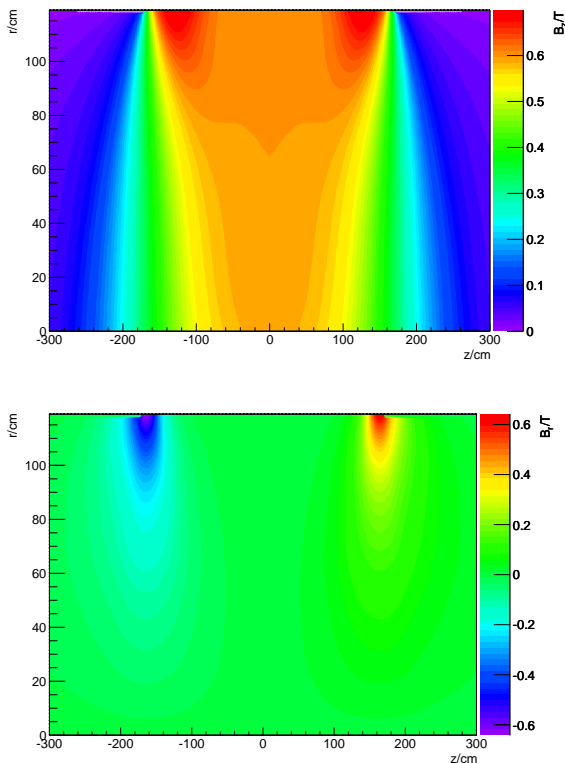


Fig. 27. Magnetic field-map of the FOPI-solenoid. Courtesy of Y. Leiffels (FOPI Collaboration). The upper picture shows the z -component B_z of the magnetic field, which is parallel to the beam axis, as a function of the z -coordinate and the distance r from the beam axis. The lower picture shows the radial component B_r of the magnetic field, which is perpendicular to the beam axis, as a function of z and r .

For the calculation of charged particles' trajectories in the magnetic field, an implicit Euler method is used to numerically solve the equations of motion. This method makes use of the fact that in a time-independent magnetic field, which is locally homogeneous, the trajectories may be regarded as a concatenation of helix-shaped chords.

Figure 28 shows projections of simulated electron trajectories in the magnetic field of the FOPI solenoid. For this specific calculation, all physics processes implemented in Geant4 have been disabled so that there is no angular straggling or energy loss of the particles as they travel through the materials of the apparatus. To illustrate the

effect of the lead shielding, all particles which hit the shields were stopped instantly. The picture illustrates the purpose of the magnetic field, which is to separate electrons in the final state of the elastic ep scattering process from electrons in the final state of the Møller scattering process. The function of the lead shielding is also illustrated: It covers the lines of sight between the Cherenkov detector and the target volume in order to prevent photons emerging from the target from hitting the detector's active volume and photomultiplier tubes.

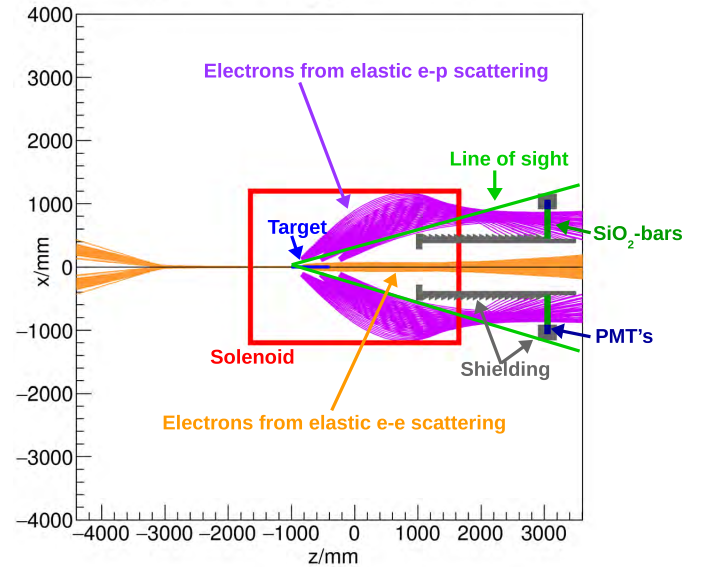


Fig. 28. Simulation of electron trajectories in the magnetic field of the FOPI solenoid. Shown are the projections to the x - z -plane of the trajectories of electrons in the final states of elastic ep scattering (purple), which are to be detected in the P2 experiment, and electrons in the final state of the Møller scattering process (orange) for $E_{\text{beam}} = 155$ MeV.

5.1.4 Simulation of the Cherenkov ring detector

The simulation of the Cherenkov detector is another central aspect of the Geant4 application. A detailed description of the Cherenkov ring detector can be found in section 5.2. The main goal of the Monte Carlo simulation is to predict the distribution of particles which hit the detector as well as the detector response.

The calculation of the particle distribution that is incident upon the detector's active volume, which will consist of SiO_2 bars wrapped in a reflective foil (see Fig. 34), is done by scanning the particles' states when they reach the surface of a SiO_2 bar in the simulation. The information gathered includes

- the particle's type,
- the impact position of the particle on the active volume's surface,
- and the momentum 4-vector of the particle at impact position

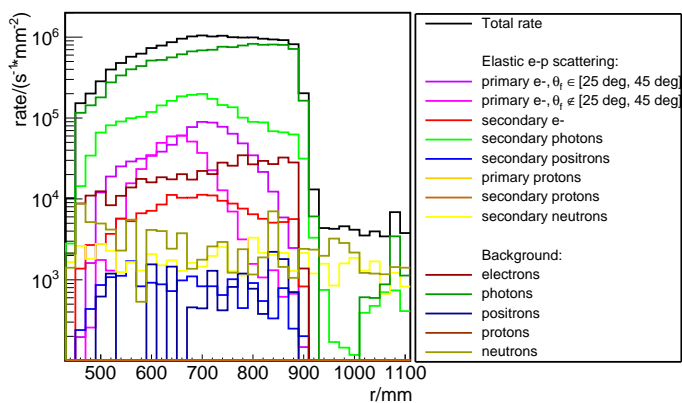


Fig. 29. Rate distributions on the surface of the Cherenkov ring detector as a function of the distance r from the beam axis. The rates have been calculated assuming the experimental conditions listed in Tab. 1 and Tab. 2 of Sect. 2. The rates have been normalized to the areas of the ring segments which correspond to the width of the histograms’ bins in r -direction. Further explanations and the discussion of the distributions can be found in the text.

for all particles. Figure 29 shows the simulated rate distribution on the surface of the ring detector for the particle types considered in the calculation. In the figure legend, the particle types are sorted into two categories according to the way the event generator operates (see section 5.1.2): The first category comprises particles which reach the detector as a consequence of an elastic ep scattering in the ℓH_2 target, the second category includes all particles which hit the detector as a consequence of a background process in the target volume. For the first category, a distinction is made between “primary” and “secondary” particles. A “primary” particle is a particle that has been generated by the final state generator, so it can be either an electron or a proton in the final state of the ep scattering process. All particles labeled “secondary” have emerged from the interaction of primary particles with the materials of the experimental setup. The total rate distribution in Fig. 29 is dominated by photons stemming from background processes in the target volume and secondary photons created during the simulation of elastic ep scattering. As described in 5.2, the SiO_2 bars reach from $r = 450$ mm to $r = 1100$ mm, but only the parts with $r \in [450 \text{ mm}, 900 \text{ mm}]$ serve as active volumes for particle detection. The sections with $r > 900$ mm guide the Cherenkov light to the photomultiplier tubes, which will be located at $r > 1100$ mm. The parts used as light-guides will be surrounded by a 100 mm thick lead shield, which is the reason for the reduction of the total rate in the region with $r \geq 900$ mm. Table 12 lists the total rates expected in the P2 experiment on the surface of the full SiO_2 ring.

It is obvious from Fig. 29 that a good understanding of the Cherenkov detector’s response to the incident particles is needed, since the photon rate is much higher than the rate of the primary electrons from elastic ep scattering. In order to be able to predict the response of the detector, one needs to know the number of photo-electrons emitted

| Contribution | Hit rate/ s^{-1} |
|---|-----------------------|
| Total | 1.54×10^{12} |
| Elastic ep scattering in the target: | |
| Primary electrons, $\theta_f \in [25^\circ, 45^\circ]$ | 7.10×10^{10} |
| Primary electrons, $\theta_f \notin [25^\circ, 45^\circ]$ | 3.21×10^{10} |
| Primary protons | 0.00 |
| Secondary electrons | 1.33×10^{10} |
| Secondary positrons | 1.47×10^9 |
| Secondary photons | 2.12×10^{11} |
| Secondary protons | 5.11×10^5 |
| Secondary neutrons | 5.41×10^9 |
| Background processes in the target: | |
| Electrons | 4.05×10^{10} |
| Photons | 1.14×10^{12} |
| Positrons | 1.40×10^9 |
| Protons | 0.00 |
| Neutrons | 8.31×10^9 |

Table 12. Survey of the hit rates expected on the full SiO_2 ring of the Cherenkov detector for the projected experimental conditions.

from the photomultiplier’s cathode in consequence of a particle hitting the detector. Since the reproduction of the Cherenkov effect in the simulation of the full experiment is not feasible due to the CPU time required for a coherent simulation of the effect, a parametrization of the detector modules’ response has been created. The parametrization is described in detail in Sect. 5.2. It allows to calculate the mean number of photo-electrons expected from a particle passing through a SiO_2 bar based on:

- The particle’s type;
- The particle’s total energy;
- The particle’s momentum direction at impact position on the detector module.

Utilizing the detector response parametrization allows to convert the hit rate distributions shown in Fig. 29 into the photo-electron rate distributions shown in Fig. 30. Here, the photo-electron rates emitted from the photocathodes are shown as functions of the radius r at which the particles have hit the detector. The total photo-electron rate is clearly dominated by the contributions stemming from electrons, which have been scattered elastically off protons in the target volume. The parametrization of the detector response currently includes only electrons, positrons and photons. All other particle types’ contributions to the spectrum have been set to 0 manually. The expected photo-electron rates are listed in Tab. 13.

By comparing the spectra shown in Fig. 29 and Fig. 30, one observes that the relative contribution of photons to the total photo-electron rate is drastically reduced com-

| Contribution | Photo electron rate/ s^{-1} |
|---|--------------------------------|
| Total | 9.06×10^{12} |
| Elastic ep scattering in the target: | |
| Primary electrons, $\theta_f \in [25^\circ, 45^\circ]$ | 5.12×10^{12} (56.5 %) |
| Primary electrons, $\theta_f \notin [25^\circ, 45^\circ]$ | 3.11×10^{12} (34.3 %) |
| Secondary electrons | 3.07×10^{11} (3.4 %) |
| Secondary positrons | 6.17×10^{10} (0.7 %) |
| Secondary photons | 1.63×10^{11} (1.8 %) |
| Background processes in the target: | |
| Electrons | 2.54×10^{11} (2.8 %) |
| Photons | 3.48×10^{10} (0.4 %) |
| Positrons | 7.97×10^9 (0.1 %) |

Table 13. Survey of the photo-electron rates expected in the Cherenkov ring detector for the projected experimental conditions.

pared to the photons' relative contribution to the total hit rate distribution. The explanation for this is that many photons do not lead to a detector signal, because they cannot produce Cherenkov light inside the SiO_2 bars directly. The photons have to interact with the detector material first leading to charged particles with mass m travelling through the SiO_2 bars, whose energies are above the threshold energy

$$E_{\text{th}} = \frac{m}{\sqrt{1 - (1/n^2)}} \quad (59)$$

for the production of Cherenkov light. In Eq. (59), n is the refractive index. For electrons traveling through SiO_2 , it is $E_{\text{th}} \approx 0.7 \text{ MeV}$. Most of the photons which hit the detector have energies smaller than E_{th} , as can be seen

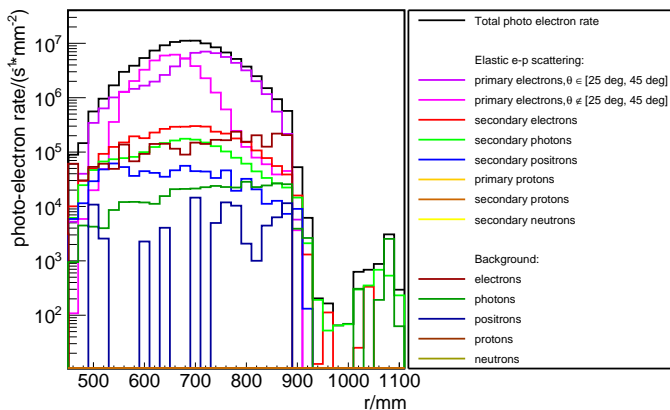


Fig. 30. Photo-electron rate distributions as a function of the distance r from the beam axis at which the particles hit the surface of the SiO_2 ring. Like the distributions shown in Fig. 29, the photo-electron distributions are normalized to the areas of the ring segments associated with the bin widths of the histograms. Further discussion in the text.

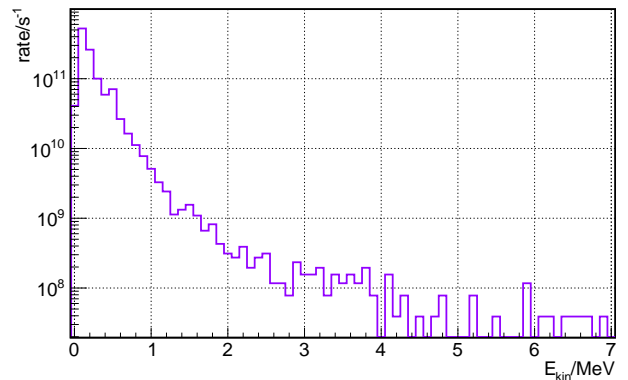


Fig. 31. Energy distribution of the photons stemming from background processes in the target. The majority of the photons have energies below $E_{\text{th}} \approx 0.7 \text{ MeV}$.

in Fig. 31. This circumstance enhances the suppression of photons in the Cherenkov ring detector.

Figure 32 shows the photo-electron rate distribution of all particles hitting the detector in consequence of an elastic ep scattering in the target volume in dependence of the distance r from the beam axis and the Q^2 value of the scattering event. From this distribution the average value of Q^2 can be calculated:

$$\langle Q^2 \rangle_{\text{Cherenkov}} = 4.57 \times 10^{-3} (\text{GeV}/c)^2. \quad (60)$$

This corresponds to

$$\langle A^{\text{exp}} \rangle_{\text{Cherenkov}} = -28.77 \text{ ppb} \quad (61)$$

for the asymmetry, which is to be measured. The reduction of the absolute value of the asymmetry by 28 % compared to the value of -39.94 ppb , which has been predicted by the error propagation calculation in section 2.2.3 is due to the dilution of the asymmetry caused by the background and the admixture of electrons from elastic ep scattering with smaller values of Q^2 .

5.2 Integrating Cherenkov detectors

A high-precision, high-intensity electron scattering experiment such as P2 imposes substantial demands on the detector system. In order to reach the precision goal by measuring the tiny parity-violating asymmetry in electron-proton scattering of only $A^{\text{exp}} = 28.77 \text{ ppb}$, we need to collect very high statistics in a manageable run-time. The design of the detector was optimized with regard to speed, radiation hardness and optimal coverage of polar and azimuth angles as well as a strong signal from elastically scattered electrons and a suppression of background particles.

5.2.1 General detector concept

The P2 detector will detect high energy electrons via the Cherenkov effect. As shown in Fig. 33 it is going to consist

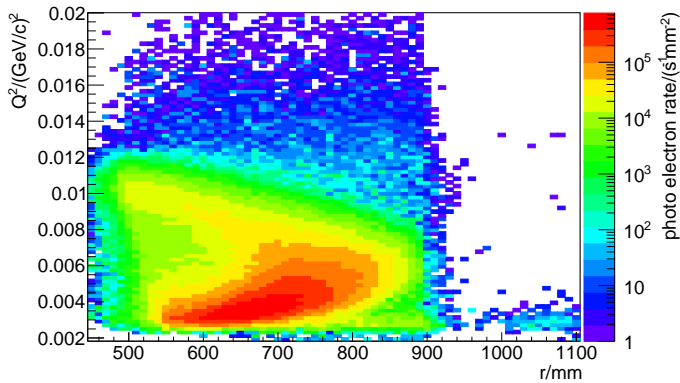


Fig. 32. Photo-electron rate distribution of all particles hitting the detector in consequence of an elastic ep scattering in the target volume.

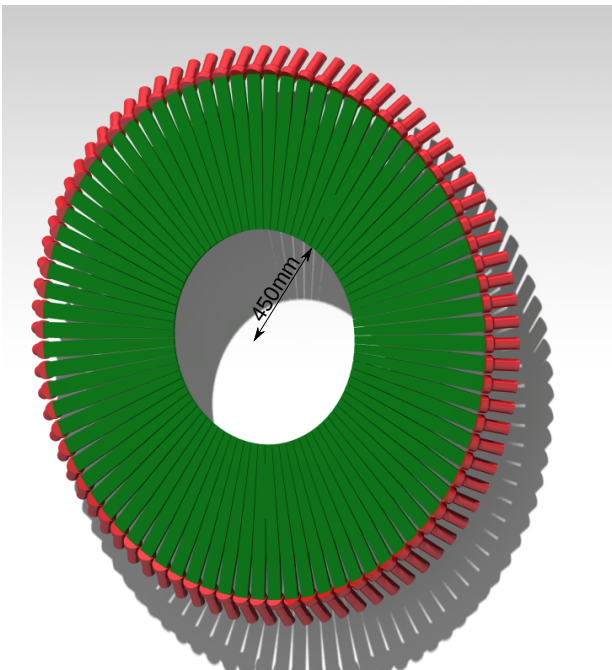


Fig. 33. Detector ring consisting of 82 fused silica bars.

of 82 wedged fused silica bars (also referred to as quartz bars) that will cover the whole azimuth angle aside from very small gaps between the single detector elements occupied by wrapping and mounting material. Each quartz bar is wrapped in Alanod 4300UP, a highly reflective aluminum foil, which is not anodized to avoid wave interference caused by a coating. A photomultiplier tube (PMT) is attached to each bar.

The active area of the bars will cover the radial range of 450 mm to 900 mm from the beam line. The quartz bars will have an additional 200 mm inactive part which will be shielded by 100 mm of lead and will serve as a light-guide for the Cherenkov light to the photomultipliers.

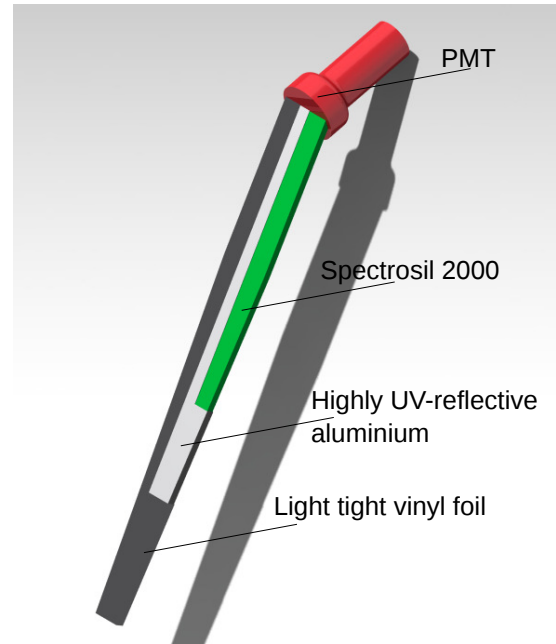


Fig. 34. Detector element consisting of quartz bar with optical outlet, PMT, UV reflective wrapping, and light-tight vinyl.

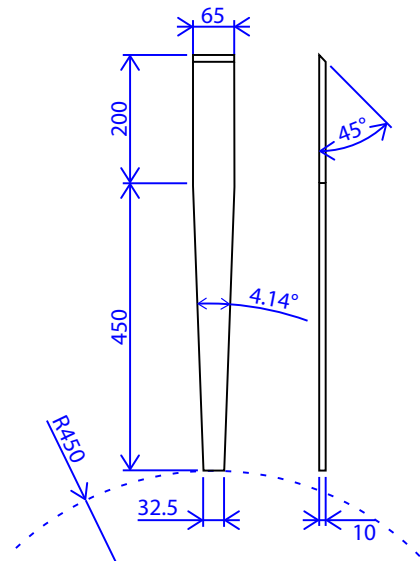


Fig. 35. Technical drawing of fused silica bars.

5.2.2 Requirements

The hit rates during the data taking runs onto the P2 detector are going to be in excess of 10^{12} Hz. They will be recorded in charge-integrating mode (see Sect. 5.3).

Operation in integrating mode precludes event mode cuts based on pulse shape, and true counting statistics is not achievable. Therefore the two primary concerns for the detector design are to reduce background sensitivity as much as possible and to increase the signal-to-excess noise ratio to a level that allows the detectors to operate as close to counting statistics as possible.

The asymmetry in the i_{th} helicity pair is

$$A_i = \frac{N_i^+ - N_i^-}{N_i^+ + N_i^-}. \quad (62)$$

Using simple error propagation and the approximation $N_i^+ = N_i^- = N_i$ this gives:

$$\sigma_{A_i} = \frac{1}{2N_i^2} \sqrt{2N_i^2 \sigma_N^2}. \quad (63)$$

If one assumed Poisson statistics ($\sigma_{N_{stat}} = \sqrt{N}$), the asymmetry error for a given detector in the i_{th} helicity pair would be

$$\sigma_{A_i} = \frac{1}{\sqrt{2N_i}}. \quad (64)$$

However, the production of showers inside the quartz, sub-optimal geometry, and poor light collection efficiency typically lead to excess noise (because they produce additional variation in photo-electron count), expressed by an additional term:

$$\sigma_{A_i} = \sqrt{1 + \alpha^2} / \sqrt{2N_i} \quad (65)$$

where $\alpha \equiv \sigma_{PE}/n_{PE}$, N_i is the number of primary electrons detected within a single helicity window, and n_{PE} and σ_{PE} are the mean photo-electron yield and standard deviation in the yield respectively. A higher average number of photo-electrons per event leads to a decrease in excess noise.

We demand that excess noise be less than 1%:

$$\sqrt{1 + \alpha^2} < 1.01. \quad (66)$$

Approximating the standard deviation to be $\sigma_{PE} = \sqrt{n_{PE}}$, we find that the number of photo-electrons per electron incidence onto the quartz bar, n_{PE} , needs to be larger than 50:

$$n_{PE} > 50. \quad (67)$$

These issues are intimately connected to the detector material and geometry, which has been optimized using simulations verified by experiment. The final choice for the geometry and orientation between the quartz pieces, the beam, and the PMTs is being studied using simulations and prototype tests at the MAMI electron beam, both of which are described in more detail in Sect. 5.2.4.

The amount and spectral distribution of Cherenkov photons, produced per 1 cm of trajectory in the radiator, are well described by the formula

$$\frac{dN}{d\lambda} = \frac{2\pi z^2 \alpha}{\lambda^2} \left(1 - \frac{1}{\beta^2 n(\lambda)^2} \right) \quad (68)$$

where z is the particle charge expressed in units of e , α is the fine structure constant, β the velocity as a fraction of the speed of light, and $n(\lambda)$ the wavelength-dependent refractive index of the material. Thus, a high energy electron generates a number of approximately 900 Cherenkov photons when travelling through a 1 cm piece of quartz. It is evident from the plot of this spectrum in Fig. 36 that a large portion of this light is in the deep UV region. Special

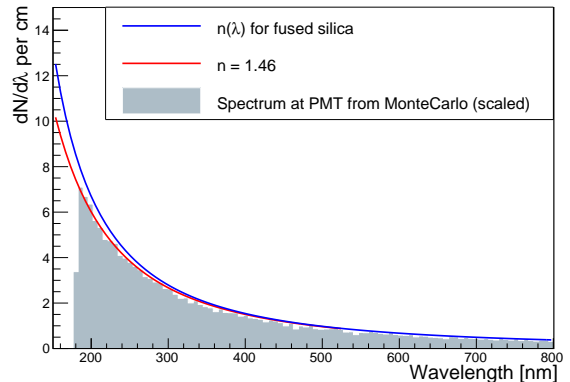


Fig. 36. Number of photons produced by the Cherenkov effect per 1 cm track length and nm wavelength in fused silica and photon spectrum detected at the location of the PMT in the Geant4 simulation (scaled for comparison purposes).

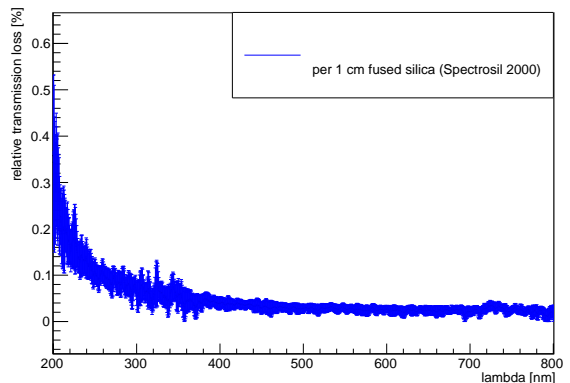


Fig. 37. Spectral transmission losses per 1 cm of fused silica.

care is taken to collect these photons in the PMT, where they will be transformed into an electric signal. The PMT will be located at the end of the quartz bar facing away from the beam axis. In order to minimize the light losses on the way to the PMT and maximize the number of electrons from the PMT cathode, all the material used for the detector elements has to be suitable for UV applications.

The fused silica bars are made of Heraeus Spectrosil 2000, a very pure form of amorphous silicon dioxide, which is extremely well transmissive to UV light. As shown in Fig. 37 the light intensity losses per 1 cm are very low even at 200 nm wavelength.

Figure 38 shows that for fused silica both the Cherenkov angle for ultra-relativistic charged particles with $\beta \approx 1$ and the critical angle of total internal reflection at the boundary to air are approximately 45° , the Cherenkov angle being slightly larger over the whole spectrum.

We chose the geometry of the quartz bars in such a way as to enhance the light collection by the effect of total internal reflection. It is ensured that Cherenkov light emerging from a perpendicular electron incidence is contained within the material and guided to the outer end, where

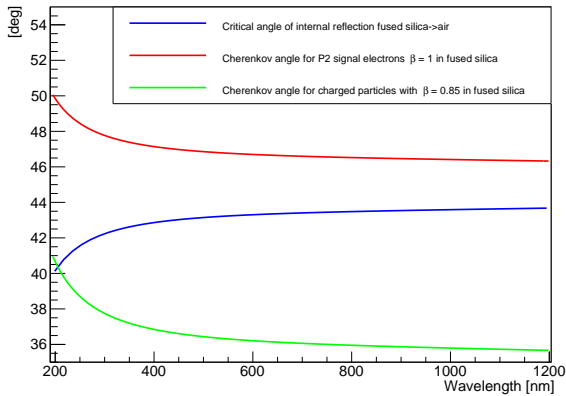


Fig. 38. Cherenkov angle and critical angle of total internal reflection as a function of the wavelength for fused silica.

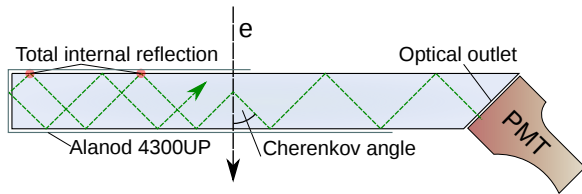


Fig. 39. Quartz as Cherenkov medium serves as an effective light-guide at the same time.

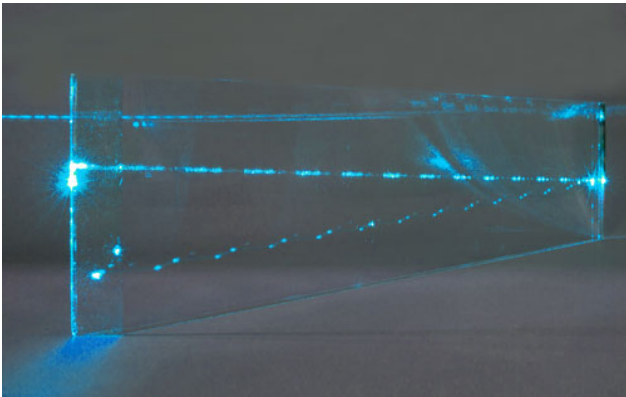


Fig. 40. Internal reflection of light in fused silica demonstrated with a laser pointer.

an optical outlet allows it to exit and reach the photomultiplier tube cathode. Figure 39 schematically shows this concept. For potential background particles with $\beta < 0.85$ the Cherenkov angle is smaller, resulting in more losses of light from these events and thus improving the signal-to-background ratio. In addition, the bar is wrapped in a highly reflective aluminum foil with a thin layer of air (0.2mm) in between. The foil helps to contain the light within the detector element and thus enhances the signal yield. The photograph in Fig. 40 visualizes the effect of total internal reflection with a blue laser pointer.

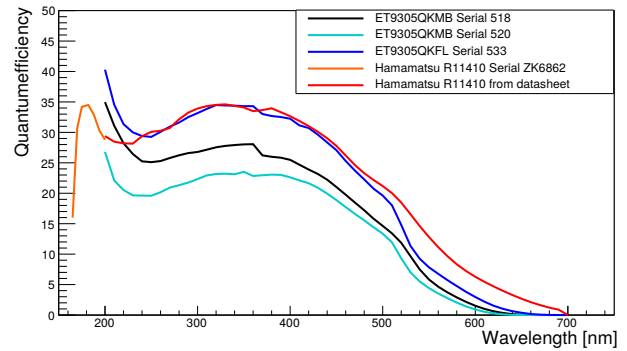


Fig. 41. Spectral responses of three different models of PMTs which are suitable for Cherenkov light detection.

5.2.3 Photomultipliers

The photomultipliers for the integrating detectors have to satisfy five main criteria: (1) high efficiency in the UV, (2) support for high cathode currents, (3) uniform sheet resistivity across the photocathode, (4) good linearity at relatively low bias voltages for current mode, and (5) fast charge collection at high bias voltages for tracking mode operation. The last two criteria are as much dependent on the base design as they are on the PMT itself. Three models of photomultipliers have been investigated, all especially developed for UV usage:

- ElectronTubes 9305QKMB;
- ElectronTubes 9305QKFL;
- Hamamatsu R11410.

All three are 78 mm in diameter with an effective area of 64 mm. They all have UV sensitive bi-alkali cathodes and quartz windows for good transmission of short wavelengths. Their spectral responses are plotted in Fig 41. The two specimen of the ET9305QKMB as well as the ET9305QKFL were individually calibrated for wavelengths ranging from 200 nm to 800 nm. The Hamamatsu PMT was only calibrated from 165 nm to 200 nm. The data for longer wavelengths was taken from the manufacturer data sheet.

The data in Fig. 42 was taken during a test beam at MAMI, where we used a prototype detector element with exchangeable PMTs. Each assembly was then irradiated with beam electrons of 195 MeV and the number of photoelectrons from the PMT cathode per electron incidence onto the detector was determined for different angles between beam and quartz surface, 0° being perpendicular. The requirement of Eq. (67) is met with each one of those PMTs.

Since the detectors are to be operated both in current mode (low gain), and tracking or event mode (high gain), we require a base that is remotely switchable between these two modes. A prototype base has been developed and tested with the prototype detectors at the MAMI facility. The schematic for the base is shown in Fig. 43. This is an active base design, using FETs and diodes to stabilize the gain behavior of the PMT at high event rates. The

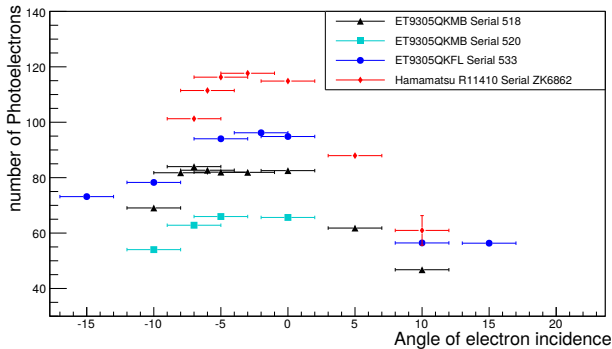


Fig. 42. MAMI test beam data from detector element prototypes with the different PMTs.

base implements the switching mechanism using photomos relays, the viability of which still requires radiation hardness testing. Alternatively, we can implement the switching mechanism with standard radiation-hard relays.

It is very important that the PMT and base system design interfaces well with the constraints placed on the integrating and event mode front-end electronics. For the integration mode measurement, the interdependencies that need to be optimized with respect to each other are summarized in the list given below and discussed in detail in Sect. 5.3. The complete main detector system layout is shown in Fig 45.

1. The PMT base design and the corresponding gain are set by the amount of charge that can be drawn from the PMT cathode and dynodes. The event rate, experiment running time and the number of photo-electrons per event determine the former, while the base design determines the latter.
2. The linearity of the PMT-base system deteriorates at lower gain (lower bias voltage), but higher gain means a larger anode current and higher charge drawn on the dynodes.
3. The integrating measurement noise bandwidth requirements (see Sect. 5.3) limit the available gain range for the preamplifier, which influences the minimum (and maximum) anode current that can be accommodated by the rest of the front-end electronics.

5.2.4 Prototype tests and Geant4 simulation of the detector response

Extensive material studies and prototype tests for the P2 Cherenkov detector have been performed between 2013 and 2016, examining different Cherenkov medium materials, photosensors, wrapping material, reflectors and detector geometries. Following a period of material and geometry considerations and studies, several detector elements have been tested at the MAMI beam with low currents of 195 MeV electrons in order to measure the signal yield of single events.

As an example, Fig. 46 shows the result of a run series with the detector design described in Sect. 5.2.1 and listed

| | |
|----------------------|------------------------------|
| Electron energy | 195 MeV |
| Beam rate | 3 KHz |
| Cherenkov medium | Spectrosil 2000 |
| Polish | Optical polish |
| Geometry | 650 mm long wedged (Fig. 35) |
| Photomultiplier | Hamamatsu R11410 ZK6862 Assy |
| Reflective wrapping | Alanod 4300UP |
| Light tight wrapping | 0.3 mm Vinyl |

Table 14. Run conditions and prototype setup for measurements and simulation shown in Fig. 46.

in Tab. 14. In order to measure the signal dependence on the angle of the particle incidence onto the detector surface, the prototype was rotated with respect to the MAMI beam line. Due to the effect of total internal reflection the number of photocathode electrons is highest for perpendicular impact.

These measurements were used to benchmark a Geant4 simulation with optical photon processes. Within this simulation, several particle types with properties expected for P2 signal electrons and background were shot onto different positions of the detector bars at different impact angles. As primary photon production processes, the Cherenkov process, and scintillation processes (not relevant in quartz) are implemented. Additional particles resulting into signal contributions can be created by pair production, Compton scattering, and bremsstrahlung.

The detector geometry and the materials were defined along with their optical properties as functions of the photon energies: refractive indices ($n(\lambda)$), light transmittance ($T(\lambda)$), and surface properties. The photons are then subject to wavelength dependent processes, namely refraction, reflection, absorption, and Rayleigh scattering. A typical simulated electron impact event onto one of the detector elements is visualized in Fig. 47.

At the position of the PMT cathode, the simulation contains a sensitive volume, which detects all particles passing through including their type, total energy, momentum direction, creation process, and place of origin. Using this information along with the cathode's quantum efficiency, the simulation can determine the number of photo-electrons per event. Figure 46 contains test beam results as well as simulated data generated using the same detector geometry, material properties, and primary particle characteristics. Thus, measured and simulated data can be directly compared. Both share the same characteristic angle dependence and agree well in the magnitude of the photo-electron signal.

The Monte Carlo simulation described in Sect. 5.1 delivers a rate distribution of particles hitting the Cherenkov detector plane. Figure 29 shows the particle rates incident on the detector ring for different particle types as a function of the radial distance from the z -axis. Particles are divided into two groups: the ones originating from an elastic ep scattering process and background particles. We see a very prominent photon background over-powering the signal electrons by one to two orders of magnitude.

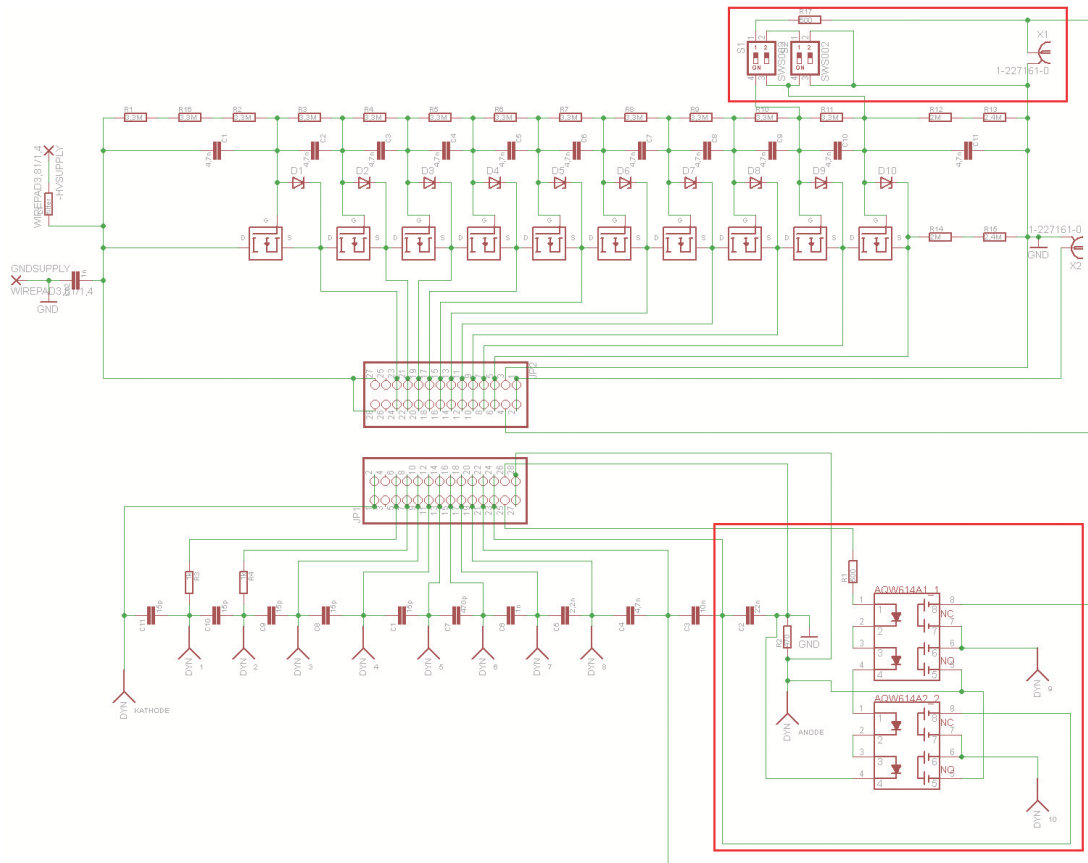


Fig. 43. Schematic of the PMT base prototype for the main Cherenkov detectors. This is an active base design, using FETs and diodes, to stabilize the gain behavior at high event rates. The base implements the switching mechanism, using photomos relays.

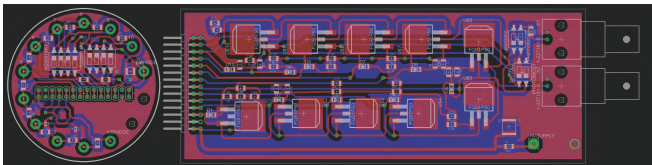


Fig. 44. PCB layout of the PMT base prototype for the main Cherenkov detectors.

The detector response simulation has been used to compile a comprehensive database of signal yields of particles hitting the detector. It includes the mean number of photo-electrons expected for electrons, positrons, and photons with energies ranging from 0 MeV to 155 MeV, various incidence positions, and incidence angles. Some example data is shown in Fig. 48.

Along with the particle information from the ray tracer simulation (Sect. 5.1) the event rates on the detector can now be converted into photo-electron rates which are plotted in Fig. 30 of Sect. 5.1. The background signal is suppressed by the small detector response to photons since they do not directly produce Cherenkov light. They only lead to a detector signal if they first convert into charged particles (e.g., by pair production or Compton scattering) inside the detector, and if the resulting particles are above

the Cherenkov threshold (0.71 MeV for electrons traveling through the quartz bars). The photon background in P2 is mainly below this threshold.

5.2.5 Radiation hardness

The energy deposition in 1 cm of quartz at 150 MeV is 15.5 MeV. The detector bars are going to cover an angle range of 25° to 45° , and we expect an electron rate of ~ 5 GHz onto each detector element, corresponding to an average of ~ 20 MHz/cm² and a deposited energy of 5×10^{-5} J/(s · cm³). This leads to an absorbed radiation dose of ~ 80 Mrad over the data taking time of 10 000 h. The material used for the detector components must be able to endure this radiation. It has been shown that for quartz, low contamination levels lead to low susceptibility to radiation damage. The PANDA DIRC group has done extensive studies with Spectrosil 2000 by irradiating the material with photons up to a dose of 100 krad and — in another study — with protons up to 10 Mrad [96,97]. The research has demonstrated the extraordinary radiation hardness of synthetic fused silica.

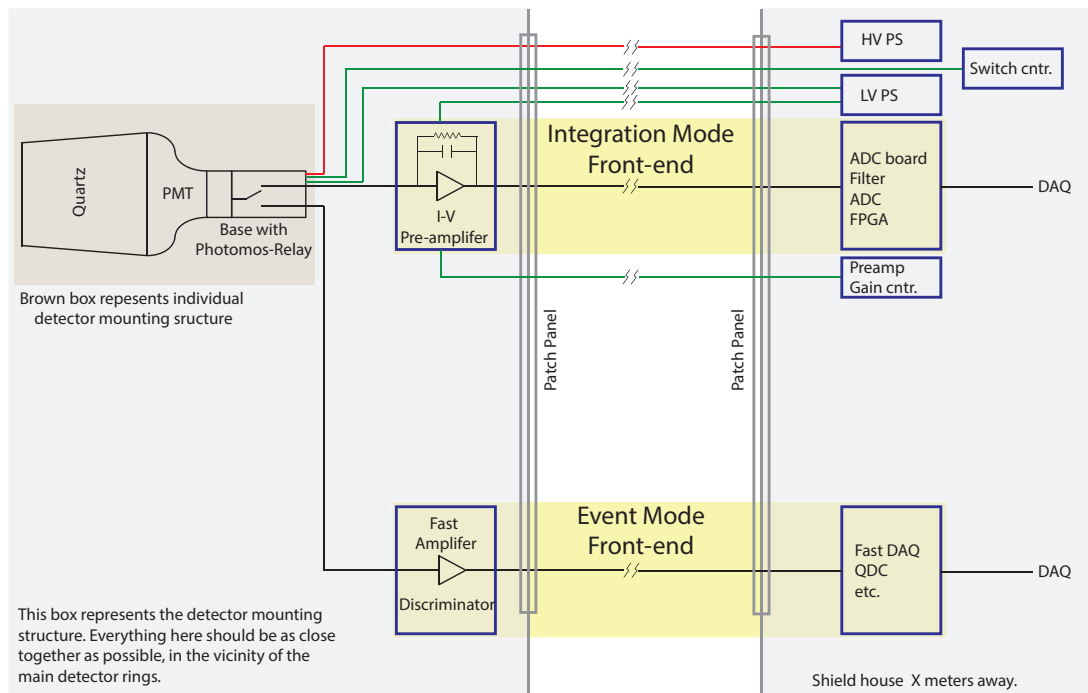


Fig. 45. Schematic layout of the main detector system, including the separate integration mode and event (tracking) mode signal chains. Also shown are the modules that control the PMT base switching and the gain adjustment for the preamplifiers. The low voltage power supplies needed for the base and preamplifier circuits are also shown, along with the high-voltage power supplies. The details of the integration mode front-end electronics system are discussed in Sect. 5.3.

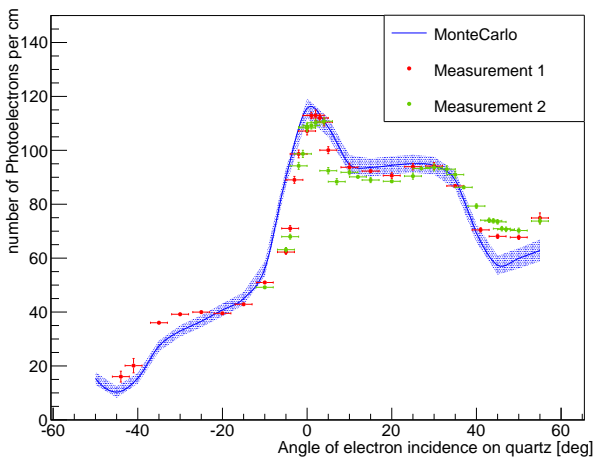


Fig. 46. Measurement results and Monte Carlo simulation of the photo-electron yield per electron event onto the detector element for angles of electron incidence ranging from -50° to 55° , the maximum signal being at perpendicular electron incidence onto the quartz surface.

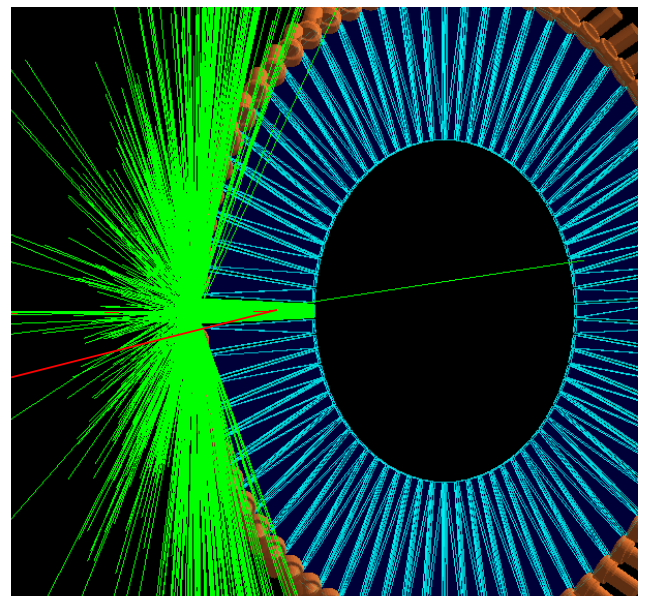


Fig. 47. Visualization of electron incidence on detector element. In red: electron, green: photons

5.3 High resolution ADCs

The small asymmetries and the precision goal for P2 require very high statistics, meaning very high event rates in the detectors. Given the needed accuracy of the proposed experiment, background susceptibility, linearity, noise behavior, and radiation hardness are major issues. For these

reasons, P2 has adopted radiation hard, highly linear, and relatively large active area ($O(100\text{ cm}^2)$) fused silica (quartz) Cherenkov detectors. The anticipated total rate in a given detector is on the order of one to several GHz. At these detector rates the counting of individual pulses is no longer possible, requiring integration mode opera-

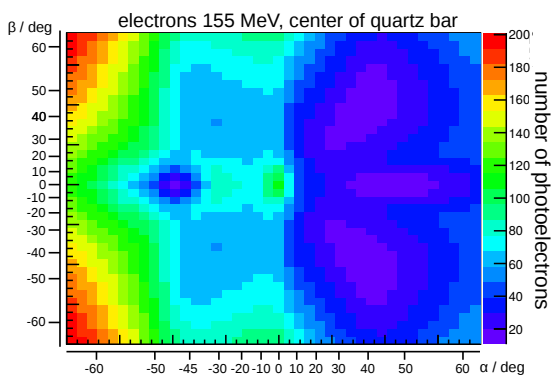


Fig. 48. A small fraction of the detector response database as an example. The number of photoelectrons is plotted for electrons of 155 MeV hitting a detector module at the center of the active at a range of different angles to the detector surface.

tion, in which individual pulses overlap to such a degree, that they produce a continuous current at the detector output (therefore this is also sometimes referred to as current mode detection, as opposed to pulse mode). The electronics discussed in this section refers to the integrating mode electronics for these detectors, as well as the beam monitors, which are used to normalize the detector signal and should therefore, ideally, have the same digitization scheme, as further discussed below. Due to the similarities in the detection and measurement methodologies with the QWeak experiment [98, 64], the P2 design introduced here is based on the design of and experience with the front-end electronics for the QWeak integrating detectors.

5.3.1 Integrating detector signal chain

The proposed P2 integration or current mode measurement front-end signal chain is shown in Fig. 49. The light from the quartz is converted to a current using quartz glass photomultiplier tubes (PMT) with a high quantum efficiency (QE) in the UV. At a nominal rate of 1 GHz and for a given detector geometry with a photo-electron yield of 50 pe per primary electron, a mean current of roughly 8 μA is produced at the anode of a PMT with a gain of about 1000. A trans-impedance preamplifier is used to convert the current signal to a voltage and to provide the primary filtering stage for the signal. The voltage signal is then further filtered and digitized by an ADC. Several channels of the filter and ADC chain are implemented on a single board, together with an FPGA, which queries the ADCs, collects (meaning in this case integrates) the data and facilitates the readout. The preamplifier also implements a line driver to sustain the signal over the longer cable distance between the detectors and the ADC. The preamplifiers and the integrating ADC boards are the main subject of this section.

The design of the electronics is, of course, dictated by the properties of the signal, including the mean amplitude,

the RMS width, noise sources, and expected variation as a function of helicity. For the purposes of discussing the integrating electronics, the electronic signal from a single detector (i) can be written as

$$I_i^\pm(t) = I_{i_P}^\pm(t) + \sum_B I_{i_B}^\pm(t) + I_{i_D}(t). \quad (69)$$

This is the current that is present at the anode of the PMT, where $I_{i_P}^\pm(t)$ is the contribution to the current from the physics process of interest (elastically scattered electrons and the secondaries they produce, indicated by the subscript P), the sum over $I_{i_B}^\pm(t)$ is the contribution from the various background processes (indicated by the subscript B), and $I_{i_D}(t)$ is the dark current (indicated by the subscript D). The current is converted to a voltage by an I-to-V amplifier with a gain of $g_{Amp_i}^\pm(t)$, in units of Ohms, so that the corresponding voltage yield is

$$V_i^\pm(t) = g_{Amp_i}^\pm(t) I_i^\pm(t) + V_{i_E}^\pm(t). \quad (70)$$

Equation (70) includes a voltage contribution ($V_{i_E}^\pm(t)$) from a possible amplifier offset and the voltage signal corresponding to the dark current can contain helicity dependence due to possible electronic coupling of the helicity signal in the preamplifier. The latter should be suppressed or eliminated if possible through the use of appropriate signal isolation (avoidance of ground loops, signal isolation, the use of fiber optics, etc.).

For measurements in integration-mode, the counting statistics manifests itself primarily in the root-mean-square (RMS) width of the shot noise at the PMT anode, which has contributions from all sources that generate an anode current, including background and dark current. To get the total RMS width in the signal, as it is sampled by the ADC, one has to add all sources of electronic noise $\sigma_{i_E}^2$, which includes resistive (Johnson) noise, as well as noise introduced by active components and filters. The total squared RMS noise density in the signal is then given by

$$\sigma_i^2 = 2Q_{i_P} I_{i_P} + \sum_B 2Q_{i_B} I_{i_B} + 2Q_{i_D} I_{i_D} + \sigma_{i_E}^2 \quad (71)$$

where $I_{i_{P,B,D}} = \langle I_{i_{P,B,D}}^\pm(t) \rangle$ is the mean anode current and $Q_{i_{P,B,D}} = \langle Q_{i_{P,B,D}}(t) \rangle$ is the mean quantum of charge at the anode. For the anode current this is simply a time average, but for the charge quantum the assumption is that this is the mean of a Poisson distribution and that the time integration for the current is done over a time period for which the quantum efficiency was stable. Note that, under ideal operating conditions, the dark current is dominated by thermionic emission of single electrons at the cathode, so that $Q_{i_D}(t) = g_{PMT_i}(t) e^-$ and the corresponding dark current is given by $I_{i_D}(t) = AT^2(t) e^{-(W)/kT(t)}$, where A is constant depending on the cathode material and size, T is the temperature in Kelvin, W is the (field modified) work function of the cathode material, and k is the Boltzmann constant.

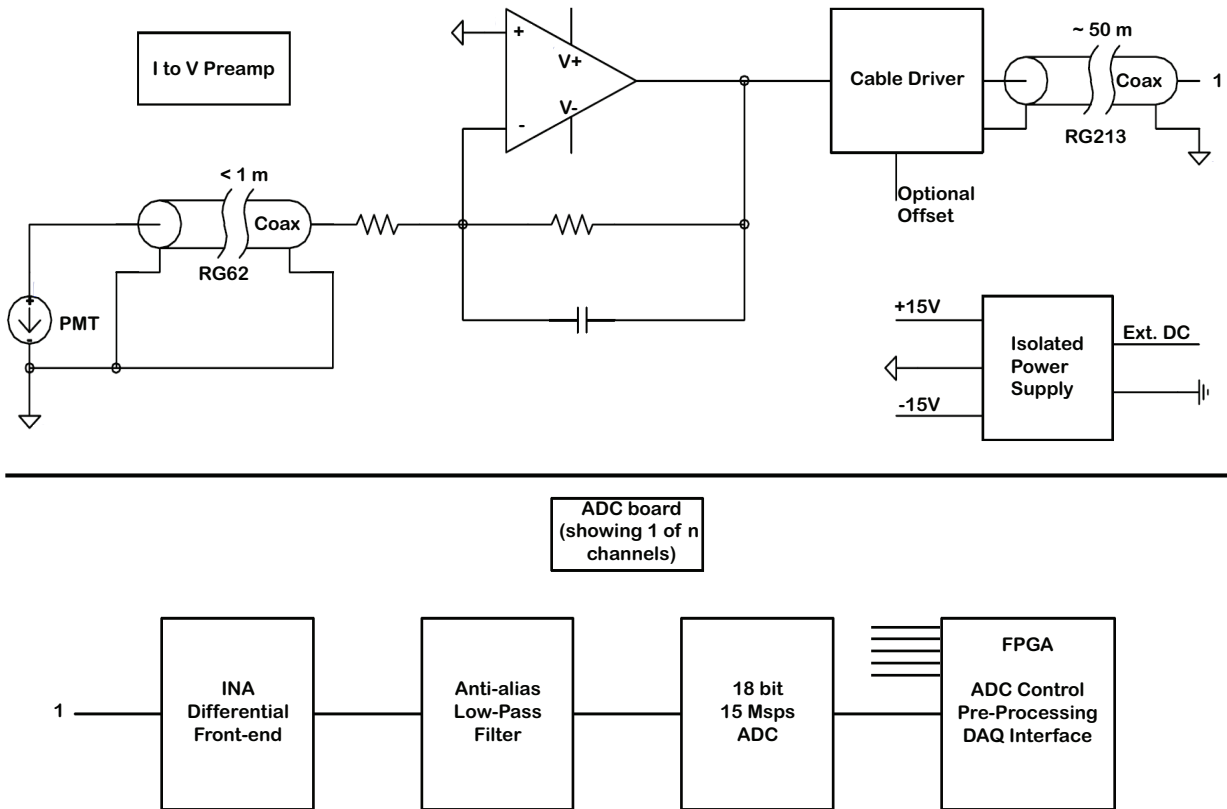


Fig. 49. Schematic of the front-end signal path for integration mode measurements. The continuous current signal from the PMT will be converted to a voltage signal using a trans-impedance amplifier. A cable driver will maintain the signal strength from the amplifier to the ADC board, which is located away from the detector behind a shielding wall. The filtered amplifier signal will be digitized by a high resolution ADC and the digitized data will be pre-processed and transmitted to the DAQ system using an FPGA.

In the expressions above, a possible, explicit dependence on helicity state of a given parameter is indicated by the \pm superscript, while explicit time dependence (both slow and fast), that is generally not correlated with the helicity state is indicated by the continuous time parametrization (t). Aside from the physics asymmetries, the variation of various parameters with the helicity state of the beam may be a result of either electronic coupling of the helicity signal or direct variations in the beam as a function of helicity state. Examples of the former would be the coupling of the helicity gate into the signal that comes from the detector preamplifiers $g_{Amp_i}^\pm(t)$ or the ADC electronics $V_{i_E}^\pm(t)$. Helicity correlated changes in beam conditions result in explicit changes of the rate seen in the detectors, even in the absence of any asymmetry that results from the interaction of the primary beam in the target or the rest of the experiment. Continuous time dependence in the detector signal is primarily due to variations in the beam current, target conditions, electronic drifts, temperature fluctuations, and PMT ageing, but also due to electronic drifts. A great deal of effort goes into the overall experimental design and analysis methods to remove or mitigate the dependencies on these unwanted experimental factors

and many of the solutions are explicitly related to or influence the design of the integrating electronics.

5.3.2 Design criteria for the integrating electronics

The list below briefly describes the requirements the integrating electronics has to satisfy.

1. Helicity correlated changes in the beam (current, energy, position, and angle) are unavoidable, but they can be minimized to some degree and they can be measured using charge and position monitors. The experiment will be designed to measure the sensitivity of the detectors to these beam changes. The sensitivity measurements are made by measuring the correlation between the changes measured with the beam monitors to those measured with the detectors, which requires that the electronics chain used to process the measurements from the beam monitors is identical to that of the integrating detectors. This is particularly important in the case of the beam current monitors, since the integrating detector signal is normalized to the current monitor signal to remove random drifts,

fast fluctuations, and helicity correlated changes, in the beam current.

2. Random and systematic drifts in the detector signal $V_i^\pm(t) \rightarrow V_i^\pm$: The detector signal contains random changes and systematic drifts, both fast and slow. The slow drifts emerge due to variations in beam current, target conditions (target boiling and slower density changes), electronic drifts, temperature fluctuations, and PMT ageing. Almost all of these can be controlled to some degree (for example by operating the PMTs at a reasonable HV bias, in a reasonably stable temperature environment, and removed from or shielded from direct radiation exposure), but the primary way to deal with possible false asymmetries due to drifts and unwanted noise above shot noise, due to large amplitude random drifts, is to perform each asymmetry measurement on a timescale that is short compared to the timescale of the drifts. This is achieved by running the experiments with a fast helicity reversal rate (currently planned $\simeq 1$ kHz) and a suitable choice of helicity patterns. Helicity quartets such as $+--+$ and $-++-$ remove linear drifts and the introduction of pseudo-random initial state (\pm) of the quartet removes quadratic drifts. The faster the helicity reversal rate, the more the signal variation with respect to time is well approximated as constant on the timescale of an asymmetry calculation:

$$A_{i_{raw}} = \frac{V_i^+(t_+) - V_i^-(t_-)}{V_i^+(t_+) + V_i^-(t_-)} \rightarrow \frac{V_i^+ - V_i^-}{V_i^+ + V_i^-}.$$

Random variations that are faster than the helicity reversal rate are dealt with and used to advantage in the electronics chain, as described in detail below. The choice of helicity reversal rate influences or determines almost every detail of the electronics design.

3. Minimization of electronics noise contribution:

$$\sigma_{i_E}^2 \ll 2Q_{i_P} I_{i_P} + \sum_B 2Q_{i_B} I_{i_B} + 2Q_{i_D} I_{i_D}.$$

4. Minimization of drift effects and helicity correlated electronic pickup in the pedestal: $V_{i_E}^\pm(t) \rightarrow V_{i_E}$.
5. Minimization of drift effects and helicity correlated electronic pickup in the amplifier: $g_{Amp_i}^\pm(t) \rightarrow g_{Amp_i}$.
6. Bandwidth matching of all electronic components and between the various detectors that will be read out in integrating mode.
7. Optimization of ADC resolution and sampling rate with respect to a 1 kHz reversal signal and the 1 MHz input bandwidth is required to follow (resolve) the helicity reversal signal transition (see below).

5.4 Signal structure and sampling scheme

Figure 50 shows a 2-minute period of the raw and beam current normalized signals for one of the QWeak integrating detectors. This data corresponds to an integration with an equivalent bandwidth of half the helicity reversal

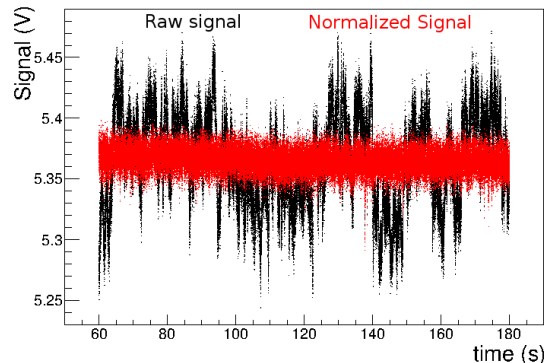


Fig. 50. Example period of a signal from one of the QWeak integrating detectors. The black data shows the raw, unnormalized yield and the red data shows the beam current normalized yield.

rate (480 Hz), since the data for each helicity window is averaged to one value per helicity window, in the FPGA, after sampling. Even after normalization, drifts can be seen at timescales down to seconds, along with much longer drifts, and large non-Gaussian drops in yield, due to target boiling, can be seen at much shorter timescales (around 30 ms). A high helicity reversal rate prevents these types of drifts from producing false asymmetries and reduces the contribution to the RMS width in the asymmetry signal, due to these effects. For a mean signal of, say, 4 V a physics asymmetry of 40×10^{-9} produces a shift in the mean of about 0.16 μ V, which is much smaller than the observed RMS width of a few mV. Since the bit resolution of even the best ADCs today is not high enough to measure a signal difference at that level, in a single sample, the combination of a suitable bandwidth selection and a high rate of oversampling is used to increase the effective bit resolution of the ADC.

Figure 51 illustrates the division of the integration mode detector signal into sampling regions. The period sampled for the physics measurement must be stable, which means that the time periods corresponding to the Pockels cell settling and ADC stability are excluded. However, it is important that the electronics be designed to allow sampling during the excluded time periods, so that the settling time can be monitored and used for systematic checks. The example in Fig. 51 shows the time structure used for the QWeak experiment, with a helicity reversal rate of 960 Hz, Pockels cell settling time of 70 μ s, and an ADC delay of 42.5 μ s. For P2, the reversal rate will be 1 kHz and the goal Pockels cell settling time is 10 μ s. This means that the integrating electronics settling should be correspondingly faster and operate at a higher sampling rate. The primary goal of the integrating electronics is to match the ADC bit resolution and sampling rate with the detector signal bandwidth needed to follow the changes in the beam (related to the helicity change and otherwise).

Figure 52 illustrates the concept behind the oversampling. The right hand side of the figure shows two simulated data sets (red and blue) for which the mean value

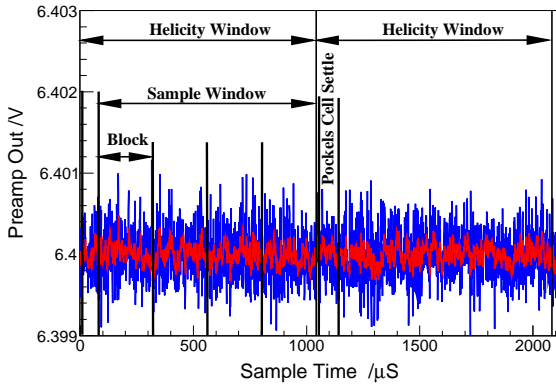


Fig. 51. Integration mode detector signal (simulated Gaussian white noise) at the preamplifier output with a 500 kHz bandwidth (blue) and a 25 kHz bandwidth (red) and how this signal is divided into helicity windows and sampling regions. A primary goal of the integrating electronics is to match the ADC bit resolution and sampling rate with the detector signal bandwidth needed to follow the changes in the beam (related to the helicity change and otherwise).

differs (e.g., as a result of an asymmetry), as a function of sample time. The left hand side shows the samples accumulated by the ADC in histogram form. In this simulated data set, the mean difference between the two data sets is 20 mV, while the bin width in the histogram, which represent the resolution of the ADC, corresponds to 25 mV. Both of these values are exaggerated for illustrative purposes, but they show the general effect. The ADC resolution is too large to resolve the difference in the signal caused by the asymmetry, but the signal is sampled many times within each period (i.e., the helicity window) and the mean difference of the two distributions is clearly visible. This only works effectively, if the RMS width in the signal is significantly larger than the resolution of the ADC ($\Delta = V_{ref}/2^n$ for an n -bit ADC), which then automatically exceeds the digitization error in the ADC $\sigma_d = \Delta/\sqrt{12}$. Another benefit of the larger RMS width in the signal is that the ADC differential non-linearity becomes less and less significant while increasing the number of ADC channels over which the signal is spread. The experimental design and a suitable choice for the bandwidth in the preamplifiers and filters at the ADC input will ensure that this requirement is satisfied. The final ADC has to be chosen to have an integral non-linearity that is as small as possible, but since the difference in the mean of the signal for any pair of opposite helicity windows is smaller than the ADC resolution, the resulting distortions in the output distributions (left-hand panel in Fig. 52) for a given helicity pair will be nearly the same and the averaging over a large number of ADC bins, inherent in the this sampling scheme, reduces the effect further. For most good ADCs, the integral non-linearity as a function of ADC output code is distributed around 0 ± 0.6 LSB.

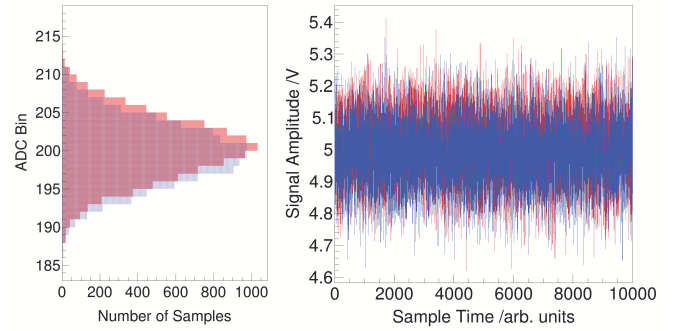


Fig. 52. Illustration of the concept behind oversampling. The right-hand side of the figure shows two simulated data sets (red and blue) for which the mean value differs (e.g., as a result of an asymmetry), as a function of sample time. The left-hand side shows the samples accumulated by the ADC in histogram form, where the bin width of the histogram is synonymous with the resolution of the corresponding ADC. The difference is again shown in red and blue, with the darker region being the overlap of the two distributions. The difference in the mean for the two signals is 20 mV, while the bin width (ADC resolution) is 25 mV, but the oversampling, together with the large RMS width in the signal, allows a high precision difference measurement between two helicity windows.

5.4.1 Bandwidth requirements

The lower limit to the system bandwidth is set by the need to follow the helicity flip settling time. The goal for the settling is 10 μ s and the front-end electronics has to be fast enough to follow this transition, to ensure that the amount of lost data within a helicity window is minimized. This means that the preamplifier output should also settle, within a certain accuracy relative to the mean helicity signal level, within a few μ s. Taking a rate of 100 GHz in the detectors (approximately, from primary scattered electrons only), counting statistics within a single 1 ms helicity window is about 100 ppm. Assuming that the noise from ringing during helicity transitions is perfectly correlated in all detectors and that we want the corresponding peak-to-peak variations to be much smaller than the counting statistics noise (shot-noise), we demand that the amplifier must settle to 0.001 % (10 ppm) within a time window that is small compared to the helicity flip settling time. A single pole filter with a signal bandwidth cutoff of $f_{3\text{dB}} = 1$ MHz has a time constant of $RC \simeq 0.16$ μ s and reaches the desired settling in $t_s = -\ln(0.001/100) \cdot RC \simeq 2$ μ s, which is reasonable and also allows for some component variation and monitoring of additional ringing during the helicity transition. Suitable operational amplifiers for the preamplifiers have to be selected with these criteria in mind.

5.4.2 The preamplifier

The design of the P2 integrating electronics will be based on the QWeak electronics, but will be modified to satisfy, primarily, the criteria for higher bandwidth discussed

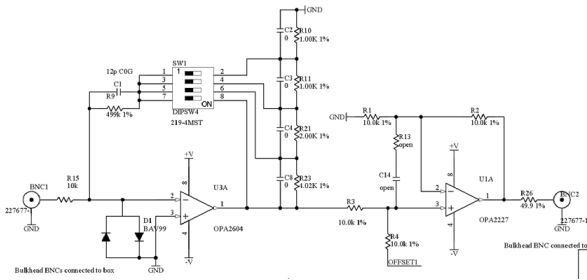


Fig. 53. QWeak style trans-impedance preamplifier schematic. The gain is set by a selectable feedback amplifier, using a dip switch. The bandwidth is mainly determined by the parallel capacitor-resistor pair (C1 and R9).

above. The schematic for a single channel of the QWeak preamplifier is shown below, in Fig. 53. The inputs are protected with a combination of resistors and diodes. Each channel has a separate set of switches that set the gain between various values (here shown for QWeak, between 0.5 and 4.0 M Ω). The bandwidth is primarily set by the parallel C1/R9 capacitor resistor feedback circuit, which was 25 kHz for QWeak. The displayed operational amplifier (OPA2604) can not support the desired 1 MHz bandwidth at the needed gains, so we will have to choose a different OpAmp, or implement a second gain stage. The constraints for the achievable signal bandwidth are set by the competing needs for the feedback capacitance (C_F) (which controls the noise behavior), feedback resistance (R_F) (which sets the overall gain), and the gain bandwidth product of the OpAmp. The two relevant relations are $f_{SB} \leq 1/2\pi R_F C_F$ and $f_{GB} > (C_{IN} + C_F)/2\pi R_F C_F^2$, where f_{SB} is the desired signal bandwidth, f_{GB} is the gain bandwidth of the OpAmp (which is 20 MHz for the OPA2604 used for the QWeak design), and C_{IN} is the capacitance at the amplifier input, which is a combination of the OpAmp input capacitances, the PMT capacitance, and the cable capacitance. The latter two are, of course, dependent on the PMT base design and the cable length needed to connect the PMTs to the preamplifiers. The QWeak amplifier also implemented an offset control that sets an output bias voltage on each channel, to provide an indication that the preamp is powered and connected. An external 5V source powers an isolated DC-DC converter to supply ± 15 V internally.

5.4.3 The integrating ADC

As discussed in Sect. 5.4, two critically important parameters for the integrating detector ADCs will be the sampling rate and the amplitude or bit resolution. These are also competing parameters, in that ADCs with a high-bit resolution tend to have lower sampling rates and vice versa. Today, one can buy high performance, low noise, ADCs with 18 to 24 bit resolution and sampling speeds of several Msp. For P2, 18 bit resolution is sufficient, given that the experiment will use the oversampling scheme de-

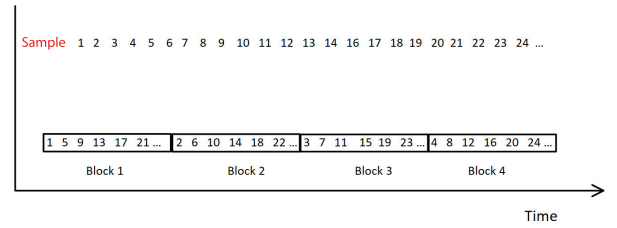


Fig. 54. Each helicity period can be separated into 4 blocks which are normally populated by samples taken in sequence. For diagnostic purposes relating to possible phase slippage in detector signals (particularly between the beam monitors and the integrating detectors), it is desirable to have only every n th sample (up to $n = 4$) in a given block, as illustrated in this figure.

scribed in Sect. 5.4. A suitable ADC has been identified¹, with a sampling speed of 15 Msp, which is significantly above the minimum required for the desired 1 MHz signal bandwidth.

For an event rate of 1 GHz, a PMT gain of 1000, and about 50 photo-electrons at the cathode, per event, the average current from a single detector would be about 8 μ A. Assuming also that the background and electronic noise contributions are negligible, Eq. (71) gives an estimated RMS width in the detector signal ($\sqrt{2Q_{i_P} I_{i_P} B}$) of about 0.36 μ A (for a 1 MHz signal bandwidth). A preamplifier gain of 0.2 M Ω would then produce a signal at the ADC, with a mean of 2 V and an RMS of about 90 mV. The 18 bit ADC currently under consideration has a full scale voltage range of $V_{fs} = \pm 4.096$ V and has a resolution of $V_{Ref}/2^{18} = 4.096 \text{ V}/2^{18} \simeq 16 \mu\text{V}$, which means that a signal with an RMS width of 90 mV would be spread over more than 5625 ADC channels, which is more than enough to make the digitization noise and non-linearity negligible, as discussed above.

5.4.4 Back-end data processing, readout, and DAQ interface

As illustrated in Fig. 51, the signal readout for the QWeak experiment included the option to split the signal into four blocks of consecutive samples, for diagnostic purposes, and this capability should be retained for the P2 design. In addition to this, it is desirable to implement the possibility to accumulate only every n th sample in a given block, as illustrated in Fig. 54, primarily to monitor the effects of possible phase slippage between the integrating detectors and the beam monitors.

The QWeak design only allowed the readout of the sample sum for each entire helicity window and the sums for the four separate blocks within each helicity window. It is desirable to implement the readout of additional information in the data stream for each data block, such as the minimum sample value, maximum sample value, and RMS of the samples in each block. In addition, for

¹ Analog Devices <http://www.linear.com/product/LTC2387-18>

diagnostic purposes, it is often desirable to obtain the fast Fourier transform of the actual signal, as it is sampled by the ADC. For this to work, it is necessary to implement the possibility of reading out every ADC sample, at a lower event rate (tracking rates), rather than only producing integrated numbers for each helicity window. This mode basically amounts to running the ADCs as slow waveform digitizers. This pre-processing of the ADC data will be implemented with an FPGA. For the purpose of commissioning, when the DAQ is being synchronized with the rest of the experiment, it will be necessary to have front panel outputs and data stream information about when exactly the FPGA starts and stops accumulating ADC samples after the helicity gate. The ADC will be controlled by an external clock that is synchronized to the helicity reversal. The ADC data will be read out via Gbit ethernet connections for each module.

5.5 Tracking detectors

Depending on the scattering position along the target, the solenoidal field will map different scattering angles into the acceptance of the integrating Cherenkov detectors. A tracking detector is needed to determine this relationship and ultimately the average squared momentum transfer $\langle Q^2 \rangle$ of the electrons entering the asymmetry determination. High resolution tracking also allows for the study of backgrounds and position and momentum dependent systematic effects.

The tracking detector geometry and reconstruction was developed using a full Geant4 [91,92,93] based simulation of the P2 setup including a detailed field map based on the FOPI solenoid magnet [95].

5.5.1 Tracker operation modes

Two main modes of operation are foreseen for the tracker, one at low rates, where the Cherenkov detectors can be operated in single electron detection mode and coincidences with the tracker can be formed. A second mode at high rates is used to study rate, position and momentum dependent systematic effects; here the tracking detectors will be gated in order to keep the data acquisition rate manageable.

The first mode requires that the tracker acceptance at the very least covers all electrons that can reach one fused silica bar with very high efficiency, whilst the second mode demands a very fast, radiation tolerant detector with a geometry that allows for a reliable track reconstruction also at high occupancy. The low electron momentum and the reduction of background from photons created in the tracker put very stringent constraints on the tracker material budget.

5.5.2 Tracker geometry

The tracking detector uses the curvature in the magnetic field for momentum measurements, requiring placement

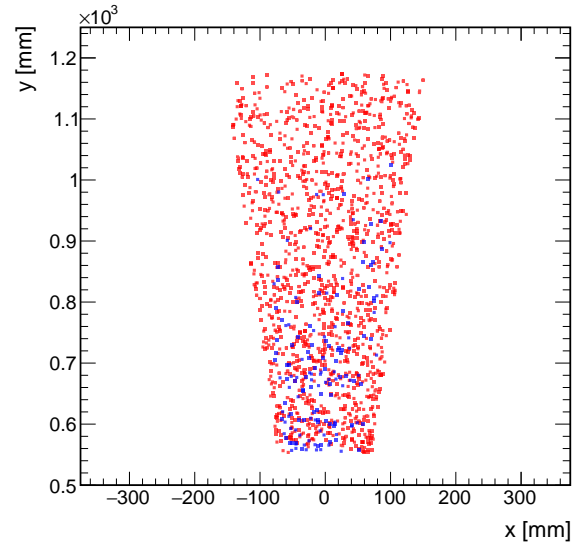


Fig. 55. Simulated hit distribution in a segment of the first tracker plane at full rate and with a 50ns integration window. About one in thousand bremsstrahlung photons leaves a hit (red dots). The signal electrons cause the hits indicated with blue dots. A coordinate system centered in the solenoid center and with the z axis along the beam direction is employed.

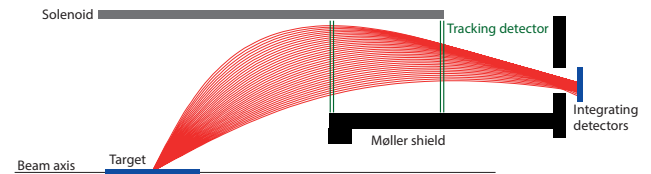


Fig. 56. Schematic view of the tracking detector geometry.

in the solenoid and thus prevents a complete geometric shielding of the bremsstrahlung photons created in the target. Indeed, the first tracker plane is impinged by up to six orders of magnitude more photons than signal electrons. This in turn requires again a very thin tracker to minimize the photon interaction probability and a geometry that allows for a robust track reconstruction with a very adverse signal-to-background ratio of tracker hits (see Fig. 55). Such a robust track reconstruction can be achieved by tracking plane pairs spaced by roughly the typical distance of two hits on a single plane at full occupancy (≈ 1 cm to 2 cm).

For the low momentum tracks expected in P2, multiple Coulomb scattering in detector material is the main effect determining momentum resolution. It is thus desirable to have a long, material-free region to obtain a good curvature measurement. The demands of the reconstruction and good momentum resolution can be met by two double planes separated by a wide, empty drift region, the geometry chosen for P2, see the schematic view in Fig. 56.

The $\langle Q^2 \rangle$ determination does not require full azimuthal coverage of the tracker; the active area should however be large enough to cover virtually all electrons heading for

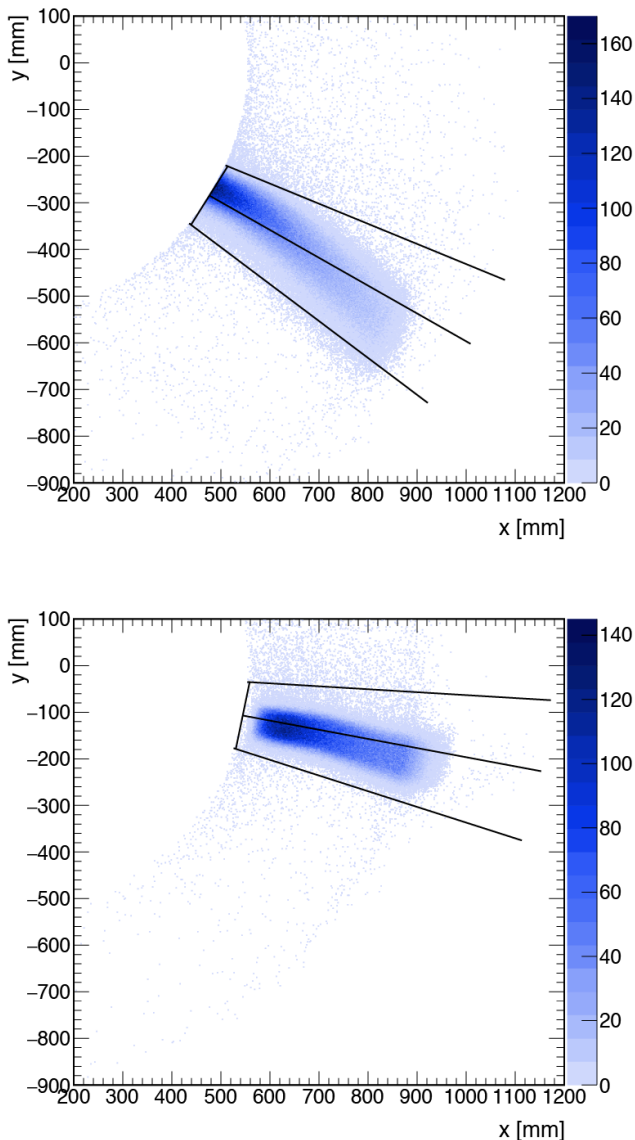


Fig. 57. Simulated intercept of the electron trajectories ending in one fused silica bar with the first (closest to the target, top) and last (closest to the silica bar, bottom) tracking plane. The active area and the centerline of a tracking panel are indicated with the black lines.

one fused silica bar. This can be achieved by tracker segments covering 15° , see Fig. 57. We currently foresee four such segments to cover up-/down- and left-/right- asymmetries.

5.5.3 High-Voltage Monolithic Active Pixel Sensors

The P2 tracker requires active elements which are fast, thin, radiation hard and highly granular in order to deal with the high rates and low momentum tracks. High-Voltage Monolithic Active Pixel Sensors (HV-MAPS, see [99,

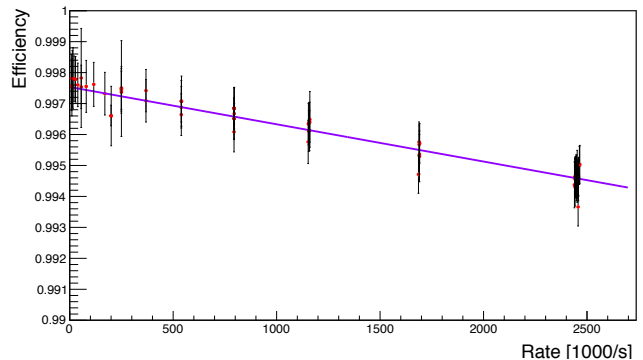


Fig. 58. Rate-dependent efficiency of a MuPix7 HV-MAPS prototype illuminated by a roughly $500\ \mu\text{m}$ diameter electron beam.

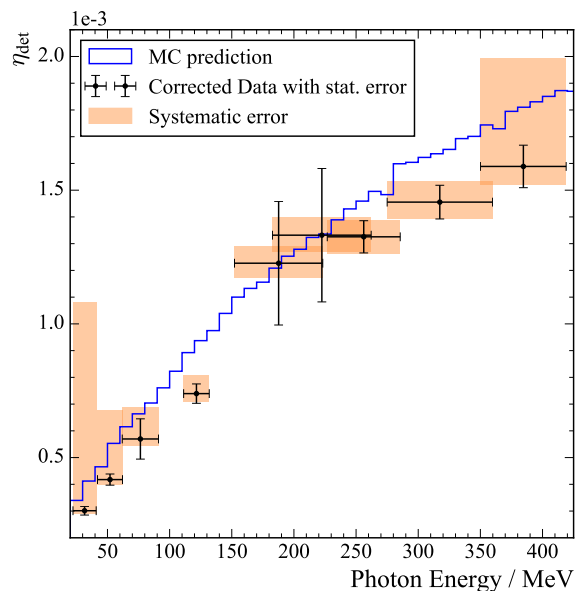


Fig. 59. Efficiency of MuPix7 sensors for high energy photons compared with the Geant4 based simulation.

100,101,102,103]) fulfill all these requirements. A commercial high-voltage CMOS process providing deep n -wells in a p -doped silicon substrate allows for reverse bias voltages of about 90 V between wells and substrate. This creates a thin, high-field depletion region, from which charge is quickly collected via drift. Inside the n -wells, complete CMOS electronics can be implemented, allowing for in-pixel amplifier circuits and complete signal digitization and processing on the same chip. The thin active region allows for thinning of the sensors to just $50\ \mu\text{m}$ thickness.

In the framework of the Mu3e collaboration [104], we have developed a series of HV-MAPS prototypes known as the MuPix chips [105,106]. With the MuPix7 prototype [107], we have produced a complete system-on-chip with a $3\ \text{mm} \times 3\ \text{mm}$ active pixel matrix with internal amplifiers and source followers, driving the signals to the chip

periphery, where hits are detected by a tunable comparator and timestamps are assigned. A state machine collects and serializes the hits and sends them off-chip using a 1.25 Gbit/s low-voltage differential signaling (LVDS) link. In this system, we have measured detection efficiencies well above 99% and a time resolution below 15 ns at noise rates below 1 Hz per pixel using a variety of beam tests at DESY, PSI, CERN and MAMI. High rate capability has been demonstrated by a MAMI beam test, where we illuminated a roughly 500 μm large spot with more than 2 MHz of 800 MeV electrons, leading to an efficiency loss consistent with the single pixel deadtime of about 1 μs , see Fig. 58. Despite no special design measures being taken, the sensors turn out to be very radiation hard [108].

Given the very large bremsstrahlung background expected in P2, it is imperative that the sensors have a small and well understood efficiency for detecting photons. To this end we have conducted tests with sources and at the A2 tagged photon facility at MAMI and find detection probabilities below 10×10^{-3} for photons in the few MeV energy range, see Fig. 59. The detection probability rises again towards lower energies and was found to be $\approx 30\%$ at 5.9 keV, again in good agreement with simulations [109].

We are currently testing the 2 cm \times 1 cm MuPix8 prototype in order to understand scaling effects in large sensors and prepare for the production of the final 2 cm \times 2 cm sensor.

5.5.4 Tracker segments

The tracker will consist of double layer segments covering 15° in azimuth and as much as mechanically possible of the radial space between the Møller shield and the magnet inner wall (535 mm to 1200 mm in radius). The active sensors will be cooled by gaseous helium.

Mechanics A tracker module, see Fig. 60, is built from 29 staggered strips on each side with a slight overlap of the sensors along the radial axis to prevent ineffective areas and a frame providing mechanical support, cooling and electrical connectivity. Depending on the radius, each strip is equipped with between 8 and 14 50 μm thin HV-MAPS sensors, the strip design is derived from the Mu3e design [110]. About 30 single point tape-automated bond connections [111] to an aluminum-polymide flexprint provide the supply voltages and transfer data and control signals. An additional polymide layer with V-shaped folds glued to the flexprint provides mechanical stability and cooling channels. The overall thickness of the active part of a strip is less than 0.12% of a radiation length.

The strip ends in a rigid printed circuit board (PCB) with a milled plastic cooling gas manifold on top; two different PCB thicknesses allow for the strip staggering. At both ends of the strip, these end PCBs are connected to a frame built from long PCBs and cooling ducts. Signals and power are connected via a high-density interposer. The azimuthal sides of the frame have a sliding system

and are tensioned by springs in order to compensate for thermal expansion of the strips. Two layers of strips are connected to the same frame such that the sensors face inwards towards each other with a distance of roughly 23 mm. The full module has 632 sensors.

The modules will be mounted on rails in their surrounding helium volume with the possibility to remove and re-insert them in a limited amount of time. This is in particular required for the runs with lead targets, where the radiation levels definitely exceed the tolerance of the tracker and gives the flexibility to also run without tracker in hydrogen mode in order to study systematics or perform repairs.

We are currently investigating two solutions for the powering of the HV-MAPS sensors, which require a 1.8 V supply voltage. Either this voltage is generated from an external 10 V supply via radiation hard DC-DC converters [112] mounted on the support frame or we employ a powering scheme, where several sensors are connected to the external supply in series; the required on-chip shunts are currently under test.

Cooling The HV-MAPS sensors are active and, depending on their settings, dissipate between 150 mW/cm² and 400 mW/cm². One module can thus produce in excess of 1 kW of heat, which needs to be actively cooled; any liquid coolant would however add unacceptable amounts of material in the active region. We therefore employ a gaseous Helium cooling with high flows in the V-folds, the gap between the two planes in a module and over the module outside. Helium is suitable due to its long scattering length, high mobility and high speed of sound (allowing for large laminar flow speeds). The piping in the frame allows for counter-flowing helium streams in the two V-folds of each strip as well as on the top and bottom of a layer. We have performed extensive computational fluid dynamics simulations of the modules. With flow velocities of the initially 0 °C Helium of 17 m/s in the V-folds and volume flows of 6 L/s in between and on top of the layers, a mean temperature of 49 °C (maximum: 64.5 °C) can be achieved with 400 mW/cm² heating power, see Fig. 61. The MuPix HV-MAPS sensors have been tested at temperatures above 90 °C with only a very moderate amount of additional noise.

5.5.5 Tracker readout

At nominal beam current, the tracker produces in the order of 10 Tbit/s of raw data, more than can be managed by an affordable readout system. We will thus use a gated mode, where the sensors are only active for short time slices.

The HV-MAPS sensors send out zero suppressed hit data (column and row address, time stamp) via a LVDS link with 1.25 Gbit/s. The data are then sent out of the active volume either using radiation resistant LVDS repeaters or multiplexed on radiation hard optical links [113,

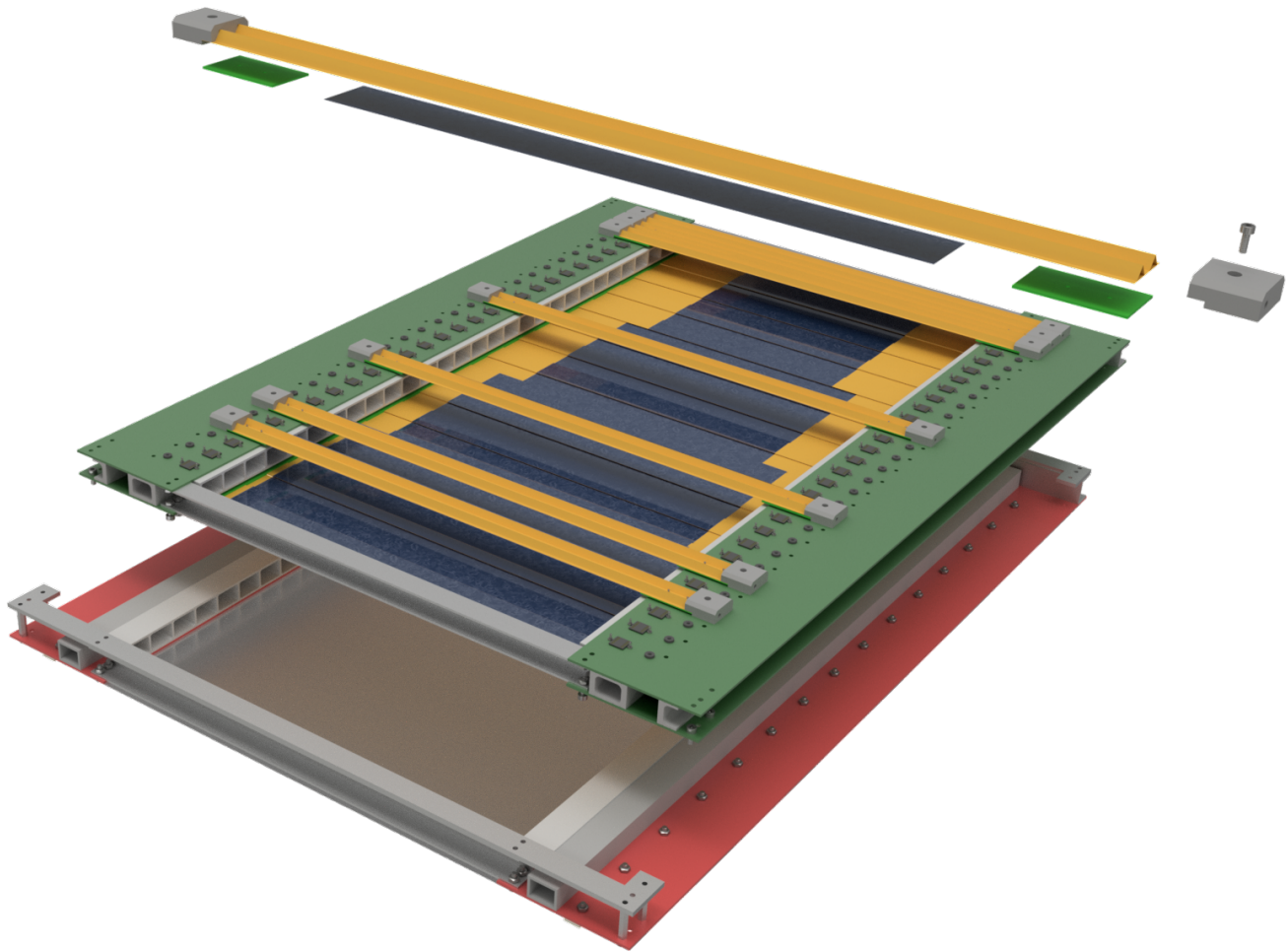


Fig. 60. Rendering of a partially assembled tracker module. On top a single strip assembly is shown with the sensors in blue, the polyimide flexprint with the cooling channel V-folds in yellow, the end PCBs in green and the gas distribution pieces in gray. Below a module with the front cover and most of the front layer strips removed. The PCB/cooling pipe frame with gas distribution is visible, as are the sensors of the back layer. On the bottom is the back cover with its gas distribution.

114, 115]. Both options are currently under study in terms of power and space requirements as well as signal integrity.

Outside of the radiation area, the signals are received by FPGA-based front-end boards. The data streams are synchronized and the hits time-sorted (the MuPix readout scheme introduces some randomization of the time-order of hits). The double plane structure of the tracker is then used to form hit pairs and thus reduce the data rate. These hit pairs are then forwarded to reconstruction PCs, where track finding and fitting is performed. The geometry of the P2 spectrometer and the limited momentum range of the tracks leads to a good locality of the tracking problem, reducing the need for complex data distribution networks.

5.5.6 Track reconstruction

Track finding. The high occupancy of the tracking detectors at the nominal beam current makes track finding in P2 a potentially daunting task. We have developed an algorithm progressing from regions with low-occupancy

to regions with high-occupancy using optimized track-dependent search windows [116] that elegantly manages the combinatorial problems posed. Figure 62 gives a schematic overview of the algorithm, which starts from the two tracking planes furthest away from the target and finds hit pairs consistent with a track from the target. The target constraint and the vector connecting the two hits are then used to define an optimal search window on the second plane of the front module. Matching hits found there are then validated using the front plane. Finally the four hits are subjected to a track fit (see below) and the fit χ^2 is used to accept or reject the track. The performance of the algorithm in reducing the number of candidates reaching the fit state is shown in Fig. 63. The number of wrongly combined tracks (fakes) is highly dependent on the beam rate, see Fig. 64 but even at the full rate, a signal to background ratio above 10 can be achieved at a reasonable efficiency of 85 %.

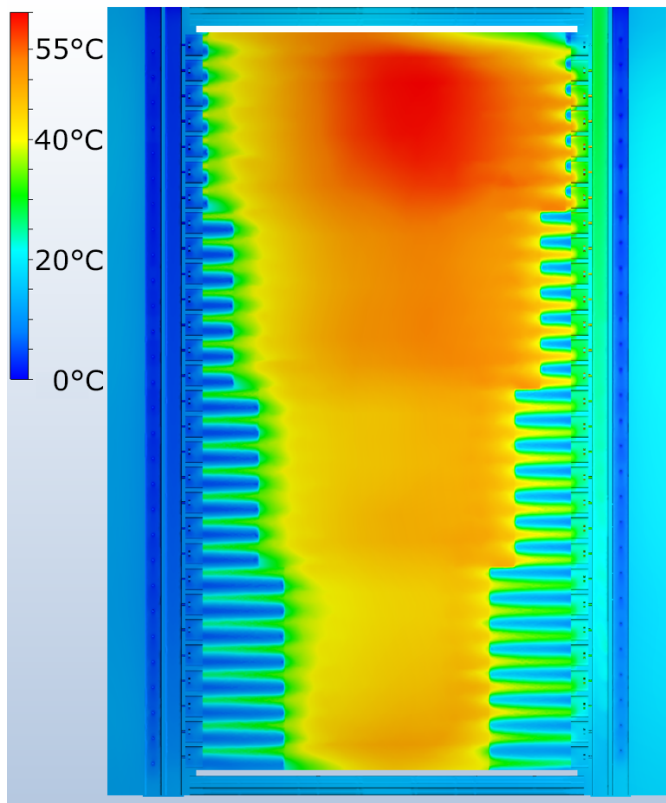


Fig. 61. Computational fluid dynamics simulation of a full tracker module at the maximum power dissipation of the HV-MAPS of 400 mW/cm^2 .

Track fitting. The best precision for the track parameters is obtained using a fit to the measured hit positions. We start by assuming that the track is a helix originating on the beam axis and passing through the centers of gravity of the first two and the last two tracker hits. This rough track, which assumes a constant magnetic field, is then used as a seed in the general broken lines fit [117,118], which takes into account the hit position uncertainty and multiple Coulomb scattering at the two internal planes. The track state is propagated between planes using a Runge-Kutta-Nyström integration of the (inhomogeneous) magnetic field. From four 3D measurements, the fit determines two global track parameters (momentum and polar angle), eight shifts in the measurement planes and four scattering angle projections at the internal planes. The required additional constraints are the zero expectation value of the scattering angle and its variance from multiple scattering theory. In total there are 16 constraints and 14 fit parameters; the resulting track χ^2 can be used to select well reconstructed tracks with little multiple scattering.

The achieved precision for the track parameters is shown in Figs. 65 and 66: the resolution for the track momentum is about $2 \text{ MeV}/c$.

$\langle Q^2 \rangle$ reconstruction. For elastic scattering of a beam of known energy and direction, the momentum transfer can

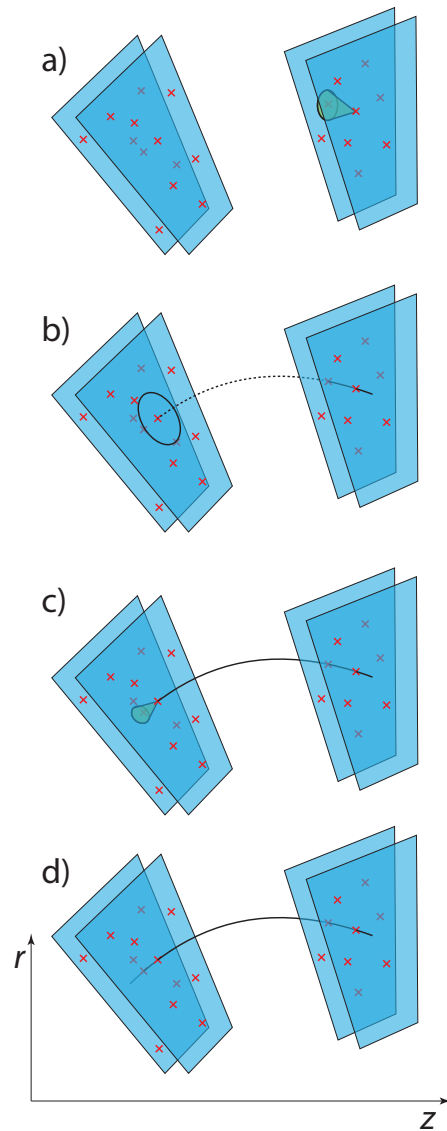


Fig. 62. Schematic overview of the track reconstruction (see text for details). a) forming of hit pairs in the back module, b) extrapolation to the front module, c) validation using the first plane, d) track fit.

be determined from either the scattering angle or the outgoing electron momentum. The very long liquid hydrogen target in P2 however leads to energy losses and small angle scattering of both incoming and outgoing electrons, such that even a very good knowledge of the polar angle and momentum of the electron after leaving the target allows only a very approximate determination of $\langle Q^2 \rangle$. The distributions for energy loss, multiple scattering angles and detector acceptance are highly non-Gaussian and tend to cause biases, which is also the case for the radiative corrections to the large scattering (see Sect. 6.2). The $\langle Q^2 \rangle$ reconstruction does thus have to rely on an iterative procedure using a Monte Carlo simulation including higher-order corrections, where not only the mo-

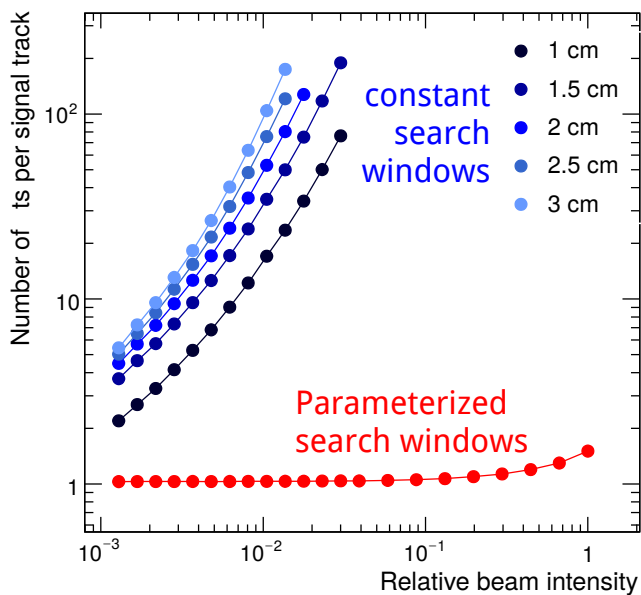


Fig. 63. Number of track candidates as a function of beam intensity (relative to the nominal current of $150\ \mu\text{A}$) using fixed size search windows and the parametrization technique described in the text.

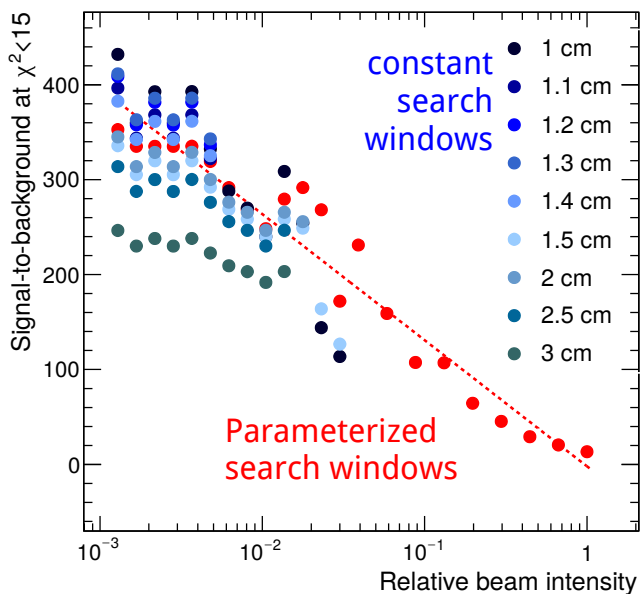


Fig. 64. Signal to background ratio of track finding algorithms depending on beam intensity (relative to the nominal current of $150\ \mu\text{A}$).

momentum and angle distributions, but also the longitudinal and radial position distributions of the point of closest approach need to be reproduced. We are still in the process of developing the respective algorithms and study potential sources of bias; currently we achieve a resolution per track of $3 \times 10^{-4}\ \text{GeV}^2$ (4.3%), see Fig. 67. This allows us to reach the required statistical precision with a few dozen tracks — the $\langle Q^2 \rangle$ measurement will be completely

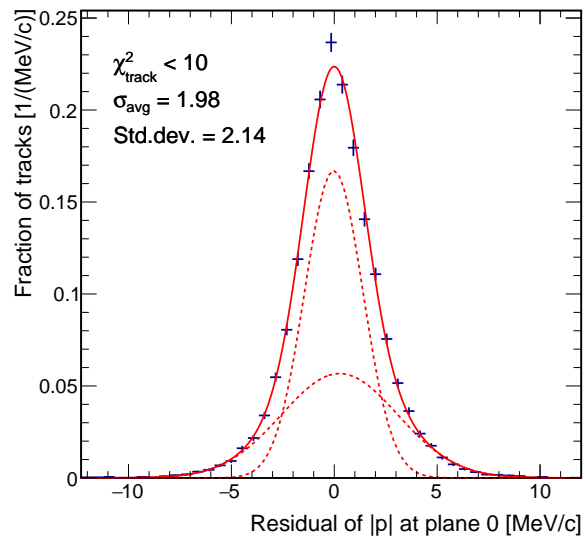


Fig. 65. Reconstructed minus simulated absolute momentum of electron tracks determined at the first tracking plane with requirement on the track fit χ^2 of 10. The fit is the sum of two Gaussians, the resolution σ is the area-weighted mean.

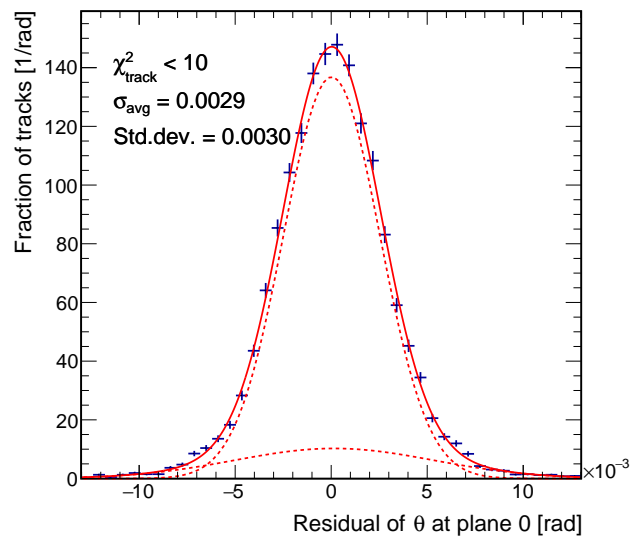


Fig. 66. Reconstructed minus simulated polar angle of electron tracks determined at the first tracking plane with requirement on the track fit χ^2 of 10. The fit is the sum of two Gaussians, the resolution σ is the area-weighted mean.

dominated by systematic uncertainties. We have started studying systematic uncertainties arising due to detector misalignment and estimate them to be much smaller than the required precision of 1% after a track-based alignment. The dominating uncertainty is expected to arise from the MC description of multiple Coulomb scattering and energy loss in the target, which can only be addressed when beam data with the physical target become available. In

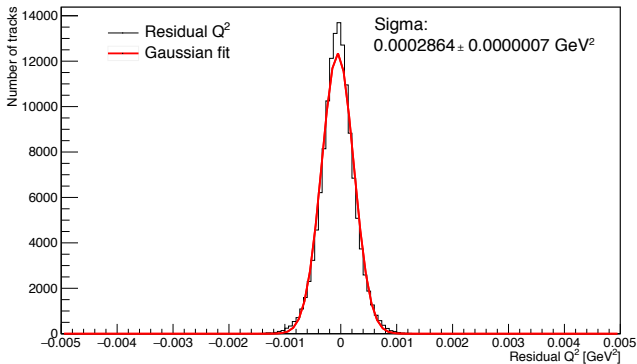


Fig. 67. Reconstructed minus simulated Q^2 for electron tracks as determined with the P2 tracking detector.

the meantime, we will continue our efforts to qualify simulation models using test beam data, see e.g. [119].

6 Theory input

The interpretation of a high-precision measurement of the helicity asymmetry in ep scattering requires theory predictions with uncertainties below those of the experiment. In this section we describe the present status of the corresponding calculations.

To leading order in the electroweak coupling constants, the amplitude \mathcal{M}_{ep}^\pm for elastic scattering of electrons with helicity $\pm 1/2$ is given by the sum of two Feynman diagrams which are due to the exchange of one photon and one Z boson, respectively,

$$\mathcal{M}_{ep}^\pm = \mathcal{M}_\gamma + \mathcal{M}_Z^\pm. \quad (72)$$

While the γ exchange is parity-conserving, the Z exchange contains parity-violating contributions which flip sign depending on the helicity.

At very small elastic momentum transfer Q^2 the internal structure of the proton is not resolved, and the two amplitudes only depend on the proton's electric and weak charges, $e_p = +1$ (in units of the positron charge) and $Q_W(p)$, respectively,

$$\mathcal{M}_{ep}^\pm \sim \frac{1}{Q^2} \mp \frac{Q_W(p)}{16 \sin^2 \theta_W \cos^2 \theta_W} \frac{1}{Q^2 + m_Z^2}, \quad (73)$$

with $m_Z = 91.188(2)$ GeV the mass of the Z boson and θ_W the weak mixing angle. The proton's weak charge at tree-level is related to the weak mixing angle, $Q_W(p) = 1 - 4 \sin^2 \theta_W$.

The parity-violating asymmetry measures the difference between the cross sections for electrons with opposite helicities,

$$A^{\text{PV}} = \frac{|\mathcal{M}_{ep}^+|^2 - |\mathcal{M}_{ep}^-|^2}{|\mathcal{M}_{ep}^+|^2 + |\mathcal{M}_{ep}^-|^2}, \quad (74)$$

and for $Q^2 \ll m_Z^2$ it is a small quantity which arises from the interference of virtual γ and Z exchange. Evaluating this asymmetry using Eq. (73) for very low Q^2 and introducing the Fermi constant

$$G_F = \frac{\pi \alpha_{\text{em}}}{\sqrt{2} m_W^2 \sin^2 \theta_W}, \quad (75)$$

we obtain

$$A^{\text{PV}}(Q^2 \rightarrow 0) = -\frac{G_F Q^2}{4\pi \sqrt{2} \alpha_{\text{em}}} Q_W(p). \quad (76)$$

The direct proportionality between the PV asymmetry and the proton's weak charge constitutes the basis of the P2 experiment.

To match the precision of the experimental measurement of A^{PV} , one has to go beyond the tree-level approximation and include radiative corrections described by Feynman diagrams with loops. They generically scale as $\alpha_{\text{em}}/\pi = O(10^{-3})$, but may be enhanced by logarithms or large numerical factors, as, e.g., in the case of the WW box. Moreover, box diagrams are in general functions of

two kinematical variables, E_i and Q^2 , which requires additional caution when relating the PV asymmetry to the proton's weak charge.

We follow Refs. [120,121] to define the weak charge as

$$Q_W^{1\text{-loop}}(p) = \lim_{E_i \rightarrow 0} \lim_{Q^2 \rightarrow 0} \frac{A^{\text{PV}}}{A_0} \quad (77)$$

with $A_0 = -G_F Q^2 / (4\sqrt{2}\pi\alpha_{\text{em}})$.

The measurement of the PV asymmetry in PVES realized at finite energy E_i and finite momentum transfer Q^2 can be cast in the following form that generalizes Eq. (7) to include one-loop effects,

$$A^{\text{PV}} = A_0 \left[Q_W^{1\text{-loop}}(p) - F(E_i, Q^2) + \Delta_{\square}(E_i, Q^2) - \Delta_{\square}(0, 0) \right], \quad (78)$$

where, for the sake of completeness, we keep the kinematically suppressed term $F(E_i, Q^2)$ introduced earlier in Eq. (7).

The one-loop SM result for $Q_W(p)$ has been formulated in Ref. [122] in the $\overline{\text{MS}}$ scheme, and Eq. (15) is replaced by

$$Q_W^{1\text{-loop}}(p) = (\rho_{nc} + \Delta_e) \left(1 - 4 \sin^2 \hat{\theta}_W(\mu) + \Delta'_e \right) + \Delta_{\square}(0, 0) \quad (79)$$

where $\hat{\theta}_W(\mu)$ is the weak mixing angle defined in the $\overline{\text{MS}}$ scheme at scale μ , where $\mu \simeq 0$ for the P2 experiment. In this equation, the Veltman parameter ρ_{nc} is a universal correction which renormalizes the ratio of the neutral and charged current strengths at low energies. Δ_e and Δ'_e are small, non-universal corrections at the electron vertex. The term Δ_{\square} in Eq. (79) represents the contributions to $Q_W(p)$ from box graphs and is the subject of the next subsection.

The scale dependence of the $\overline{\text{MS}}$ weak mixing angle has been studied in Ref. [123] (see also [124] for a recent update). The value of $\sin^2 \hat{\theta}_W(\mu)$ at low momentum transfer is related by

$$\sin^2 \hat{\theta}_W(0) = \kappa(m_Z) \cdot \sin^2 \hat{\theta}_W(m_Z), \quad (80)$$

to its value at the Z pole (with $\kappa(m_Z) = 1.0317$ for the present values of the SM parameters).

In the $\overline{\text{MS}}$ scheme the scale dependence of the weak mixing angle is determined by the renormalization group evolution of the SM coupling constants. Other definitions of a scale-dependent effective weak mixing angle exist in the literature, see for example [125]. They are based on a redefinition of $\sin \theta_W$ which absorbs universal and partly non-universal one-loop corrections into an effective weak mixing angle $\sin \theta_{W,\text{eff}}$. Figure 68 shows some typical Feynman diagrams contributing to the scale dependence of the effective weak mixing angle.

6.1 Box graph and hadronic uncertainties

The one-loop result of Eqs. (78, 79) singles out the two-boson exchange contributions,

$$\Delta_{\square} \equiv \square_{WW} + \square_{ZZ} + \square_{\gamma Z} + \square_{\gamma\gamma}, \quad (81)$$

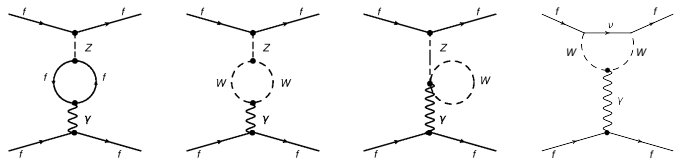


Fig. 68. Feynman graphs of universal and non-universal electroweak corrections which lead to an energy scale dependence of $\sin \theta_{W,\text{eff}}$.

representative Feynman diagrams of which are displayed in Fig. 69. For each box graph, only the real part contributes and \square_{ab} is understood as the real part of the corresponding diagram here and in the following. The box graphs are specific and have to be added as separate contributions since they depend on both the 4-momentum transfer Q^2 and the electron energy. Other one-loop corrections depend on Q^2 only and can therefore be factorized and partly absorbed into universal correction factors as shown above in Eq. (79).

It has been observed in Refs. [126,127,128] that the energy dependence of the heavy-boson box graphs associated with WW and ZZ exchange induces corrections of order $G_F E_i^2$, rather than $\sim \alpha_{\text{em}}/\pi$. For electron energies up to a few GeV these energy-dependent contributions can be safely neglected. The constant terms, however, are numerically large. Since they are dominated by contributions from loop momenta of the order of m_Z , their calculation in the framework of perturbation theory is safe with a reliable uncertainty estimate [122].

The $\gamma\gamma$ box does not contain large logarithms and is known to vanish at small momentum transfer as it can only renormalize the charge radius of the proton but not its charge. Since it only corrects the parity-conserving part of the amplitude, its effect on the PV asymmetry will also be multiplied by the proton's weak charge. All in all, it is natural to expect a correction to A^{PV} of the order of $(\alpha_{\text{em}}/\pi)(Q^2/E_i^2)Q_W(p)$ due to $\gamma\gamma$ -box graphs. This amounts to a negligible correction of order $O(10^{-5})$ for the kinematical conditions at the P2 experiment that can be accommodated in the uncertainty associated with the kinematically suppressed correction term $F(E_i, Q^2)$. With these observations, the energy dependence of the boxes present in Eq. (78) reduces to that of the γZ box,

$$\Delta_{\square}(E_i, Q^2) - \Delta_{\square}(0, 0) = \square_{\gamma Z}(E_i, Q^2) - \square_{\gamma Z}(0, 0). \quad (82)$$

The γZ -box graph contains a large logarithm $\log \frac{m_Z^2}{\Lambda^2}$ where $\Lambda \sim 1 \text{ GeV}$ is a typical hadronic mass scale. The co-

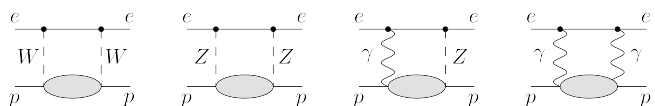


Fig. 69. Electroweak box corrections to parity-violating ep scattering. Shown are, from left to right, WW -, ZZ -, γZ - and $\gamma\gamma$ -exchange diagrams, respectively. Contributions with crossed boson lines are not displayed. The grey blob at the lower part of each diagram denotes inclusive hadronic intermediate states.

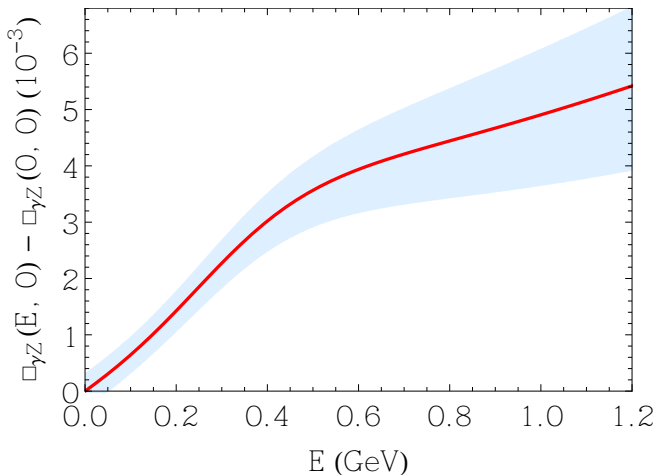


Fig. 70. Energy dependence of the γZ box graph, Eq. (82) at $Q^2 = 0$, and its uncertainty band.

efficient in front of this large logarithm is energy-independent up to corrections $\sim G_F E_i^2$ and can be calculated precisely using quark sum rules [126, 127]. The presence of the hadronic mass scale Λ signals the sensitivity of the γZ box to the hadronic structure, and this sensitivity was used to estimate the hadronic structure-related uncertainty [122]. However, early studies described in the references given above had assumed that the energy dependence of the γZ box was negligible, $\sim G_F E_i^2$, following the pattern of the heavy boson boxes.

Subsequently, the energy dependence of the γZ box was addressed in Ref. [129] in the framework of forward dispersion relations. It was shown that the energy dependence of $\square_{\gamma Z}$ is much more significant than anticipated. It has been the subject of active scrutiny in the theory community [120, 130, 131, 132, 57, 133]. The dispersive method for calculating $\square_{\gamma Z}$ is per se model-independent, relating the γZ box to an integral over measurable unpolarized interference structure functions $F_{1,2,3}^{\gamma Z}$. Nonetheless, due to the lack of reliable experimental data for these structure functions one is forced to introduce model assumptions to define the required input in unmeasured regions. While different groups agree on the central value of $\square_{\gamma Z}(E_i)$ within errors, this model dependence leads to a discrepancy in the uncertainty estimate.

In Fig. 70 the energy dependence of the γZ box is shown. It is obtained as a sum of its vector part $\square_{\gamma Z}^V$ calculated in Ref. [57] and its axial-vector part, $\square_{\gamma Z}^A$ obtained in Ref. [134, 132, 135] at zero momentum transfer. The respective uncertainties are added in quadrature. The extrapolation from the actual value of Q^2 corresponding to the kinematics at P2 down to $Q^2 = 0$ is done according to Ref. [120]. Due to the tiny value of $Q^2 \approx 0.0045$ GeV² this extrapolation leads to a numerically negligible effect, both on the central value and its uncertainty. For the kinematics at P2, the energy-dependent contribution

amounts to

$$\begin{aligned} & \square_{\gamma Z}(E_i = 155 \text{ MeV}, Q^2 = 0) - \square_{\gamma Z}(0, 0) \\ & = (1.06 \pm 0.32) \times 10^{-3} \end{aligned} \quad (83)$$

and the uncertainty is dominated by that due to the effective axial charge of the nucleon seen by charged leptons, also referred to as the anapole moment,

$$\delta \square_{\gamma Z}^A = 0.27 \times 10^{-3}, \quad (84)$$

$$\delta \square_{\gamma Z}^V = 0.18 \times 10^{-3}. \quad (85)$$

A measurement at backward angles as described in section 7.3 will allow to reduce the uncertainty due to the anapole moment considerably, $\delta \square_{\gamma Z}^A \rightarrow 0.07 \times 10^{-3}$. Assuming that this precision goal is achieved, the energy-dependent correction from the γZ box will change to

$$\begin{aligned} & \square_{\gamma Z}(E_i = 155 \text{ MeV}, Q^2 = 0) - \square_{\gamma Z}(0, 0) \\ & = (1.06 \pm 0.19) \times 10^{-3} \end{aligned} \quad (86)$$

with a reduced uncertainty. This estimate was used in Sect. 2, Tab. 2 in the summary of the uncertainty budget.

6.2 QED corrections

Electromagnetic corrections are parity conserving and do not affect the proton's weak charge. However, the relation to the measured helicity asymmetry A^{PV} receives corrections since extra radiated photons lead to a shift of the observed momentum transfer relative to the true one. Q^2 can not be determined from the electron scattering angle alone, but the momentum of unobserved photons has to be taken into account.

The tracking detectors described in Sect. 5.5 will allow one to determine the momentum of the scattered electron, i.e., its energy E_f and the electron scattering angle θ_f . From this information one can determine $Q^2 = -(k - k')^2$ (corresponding to Eq. (6)), where k and k' are the momentum 4-vectors of the initial and final electron. In the presence of bremsstrahlung, a photon with 4-momentum k_γ emitted from the electron will shift Q^2 to the true momentum transfer $Q_{\text{true}}^2 = -(k - k' - k_\gamma)^2$. This true Q^2 value has to be used in the equation relating the measured asymmetry with the proton's weak charge, Eq. (7).

In Fig. 71 we show the average relative shift of Q^2 due to photon radiation including one-photon bremsstrahlung. The Q^2 shift depends strongly on the beam energy and the scattering angle, as well as on a possible cutoff of the energy of photons radiated into the final state. Preliminary results of a calculation including two-photon radiation show that order $O(\alpha^2)$ corrections are much less important. This can be understood since we deal with a kinematic effect: the relation between scattering angle and momentum transfer is not unique anymore in the presence of an additional photon. A second photon does not add considerably more freedom, but only adds corrections of order $O(\alpha^2)$ to the cross section. Eventually, bremsstrahlung effects will be included in the detector simulation.

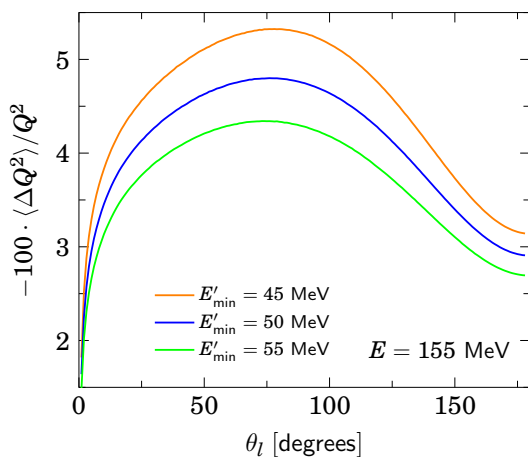


Fig. 71. The average relative shift of the momentum transfer due to photon radiation.

6.3 Theory summary

The current SM prediction for the parity-violating asymmetry in elastic ep scattering, summarized in this section, includes the complete set of NLO corrections. At this order, no further theoretical uncertainties will affect the interpretation of a high-precision measurement of A^{PV} in terms of $\sin^2 \theta_W$ beyond the level of 10^{-4} . In particular, uncertainties from the hadronic structure entering the γZ -box graph at the low energy and small Q^2 values relevant for the P2 experiment are well under control.

A conclusive test of the SM and analyses of the anticipated experimental result at P2 in terms of New Physics can be obtained by comparing with other high-precision determinations of the weak mixing angle from LEP, SLC, and future measurements at the LHC. This will require the inclusion of two-loop electroweak corrections and work on the corresponding NNLO calculations is underway.

7 Further physics programme

7.1 Measurements with Carbon-12

High precision measurements of the weak charges of different particles and nuclei offer complementary sensitivities to physics beyond the Standard Model in the form of new tree level and quantum loop correction parameters. For example, one may consider ratios of polarization asymmetries in which the polarization uncertainty mostly cancels.

Here we summarize the results of first feasibility studies of a measurement of the weak charge of the ^{12}C nucleus with the P2 setup. As a spin-zero nucleus, ^{12}C can be described by a single form factor and is thus theoretically easy to handle [8]. Moreover, its QED cross section is 36 times larger than that of the proton, and its weak charge is 78 times as large, which significantly reduces beam time requirements. The SM prediction for the helicity asymmetry at leading order can be written as in Eq. (7) with

$$Q_W(^{12}\text{C}) = -24 \sin^2 \theta_W. \quad (87)$$

At low momentum transfer $Q^2 \ll M_Z^2$ weak charges can be parametrized with respect to the so-called oblique parameters, such as the S , T and U parameters introduced by Peskin and Takeuchi [136,137]. However, S , T and U are already very precisely determined from Z -pole observables, whereas weak charges are able to constrain some of the higher-order oblique parameters. For example, the X parameter [138] describes the difference of new physics contributions to the γZ mixing at the Z pole and at low energies, and cannot be determined by Z -pole physics alone. Likewise, in the absence of mass mixing, Z -pole observables are virtually blind to extra heavy gauge bosons Z' as new amplitudes are suppressed relative to the Z resonance. By contrast, at low energies Z' amplitudes are merely suppressed by the square of the ratio of the Z and Z' masses. One has [44]

$$\begin{aligned} Q_W(^{12}\text{C}) &= -5.510[1 - 0.003T + 0.016S - 0.033X - \chi], \\ Q_W(\text{p}) &= +0.0707[1 + 0.15T - 0.21S + 0.43X + 4.3\chi], \\ Q_W(\text{e}) &= -0.0435[1 + 0.25T - 0.34S + 0.7X + 7\chi], \\ Q_W(^{133}\text{Cs}) &= -73.24[1 + 0.011S - 0.023X - 0.9\chi] \end{aligned} \quad (88)$$

for the weak charges of ^{12}C , the proton, the electron and ^{133}Cs , and $\chi = M_Z^2/M_{Z_\chi}^2$ was used where Z_χ is the extra Z boson predicted by $SO(10)$ Grand Unified Theories (in the absence of gauge kinetic mixing). The different pre-factors in this parametrization show the complementarity of the different weak charges to physics beyond the Standard Model. Low- Q^2 measurements also have unique sensitivity to certain beyond the Standard Model scenarios such as those involving so-called dark Z bosons [139], which are light (on the order of tens of MeV) and very weakly coupled extra neutral gauge bosons which may mix with the ordinary Z boson, and which may be parametrized by taking X as a function of Q^2 .

One can also discuss the implications of weak charges in a model-independent way. In the effective field theory picture, the Standard Model may be defined by the most general Lagrangian consistent with gauge and Lorentz invariance built from the known particles up to dimension four, while the weak charges probe specific (combinations of) dimension six operators. In photon-interference experiments only vector and axial-vector Lorentz structures are important, and in the elastic regime the nucleus couples vector-like and parity-violation then forces the electron to enter axial-vector-like. Constraints on the quark-vector and electron-axial-vector couplings are illustrated in Fig. 72.

7.1.1 Achievable precision

The achievable precision of $\sin^2 \theta_W$ was determined numerically as described in section 2.2.1. The underlying Eqs. (18) and (19) have been modified appropriately for the case of scattering with a ^{12}C target. The beam energy was varied in the range from 100 MeV to 300 MeV, and we used a beam current of 150 μA , a data taking time of 2500 h, and for detector acceptance angles between 2°

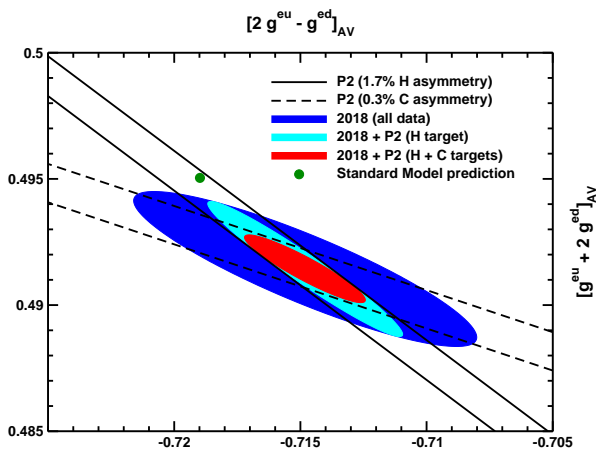


Fig. 72. 1σ constraints on the quark-vector and electron-axial-vector couplings, where the ordinate corresponds to the valence quark combination of the neutron, and the abscissa to the charge weighted sum of the up and down quarks entering the photon-interference term in polarized deep-inelastic scattering (DIS). The solid and dashed lines indicate the constraints of anticipated P2 measurements on hydrogen and carbon, respectively. The blue contour shows the present constraints from atomic parity violation in Cs and Tl, DIS (SLAC and JLab) and the anticipated result of the QWeak experiment [54]. The cyan-colored contour adds the future hydrogen measurement at P2 (assuming the central value remains unchanged), while the red contour includes in addition the possible P2 carbon measurement. The Standard Model prediction is also shown.

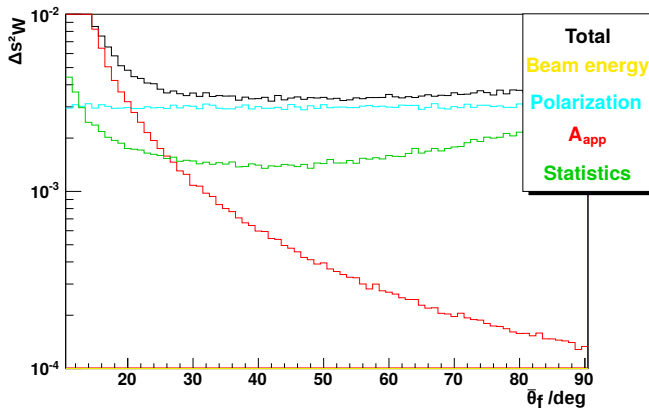


Fig. 73. Monte Carlo determination of the achievable precision in $\sin^2\theta_W$. Example graph for the simulated scattering angle dependence of the relative precision of $\sin^2\theta_W$ at fixed beam energy (150 MeV) and detector acceptance angle (18°).

and 20° . We assumed a beam polarization of 85% with a relative error of 0.3%.

Figure 73 shows the achievable precision for a fixed beam energy of 150 MeV and an acceptance angle of $\delta\theta_f = 18^\circ$ as a function of the average scattering angle $\bar{\theta}_f$. It demonstrates that the total error in $\sin^2\theta_W$ is dominated

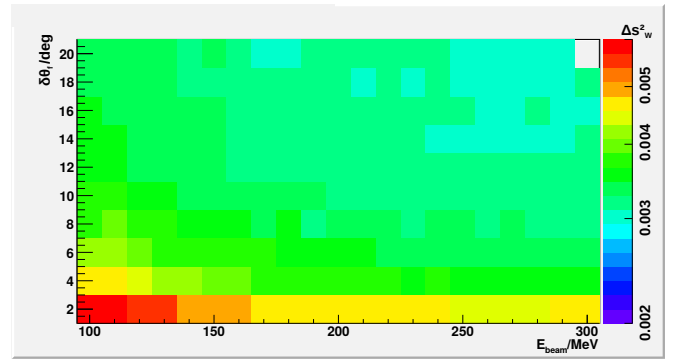


Fig. 74. Monte Carlo determination of the achievable precision in $\sin^2\theta_W$. Best values of $\Delta\sin^2\theta_W$ for a range of beam energies and acceptance angles are shown.

by the contribution of the beam polarization uncertainty (cyan) rather than by the statistical error (green).

Figure 74 summarizes the minimum values for the total error in $\sin^2\theta_W$ for all simulated beam energies and scattering angles. It shows that we can obtain a relative error of 0.3% with high detector acceptance angles and beam energies of 150 MeV. As the weak charge of the ^{12}C nucleus is proportional to $\sin^2\theta_W$, this corresponds to a relative error in the weak charge of ^{12}C of 0.3%.

7.1.2 Experimental setup

For the ^{12}C experiment, the P2 hydrogen target in Fig. 19 can be replaced by a 5-finger graphite target to ensure high luminosities while suppressing double scattering inside the target.

In order to find a suitable spectrometer, detector, and collimator setup, a Geant4 ray tracing study was carried out. Figure 75 shows the distance of the electron trajectories from the beam axis ρ . Such plots were created for a variety of target positions and for spectrometer magnetic fields ranging from 0.1 T to 1 T. When studying the results of the simulation, a setting with which we can place the detector at a focal point of the electrons of interest and with which the undesired background can be collimated was sought. Possible detector and collimator positions are included in Fig. 75.

Furthermore it is crucial to sort out inelastically scattered electrons. The plot in Fig. 76 shows the trajectories from elastically scattered electrons with a beam energy of 200 MeV in red. Trajectories of the electrons that have excited the nucleus to the first and second excited states are shown in blue and yellow, respectively. In these cases, the energy of the electrons is effectively reduced to 196 MeV (for the first excited state) or 185 MeV (for the second excited state). The simulations show that the trajectories are well separated in all cases.

7.1.3 Conclusion

A measurement of the weak charge of the ^{12}C nucleus at MESA can be made with a relative precision of 0.3% as-

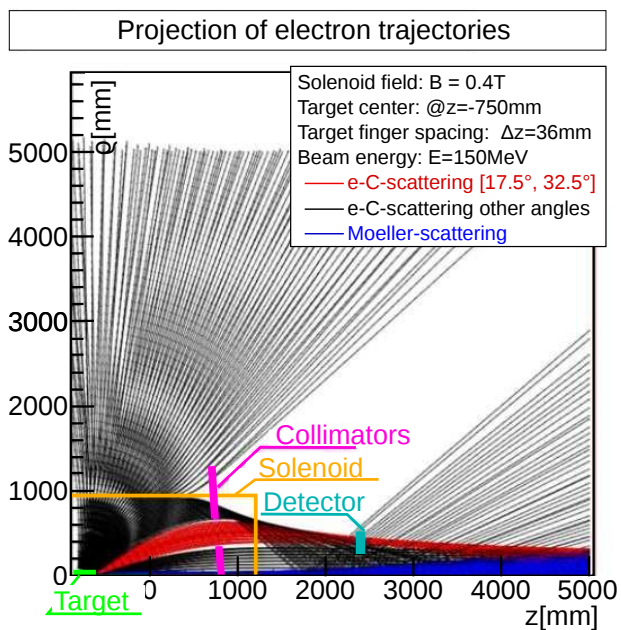


Fig. 75. Geant4 ray tracing plot showing the distance of the electron trajectories from the z -axis. Separation of Møller background (blue) and electrons that were elastically scattered by other angles (black).

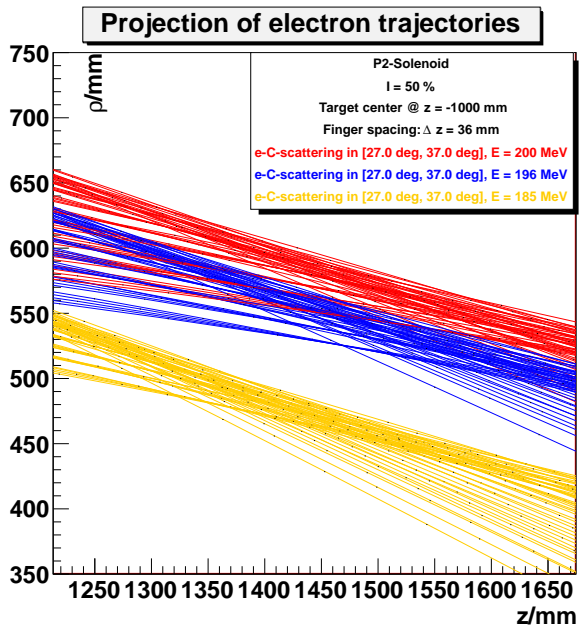


Fig. 76. Magnification of the electron trajectories close to the position of the detector in Fig. 75. Trajectories of electrons scattered off the ^{12}C ground state (red) are separated from those where ^{12}C makes a transition into its first (blue) or second (yellow) excited state.

suming a measurement time of one fourth of that for P2 with a proton target. This corresponds to a precision in the weak mixing angle of 0.3%. The ^{12}C experiment will provide additional and complementary sensitivity to certain classes of new physics models. Furthermore, already individually the carbon and proton measurements by P2 will provide the strongest constraints (95% CL sensitivities of around 50 TeV in strong coupling scenarios [55]) on any CP-allowed four-fermion operator built from first generation fermions. Combined, the operator corresponding to the coupling combination along the minor axis of the red ellipse in Fig. 72 would be probed up to 60 TeV. First conceptual studies regarding the feasibility of the project give promising results.

7.2 Neutron skin measurement

High precision parity-violating electron scattering experiments on nuclei provide a portal to the properties of neutron-rich matter. Unfortunately, it is difficult to study neutron matter directly in the laboratory because the neutron and extremely neutron-rich isotopes are unstable. However, heavy nuclei are expected to develop a neutron-rich skin where many neutrons collect near the surface. Since the parity-violating asymmetry is particularly sensitive to the neutron density, it provides a clean and model independent measurement of the neutron skin of nuclei.

The neutron-skin thickness of a nucleus ΔR_{np} , defined as the difference between the neutron and proton rms-radii is strongly related to the poorly-known symmetry energy at saturation density ρ_0 . The symmetry energy is a key parameter of the nuclear Equation of State (EoS) [140], since it quantifies the changes in nuclear energy associated with modifications of the neutron-proton asymmetry. It determines as well the properties of spectacular astrophysical phenomena such as supernovae explosions or neutron star mergers.

After the first observations of two colliding neutron stars [141], the emergent multi-messengers astronomy field will provide us with new ways to constrain the EoS and the properties of neutron-rich matter. Even stronger constraints can be imposed by combining this information with independent measurements like the precise determination of the neutron-skin thickness of heavy nuclei.

Though intensive experimental effort has been made to determine the neutron-skin thickness, a precise measurement of this quantity remains elusive. Several observables sensitive to the neutron skin have been proposed and recent experiments have been successful in measuring giant- and pygmy-resonance modes [142] on a variety of nuclei as well as the electric-dipole polarizability [143] and coherent pion photoproduction [144]. These data together with data from hadron scattering experiments (involving protons [145], anti-protons [146] and pions [147]) are valuable, but interpretations contain implicit model dependences.

The measurement of parity-violating asymmetries provides a clean and model-independent determination of neutron-skin thicknesses. In Born approximation the parity-violating asymmetry A^{PV} is proportional to the weak form

factor $F_W(Q^2)$,

$$A^{\text{PV}} = \frac{\sigma^+ - \sigma^-}{\sigma^+ + \sigma^-} \approx \frac{G_F Q^2}{4\pi\alpha_{\text{em}}\sqrt{2}} \frac{F_W(Q^2)}{F_{\text{Ch}}(Q^2)}. \quad (89)$$

$F_{\text{Ch}}(Q^2)$ is the Fourier transform of the charge density which is known. A measurement of the parity-violating asymmetry will therefore allow one to determine the weak charge density $F_W(Q^2)$, from which the weak radius

$$R_W^2 = -\frac{6}{F_W(0)} \left. \frac{dF_W}{dQ^2} \right|_{Q^2=0} \quad (90)$$

and thus the neutron radius R_n can be obtained. Taking the known charge radius into account, the neutron-skin thickness can be determined, for details see Refs. [148, 149]. The ^{208}Pb Radius EXperiment (PREX) at JLab has provided the first proof-of-principle of the application of parity-violating electron scattering for the measurement of the neutron-skin thickness [46]. The experiment achieved the systematic error goals of 2% and was a major accomplishment as a first measurement of its kind. However, because of various problems, the experiment took only $\approx 15\%$ of the planned statistics. With all corrections, the measured asymmetry is $A^{\text{PV}} = 0.656 \pm 0.060(\text{stat.}) \pm 0.014(\text{sys.})$ ppm at $Q^2 = 0.00906$ GeV 2 . This corresponds to a value for the neutron skin of ^{208}Pb of $\Delta R_{\text{np}} = (0.33^{+0.16}_{-0.18})$ fm and confirmed the existence of a neutron-radius excess with a 2σ statistical significance.

The P2 experiment will open the window for a new generation of high-precision parity-violating electron-scattering experiments. Within the scope of the P2 experimental setup, the Mainz Radius EXperiment (MREX) will determine the neutron-skin thickness of ^{208}Pb with ultimate precision. Figure 77 shows the expected cross section, parity-violating asymmetry, and sensitivity as well as the resulting figure of merit (FOM) for a beam energy of 155 MeV.

Here, the relevant figure of merit for a neutron skin measurement, for a given energy, is:

$$\text{FOM} \times \varepsilon^2 = \frac{d\sigma}{d\Omega} \times (A^{\text{PV}})^2 \times \varepsilon^2. \quad (91)$$

In addition to the typical FOM for parity-violation experiments, the sensitivity ε of A^{PV} to changes in the neutron radius R_n was taken into account [148]:

$$\varepsilon = \frac{d \ln(A^{\text{PV}})}{d \ln(R_n)} = \frac{R_n}{A^{\text{PV}}} \frac{\delta A^{\text{PV}}}{\delta R_n}. \quad (92)$$

To estimate the best possible achievable precision with MREX, calculations within the peak sensitivity in the polar angular range have been performed using three different settings for the detector acceptance: $\Delta\theta = 2^\circ, 4^\circ$, and 8° . A beam polarization of at least 85% and a systematic uncertainty of 1% in the determination of A^{PV} was taken into account for the calculation. Compared to the given error contribution in Tab. 2, a rather conservative estimation for the size of the systematic uncertainty

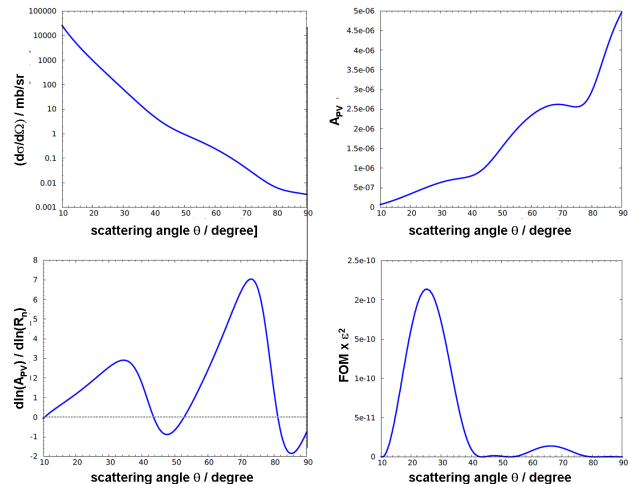


Fig. 77. All plots are for the elastic scattering of electrons off ^{208}Pb at a beam energy of 155 MeV and are based on calculations described in Ref. [150]. Top left: Cross section as a function of the scattering angle θ . Top right: Parity-violating asymmetry A^{PV} as a function of scattering angle θ . Bottom left: Sensitivity ε of the parity-violating asymmetry A^{PV} to changes in the neutron radius R_n as a function of the scattering angle θ . Bottom right: Resulting figure of merit times ε^2 .

| | |
|--------------------------------------|--------------------------|
| Beam energy | 155 MeV |
| Beam current | 150 μA |
| Target density | 0.28 g/cm 2 |
| Polar angle step size | $\Delta\theta = 4^\circ$ |
| Polar angular range | 30° to 34° |
| Degree of polarization | 85 % |
| Parity-violating asymmetry | 0.66 ppm |
| Running time | 1440 hours |
| Systematic uncertainty | 1 % |
| $\delta A^{\text{PV}}/A^{\text{PV}}$ | 1.39 % |
| $\delta R_n/R_n$ | 0.52 % |

Table 15. Kinematical values and general parameters used for the run time estimate.

was used. The best sensitivity was obtained with a detector acceptance of $\Delta\theta = 4^\circ$ in the angular range between 30° and 34° . The running time for the latter one was restricted to 2500 hours to fit the overall beam-time planning of the MESA accelerator. Already after 1500 hours a determination of the neutron radius with a sensitivity of $\delta R_n/R_n = 0.52\%$ can be achieved (see Fig. 78). The main parameters used for the calculation are summarized in Tab. 15.

A crucial requirement for the experiment to correctly measure the parity violating asymmetry is the separation of the ground state of ^{208}Pb from its first excited state ($\Delta E \approx 3$ MeV). Therefore tracking simulations of signal and background particles in the angular range of interest (30° to 34°) have been performed for a solenoid with a magnetic field strength of $B = 0.6$ T. For this study the existing trajectory simulation (see Sect. 5.1.3

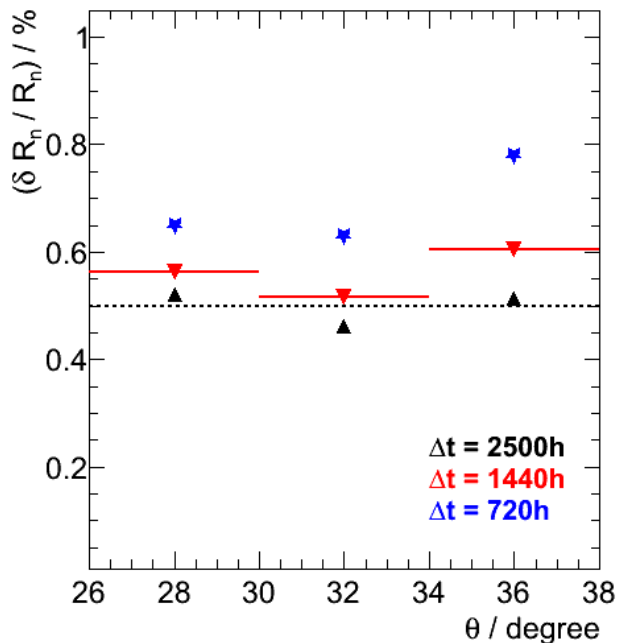


Fig. 78. Running time estimate for a detector acceptance of $\Delta\theta = 4^\circ$ indicated by the width of the horizontal red lines. A systematic error of 1% was included in the calculation.

for details) was adapted and the extended hydrogen target was replaced by a point-like lead target. Trajectories were calculated for the elastically scattered electrons with an energy of 155 MeV as well as for electrons with an energy of 152 MeV, mimicking events from the first excited state of ^{208}Pb . The target position was varied between $z = -2500$ mm and $z = -500$ mm using a step size of 100 mm. With two configurations it was possible to get a clean separation between the elastic and inelastic events. The two options with the target placed at $z = -700$ mm and $z = -2500$ mm are illustrated in Fig. 79 and Fig. 80, respectively.

In both cases it is possible to block the inelastic events with a set of collimators. While both options need the same amount of space behind the solenoid to position the detectors, option II requires additional space in front of the solenoid, adding a further experimental requirement to the changes in the P2 hall. Moreover, option I is similar to the detector configuration intended for the measurement of the weak mixing angle and could allow the use of a combined scattering chamber. This would simplify the structural alteration works during the two experimental campaigns. Implementation of the lead target inside the planned scattering chamber as well as a more detailed Geant4 simulation, including radiative corrections, are currently being performed to finalize the design.

The preliminary results reported here show that a 0.5% measurement ($\delta R_n / R_n$) of the neutron skin thickness of ^{208}Pb using the P2 setup is feasible.

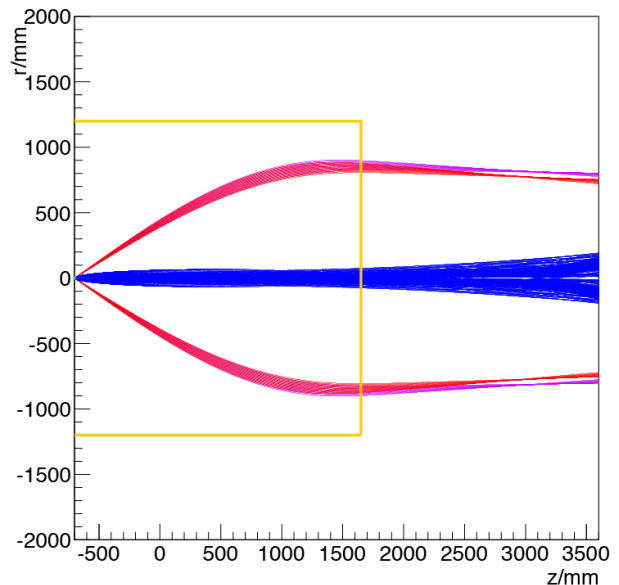


Fig. 79. Detector configuration (option I) determined by the tracking simulation. Electrons originating from the target at $z = -700$ mm with 155 MeV (from elastic scattering on the ^{208}Pb target) are shown in magenta, electrons with 152 MeV (belonging to the first excited state) in red and Møller electrons in blue. The yellow lines represent the dimension of the solenoid.

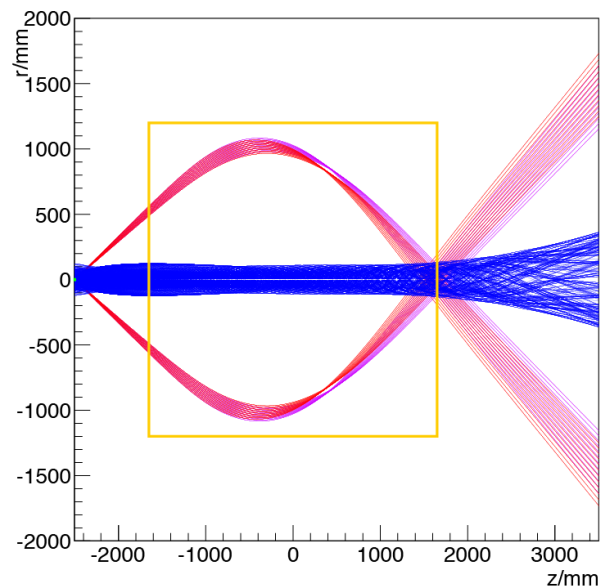


Fig. 80. Detector configuration (option II) determined by the tracking simulation. Electrons originating from the target at $z = -2500$ mm with 155 MeV (from elastic scattering on the ^{208}Pb target) are shown in magenta, electrons with 152 MeV (belonging to the first excited state) in red and Møller electrons in blue. The yellow lines represent the dimension of the solenoid.

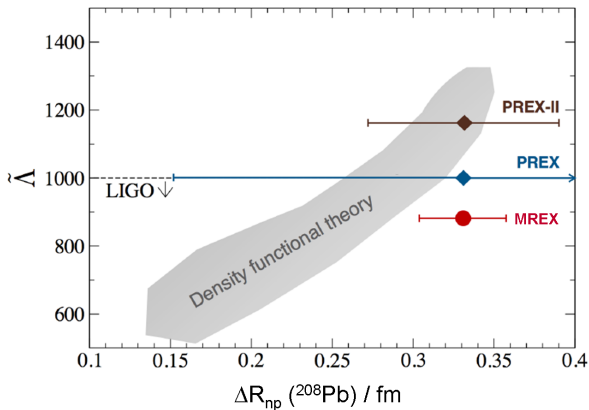


Fig. 81. Constraints provided on density functional theory by combining the tidal deformability parameter $\bar{\lambda}$ of two spiraling neutron stars observed at LIGO [141] with present and future ^{208}Pb neutron skin measurements. Projected precisions of PREX-II [151] and MREX are shown centered at the measured PREX value [46]. Figure: Courtesy of C. J. Horowitz.

Figure 81 shows the predicted MREX sensitivity together with the first calculation of the tidal deformability parameter $\bar{\lambda}$ of two spiraling neutron stars observed by LIGO [141] as a function of the neutron skin thickness of ^{208}Pb within different density functional models. Of course such correlations are only approximate since the neutron skin in ^{208}Pb depends on the EoS at about $0.7\rho_0$, while the radius of a neutron star and its deformability depend on the EoS at about twice the nuclear density. However, in general the higher the pressure at low density the larger the skin and the higher the pressure at higher densities the bigger the deformability. The upper 90% bound observed by LIGO is consistent with rather thin neutron-skin thicknesses. The future PREX-II experiment at JLab [151] with its anticipated precision of 1% together with additional measurement of neutron star mergers at LIGO will clarify the current picture.

Moreover, the improvement in accuracy aimed for by the MREX will provide stringent constraints to such correlation and thus lead to a deeper understanding of neutron-rich matter.

7.3 Backward angle measurement

As seen in Eq. (7), the parity-violating asymmetry A^{PV} depends not only on the weak charge of the proton, but also on its hadronic structure. Since $F(Q^2 = 0) = 0$, a measurement at low momentum transfer $Q^2 \ll 0.1 \text{ GeV}^2$ is mainly sensitive to the weak charge $Q_W(p)$. Nevertheless, for any $Q^2 > 0$ the hadronic contribution cannot be neglected. $F(Q^2)$ can be split up into the three terms $F^{\text{EM}}(Q^2)$, $F^{\text{A}}(Q^2)$ and $F^{\text{S}}(Q^2)$, see Eqs. (8-11). In order to extract the weak charge, the term $F^{\text{EM}}(Q^2)$ does not limit the achievable precision because the electromagnetic form factors are known at sufficiently high precision.

| P2 backward-angle experiment | |
|------------------------------|--|
| Integrated luminosity | $8.7 \cdot 10^7 \text{ fb}^{-1}$ |
| Statistical uncertainty | $\Delta A_{\text{stat}} = 0.03 \text{ ppm}$ |
| False asymmetries | $\Delta A_{\text{HC}} < 0.01 \text{ ppm}$ |
| Polarimetry | $\Delta A_{\text{pol}} = 0.04 \text{ ppm}$ |
| Total uncertainty | $\Delta A_{\text{tot}} = 0.05 \text{ ppm}$ |

Table 16. Performance of a possible P2 backward-angle measurement parallel to the P2 forward experiment. The beam energy used for this calculation is 200 MeV, the Standard Model expectation for the asymmetry is $A^{\text{PV}} \approx 7.5 \text{ ppm}$.

On the other hand, the axial form factor $G_{\text{A}}^{\text{p,Z}}$ and the strange magnetic form factor G_{M}^{s} have relatively large uncertainties such that the terms $F^{\text{A}}(Q^2)$ and $F^{\text{S}}(Q^2)$ make non-negligible contributions to the uncertainty, depending on the scattering angle or the momentum transfer respectively. Therefore we plan a dedicated measurement of these form factors within the P2 experiment. A backward-angle measurement is much more sensitive to G_{M}^{s} and $G_{\text{A}}^{\text{p,Z}}$ compared to a measurement at forward angles. Two different scenarios can be considered: either a backward-angle measurement in parallel to the main forward-angle experiment or dedicated measurements at backward angles alone. The first option depends on the available space in the experimental hall as well as on the availability of additional detectors, readout etc. The second option would require additional beam time in the order of 2.000 hours.

A backward-angle measurement parallel to the main experiment could be done in principle for the whole experiment time, i.e., 10 000 hours. The beam energy used for the following discussion is 200 MeV. The backward detector covers polar and azimuthal scattering angles of $140^\circ \leq \theta \leq 150^\circ$ and $0 \leq \phi \leq 2\pi$, the momentum transfer is $Q^2 = 0.1 \text{ GeV}^2$. Table 16 shows what could be achieved with such a P2 backward-angle measurement. One can see that the asymmetry could be measured to a precision at the sub-percent level with the beam polarization as the main source of uncertainty. From this asymmetry, one can derive a value for the linear combination:

$$F^{\text{S}} + F^{\text{A}} = 0.398 \cdot \left(G_{\text{M}}^{\text{s}} + 0.442 G_{\text{A}}^{\text{p,Z}} \right) \pm 0.011. \quad (93)$$

Here, the form factor input $F_{\text{EM}} = 0.558 \pm 0.010$ is the predominant source of uncertainty. For the P2 forward measurement, one needs as input the linear combination $F^{\text{S}} + F^{\text{A}} = 0.0040 \cdot (G_{\text{M}}^{\text{s}} + 0.691 G_{\text{A}}^{\text{p,Z}})$. If one scales down the linear combination from the backward-angle measurement to the P2 forward conditions, one has to keep in mind that the linear combinations are slightly different and the momentum transfers do not match exactly. Therefore we add an additional error for this transformation of 100% of the error of the measured linear combination. The benefit of the backward-angle measurement can be clearly seen: The uncertainty which is used as an input to the P2 main experiment analysis drops from $\Delta(F^{\text{S}} + F^{\text{A}}) = 0.00076$ if no backward-angle measurement is performed down to $\Delta(F^{\text{S}} + F^{\text{A}}) = 0.00016$ using the results of the backward-

angle measurement. This would mean an improvement by a factor of 4.

We also considered two dedicated backward-angle measurements with 1000 hours of data taking each using a hydrogen and a deuterium target. The beam energy for this calculation is $E = 150$ MeV, which corresponds to a momentum transfer of $Q^2 = 0.06$ GeV². Combining hydrogen and deuterium results, one could obtain G_M^s and $G_A^{p,Z}$ separately, which is a valuable physics result by itself. In order to estimate the achievable precision

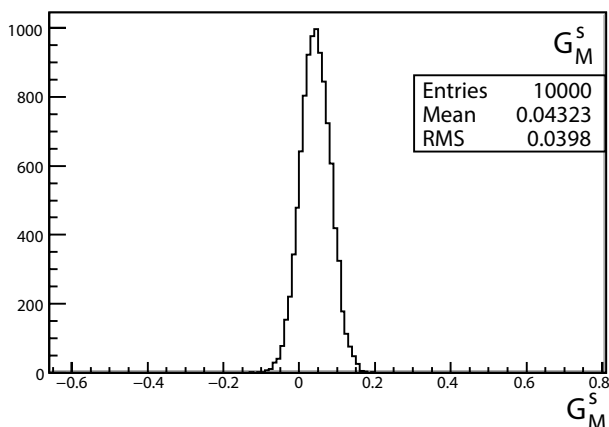


Fig. 82. Values for G_M^s from dedicated backward-angle measurements with a hydrogen and a deuterium target.

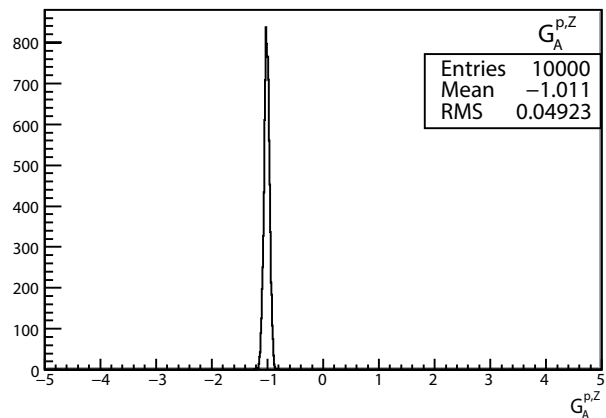


Fig. 83. Values for $G_A^{p,Z}$ from dedicated backward-angle measurements with a hydrogen and a deuterium target.

in G_M^s and $G_A^{p,Z}$, all quantities that enter into their determination were varied according to their uncertainties. The width of the distributions are displayed in Fig. 82 and Fig. 83. It turns out that the possible uncertainties would be $\Delta G_M^s = 0.04$ and $\Delta G_A^{p,Z} = 0.05$. The impact on the forward P2 experiment would be even better compared to a parallel backward-angle measurement, because the momentum transfer would match better and the re-

quired linear combination can be calculated directly from the separated form factors.

To conclude, backward-angle measurements within the P2 experiment seem promising. Two options were discussed. A backward-angle measurement parallel to the forward P2 experiment doesn't require additional beam time, but depends on the available space in the experimental hall. The uncertainty contribution of axial and strange magnetic form factors, expressed by $F^S + F^A$ would drop by a factor of 4 compared to the assumptions without such a measurement. Separate measurements on hydrogen and deuterium targets seem even more promising and would yield the most precise determination of G_M^s and $G_A^{p,Z}$ at low momentum transfer.

8 Conclusions and Outlook

This work summarizes the research and development work for the P2 experimental facility at the upcoming energy recovering recirculating accelerator MESA in Mainz. It is optimized for the measurement of an order 10^{-8} parity-violating cross section asymmetry in electron scattering. This is the smallest asymmetry ever measured in electron scattering. Many new experimental techniques will be used for the first time in order to reach the high precision goal needed to obtain physics results with a high impact on the field of research. These are:

- a superconducting solenoid as a spectrometer for scattered electrons;
- HVMAPS as thin silicon tracking detectors for the Q^2 measurement;
- a so called Hydro-Møller polarimeter, a magnetic trap for Møller scattering off atomic hydrogen;
- a low energy recirculating accelerator with low number of recirculations and energy recovery capability.

The P2 experimental facility has a rich program covering different fields like particle physics and nuclear physics. The building hosting the MESA accelerator will be finished according to the present construction plan in mid of 2020. The start of the accelerator and experiment commissioning is foreseen mid of the year 2021. A detailed beam-time plan for the experimental program has not yet been set up. This needs to be discussed in order to achieve a good compromise between commissioning of MESA and P2 and the high demands of the parity-violation program. Ideally, one would run experiments with large asymmetries and short measurement times first in order to meet the increasing demands of the experiments in parallel to the performance increase achieved by careful commissioning of accelerator, beam control systems, polarimetry and experimental setup. The present physics topics of P2 identified as topics with a high impact on the respective research fields, are:

- Measurement of the weak charge of the proton for the determination of the weak mixing angle $\sin^2 \theta_W$ with an accuracy of 0.14%. The expected asymmetry is $\langle A^{\text{exp}} \rangle_{\text{Cherenkov}} = -28.77$ ppb, averaged over cross

section and acceptance. The necessary measurement time is 10 000 h. This is the most demanding measurement due to the small size of the asymmetry and the long measurement time. The target accuracy will go beyond the present state of the art by a factor three, corresponding to a factor of 10 higher statistics and a factor of three higher in all beam-related apparatus asymmetries, and polarimetry on the level of 0.5%. It has a sensitivity for new physics beyond the standard model with mass scales ranging from 70 MeV up to 50 TeV and complementary to the new physics searches at the LHC.

- Measurement of the weak charge of the ^{12}C nucleus. The asymmetry is of order 3 ppm due to the large weak charge of the neutrons in ^{12}C and the measurement would need about 2500 h. The precision goal of 0.3% is a challenge for polarimetry and requires additional research and development work. In combination with the measurement of the weak charge one can reach a still higher sensitivity for new physics of mass scales up to about 60 TeV.
- Measurement of the neutron skin of the ^{208}Pb nucleus. The asymmetry is of order 3 ppm and the measurement would need about 1500 h. The result is expected to yield an error on the neutron radius of $\delta R_n/R_n$ of 0.52%. Such a measurement will be important for a better understanding of the physics of neutron stars.
- A backward-angle measurement of the parity-violating elastic scattering to measure the weak form factor of the nucleon. From measurements with hydrogen and deuterium targets, the error bars for G_M^s and $G_A^{p,Z}$ can be reduced substantially.

The experimental program described in this manuscript comprises several years of pure data taking, calibration and the study of systematic effects like a parity-violating asymmetry from the aluminum windows. Together with the beam-time demand from the second MESA flagship facility MAGIX, one can safely say that we are facing 6 to 10 years of a research program at MESA.

Technically, the beam energy of MESA could be increased up to 200 MeV. The discussion of a possible research program for this enhanced MESA setup is ongoing. It would bring the pion-production threshold, both for scattering off protons and for heavier nuclei, into the reach of the experimental facilities at MESA. In particular the study of hadronic parity violation which has seen enormous progress in the theory sector over the last years will be interesting [152, 153].

At energies above the pion production threshold, it is possible to directly address hadronic parity violation effects, in particular the parity-violating πN coupling constant $h_{\pi NN}^1$. As pointed out in Refs. [154, 155] these effects become prominent in the near-threshold charged pion production with a polarized electron beam and with only the charged pion in the final state detected. The origin of this parity-violating coupling lies in the effective four-quark operators which are also responsible for generating the anapole moment. The anapole moment is the source of the largest uncertainty in the upcoming P2 experiment.

Furthermore, measuring the parity-violating asymmetry in inelastic electron scattering between the pion production threshold and the $\Delta(1232)$ resonance, as argued in Ref. [57], offers an enhanced sensitivity to strange form factors of the nucleon.

Finally, the increased energy reach of MESA with a polarized beam would make it possible to perform a new measurement of the parity-conserving, beam normal spin asymmetry in elastic ep scattering at backward angles. This observable is a single-spin asymmetry with the electron polarization normal to the scattering plane. It is a purely electromagnetic effect which contributes an important systematic uncertainty to parity-violating electron scattering. The earlier measurement at 200 MeV and 150° at MIT-Bates [12] are not fully understood: the observed large asymmetry is at variance with the much smaller theory expectation [156] which is, at this energy, essentially free of uncertainties.

The upcoming new Mainz P2 experimental facility will bring very interesting times in the measurement of parity violating electron scattering.

9 Acknowledgements

This work is supported by the Deutsche Forschungsgemeinschaft (DFG) in the framework of the collaborative research center SFB1044 “The Low-Energy Frontier of the Standard Model: From Quarks and Gluons to Hadrons and Nuclei”, and in the framework of the PRISMA cluster of excellence “Precision Physics, Fundamental Interactions and structure of Matter”. Silviu Covrig acknowledges support by an Early Career Award from the DOE. Jens Erler acknowledges support in part by the German-Mexican research collaboration grant 278017 (CONACyT) and SP 778/4-1 (DFG), as well as by CONACyT project 252167-F. Michael Gericke is partially supported by funding received through the Natural Sciences and Engineering Research Council of Canada (NSERC) and the Canadian Foundation for Innovation (CFI). Mikhail Gorchtein acknowledges support by the DFG under the personal grant GO 2604/2-1. Boxing Gou would like to thank the Office of China Postdoctoral Council (OCPC) for financial support. The P2 tracker group would like to thank the Mu3e group in Heidelberg, in particular Frank Meier-Aeschbacher and Dirk Wiedner for many helpful discussions. This work comprises part of the Phd thesis work of Dominik Becker, Razvan Bucoveanu, Carsten Grzesik, Ruth Kempf, Kathrin Imai, Matthias Molitor, Alexey Tyukin, and Marco Zimmermann.

A Nucleon form factor fit parameters

It has been assumed in Eq. (21) that the nucleon form factors can be parametrized as functions $F(\{\kappa_l\}, Q^2)$, where $\{\kappa_l\}$ is a set of independent, real parameters. The parametrizations used are described in Sect. 2.2.2. Here we

present the expected values $\langle \kappa_l \rangle$ and standard deviations $\Delta \kappa_l$ of the parameters κ_l , which have been used in the error propagation calculations.

| i | $\kappa_i^E/(\text{GeV}/c)^{-2i}$ | $\Delta \kappa_i^E/(\text{GeV}/c)^{-2i}$ |
|---|-----------------------------------|--|
| 1 | $-4.701\,987 \times 10^{-1}$ | $1.133\,586 \times 10^{-2}$ |
| 2 | 4.342 292 | $6.849\,265 \times 10^{-2}$ |
| 3 | $-2.068\,202 \times 10^1$ | $1.718\,847 \times 10^{-1}$ |
| 4 | $4.406\,141 \times 10^1$ | $3.152\,484 \times 10^{-1}$ |
| 5 | $-2.474\,794 \times 10^1$ | $5.080\,538 \times 10^{-1}$ |
| 6 | $-5.087\,120 \times 10^1$ | $7.708\,359 \times 10^{-1}$ |
| 7 | $8.101\,379 \times 10^1$ | 1.055 087 |
| 8 | $-3.302\,248 \times 10^1$ | 1.047 902 |

Table 17. Parameter values used to parametrize $G_E^{p,\gamma}$.

| i | $\kappa_i^M/(\text{GeV}/c)^{-2i}$ | $\Delta \kappa_i^M/(\text{GeV}/c)^{-2i}$ |
|---|-----------------------------------|--|
| 1 | $2.445\,791 \times 10^{-1}$ | $1.285\,954 \times 10^{-2}$ |
| 2 | -4.387 620 | $4.832\,165 \times 10^{-2}$ |
| 3 | $2.244\,408 \times 10^1$ | $8.019\,477 \times 10^{-2}$ |
| 4 | $-4.477\,354 \times 10^1$ | $1.120\,105 \times 10^{-1}$ |
| 5 | $2.507\,312 \times 10^1$ | $1.455\,939 \times 10^{-1}$ |
| 6 | $3.475\,912 \times 10^1$ | $1.827\,526 \times 10^{-1}$ |
| 7 | $-5.305\,466 \times 10^1$ | $2.105\,056 \times 10^{-1}$ |
| 8 | $1.976\,824 \times 10^1$ | $1.874\,455 \times 10^{-1}$ |

Table 18. Parameter values used to parametrize $G_M^{p,\gamma}$.

| i | κ_i | $\Delta \kappa_i$ |
|---|------------|-----------------------------|
| 1 | 1.770 221 | $1.454\,643 \times 10^{-2}$ |
| 2 | 3.425 350 | $2.075\,773 \times 10^{-1}$ |

Table 19. Parameter values used to parametrize $G_E^{n,\gamma}$.

| i | $\kappa_i/(\text{GeV}/c)^{-2i}$ | $\Delta \kappa_i/(\text{GeV}/c)^{-2i}$ |
|---|---------------------------------|--|
| 0 | -1.916 029 | $4.589\,687 \times 10^{-4}$ |
| 1 | 7.092 145 | $3.229\,584 \times 10^{-2}$ |
| 2 | $-3.329\,785 \times 10^1$ | $1.602\,581 \times 10^{-1}$ |
| 3 | $1.574\,668 \times 10^2$ | $4.007\,755 \times 10^{-1}$ |
| 4 | $-4.144\,474 \times 10^2$ | $9.176\,047 \times 10^{-1}$ |
| 5 | $1.627\,159 \times 10^2$ | 2.025 616 |
| 6 | $1.152\,293 \times 10^3$ | 4.366 665 |
| 7 | $-2.117\,386 \times 10^2$ | 9.120 974 |
| 8 | $-4.908\,379 \times 10^3$ | $1.819\,254 \times 10^1$ |
| 9 | $5.114\,440 \times 10^3$ | $3.374\,769 \times 10^1$ |

Table 20. Parameter values used to parametrize $G_M^{n,\gamma}$.

| i | κ_i | $\Delta \kappa_i$ |
|---|-----------------------------|-----------------------------|
| 1 | $3.231\,461 \times 10^{-1}$ | $8.871\,228 \times 10^{-1}$ |
| 2 | 4.704 640 | $3.000\,726 \times 10^1$ |

Table 21. Parameter values used to parametrize G_E^s .

| i | $\kappa_i/(\text{GeV}/c)^{-2i}$ | $\Delta \kappa_i/(\text{GeV}/c)^{-2i}$ |
|---|---------------------------------|--|
| 0 | $4.411\,866 \times 10^{-2}$ | $1.393\,027 \times 10^{-1}$ |
| 1 | $9.312\,301 \times 10^{-1}$ | 1.016 812 |

Table 22. Parameter values used to parametrize G_M^s .

| i | $\kappa_i/(\text{GeV}/c)^i$ | $\Delta \kappa_i/(\text{GeV}/c)^i$ |
|---|-----------------------------|------------------------------------|
| 0 | -1.136 | 0.411 |
| 1 | 1.032 | 0.036 |

Table 23. Parameter values used to parametrize $G_A^{p,Z}$.

| i | $\kappa_i^E/(\text{GeV}/c)^{-2i}$ | $\Delta\kappa_i^E/(\text{GeV}/c)^{-2i}$ |
|---|-----------------------------------|---|
| 0 | $1.344\,573 \times 10^{-13}$ | $1.000\,000 \times 10^{-7}$ |
| 1 | $5.669\,833 \times 10^{-2}$ | $2.772\,295 \times 10^{-2}$ |
| 2 | $-2.465\,694 \times 10^{-1}$ | $6.866\,436 \times 10^{-1}$ |
| 3 | $5.813\,392 \times 10^{-1}$ | 4.856 379 |
| 4 | $-7.002\,228 \times 10^{-1}$ | $1.023\,000 \times 10^1$ |

Table 24. Parameter values used to parametrize G_E^{rud} .

| i | $\kappa_i^M/(\text{GeV}/c)^{-2i}$ | $\Delta\kappa_i^M/(\text{GeV}/c)^{-2i}$ |
|---|-----------------------------------|---|
| 0 | $2.474\,684 \times 10^{-2}$ | $1.824\,655 \times 10^{-2}$ |
| 1 | $6.787\,448 \times 10^{-2}$ | $7.769\,135 \times 10^{-1}$ |
| 2 | $-3.042\,028 \times 10^{-2}$ | $1.003\,967 \times 10^1$ |
| 3 | $-4.367\,643 \times 10^{-1}$ | $4.767\,653 \times 10^1$ |
| 4 | $8.468\,409 \times 10^{-1}$ | $7.470\,339 \times 10^1$ |

Table 25. Parameter values used to parametrize G_M^{rud} .

References

1. T. D. Lee and C.-N. Yang, “*Question of Parity Conservation in Weak Interactions*”, Phys. Rev., **104** 254–258, 1956.
2. C. S. Wu, E. Ambler, R. W. Hayward, D. D. Hoppes and R. P. Hudson, “*Experimental Test of Parity Conservation in Beta Decay*”, Phys. Rev., **105** 1413–1414, 1957.
3. R. L. Garwin, L. M. Lederman and Marcel Weinrich, “*Observations of the Failure of Conservation of Parity and Charge Conjugation in Meson Decays: The Magnetic Moment of the Free Muon*”, Phys. Rev., **105** 1415–1417, 1957.
4. Ya. B. Zeldovich, “*Parity nonconservation in the first order in the weak interaction constant in electron scattering and other effects*”, Sov. Phys. JETP, **36** 964, 1959.
5. C. Y. Prescott et al., “*Parity Nonconservation in Inelastic Electron Scattering*”, Phys. Lett., **B77** 347–352, 1978.
6. M. A. Bouchiat, J. Guena, L. Hunter and L. Pottier, “*Observation of a Parity Violation in Cesium*”, Phys. Lett., **117B** 358, 1982, [Erratum: Phys. Lett.121B,456(1983)].
7. W. Heil et al., “*Improved Limits on the Weak, Neutral, Hadronic Axial Vector Coupling Constants From Quasielastic Scattering of Polarized Electrons*”, Nucl. Phys., **B327** 1–31, 1989.
8. P. A. Souder et al., “*Measurement of parity violation in the elastic scattering of polarized electrons from C-12*”, Phys. Rev. Lett., **65** 694–697, 1990.
9. D. B. Kaplan and A. Manohar, “*Strange Matrix Elements in the Proton from Neutral Current Experiments*”, Nucl. Phys., **B310** 527–547, 1988.
10. B. Mueller et al., [SAMPLE], “*Measurement of the proton’s neutral weak magnetic form-factor*”, Phys. Rev. Lett., **78** 3824–3827, 1997, (arXiv:nucl-ex/9702004).
11. D. T. Spayde et al., [SAMPLE], “*Parity violation in elastic electron proton scattering and the proton’s strange magnetic form-factor*”, Phys. Rev. Lett., **84** 1106–1109, 2000, (arXiv:nucl-ex/9909010).
12. S. P. Wells et al., [SAMPLE], “*Measurement of the vector analyzing power in elastic electron proton scattering as a probe of double photon exchange amplitudes*”, Phys. Rev., **C63** 064001, 2001, (arXiv:nucl-ex/0002010).
13. R. Hasty et al., [SAMPLE], “*Strange magnetism and the anapole structure of the proton*”, Science, **290** 2117, 2000, (arXiv:nucl-ex/0102001).
14. D. T. Spayde et al., [SAMPLE], “*The Strange quark contribution to the proton’s magnetic moment*”, Phys. Lett., **B583** 79–86, 2004, (arXiv:nucl-ex/0312016).
15. T. M. Ito et al., [SAMPLE], “*Parity violating electron deuteron scattering and the proton’s neutral weak axial vector form-factor*”, Phys. Rev. Lett., **92** 102003, 2004, (arXiv:nucl-ex/0310001).
16. F. E. Maas et al., [A4], “*Measurement of strange quark contributions to the nucleon’s form-factors at $Q^2 = 0.230 (\text{GeV}/c)^2$* ”, Phys. Rev. Lett., **93** 022002, 2004, (arXiv:nucl-ex/0401019).
17. S. Baunack et al., [A4], “*Realtime calibration of the A4 electromagnetic lead fluoride calorimeter*”, Nucl. Instrum. Meth., **A640** 58–68, 2011, (arXiv:1102.5640 [nucl-ex]).
18. P. Achenbach et al., “*Radiation resistance and optical properties of lead fluoride Cherenkov crystals*”, Nucl. Instrum. Meth., **A416** 357–363, 1998.
19. P. Achenbach, S. Baunack, K. Grimm, T. Hammel, D. von Harrach, A. Lopes-Ginja, F. E. Maas, E. Schilling and H. Stroher, “*Measurements and simulations of Cherenkov light in lead fluoride crystals*”, Nucl. Instrum. Meth., **A465** 318–328, 2001, (arXiv:nucl-ex/0108019).
20. F. E. Maas et al., “*Measurement of the transverse beam spin asymmetry in elastic electron proton scattering and the inelastic contribution to the imaginary part of the two-photon exchange amplitude*”, Phys. Rev. Lett., **94** 082001, 2005, (arXiv:nucl-ex/0410013).
21. F. E. Maas et al., “*Evidence for strange quark contributions to the nucleon’s form-factors at $q^{*2} = 0.108 (\text{GeV}/c)^{*2}$* ”, Phys. Rev. Lett., **94** 152001, 2005, (arXiv:nucl-ex/0412030).
22. T. Hammel et al., “*A Luminosity monitor for the A4 parity violation experiment at MAMI*”, Nucl. Instrum. Meth., **A564** 1–12, 2006, (arXiv:nucl-ex/0504017).
23. I. Altarev et al., “*A High power liquid hydrogen target for the Mainz A4 parity violation experiment*”, Nucl. Instrum. Meth., **A564** 13–25, 2006, (arXiv:nucl-ex/0504024).
24. S. Baunack et al., “*Measurement of Strange Quark Contributions to the Vector Form Factors of the Proton at $Q^2=0.22 (\text{GeV}/c)^2$* ”, Phys. Rev. Lett., **102** 151803, 2009, (arXiv:0903.2733 [nucl-ex]).
25. D. Balaguer Ros et al., “*Measurement of the parity violating asymmetry in the quasielastic electron-deuteron scattering and improved determination of the magnetic strange form factor and the isovector anapole radiative correction*”, Phys. Rev., **D94**(5) 051101, 2016.
26. D. Balaguer Ros et al., “*New Measurements of the Beam Normal Spin Asymmetries at Large Backward Angles with Hydrogen and Deuterium Targets*”, Phys. Rev. Lett., **119**(1) 012501, 2017.
27. K. A. Aniol et al., [HAPPEX], “*Measurement of the neutral weak form-factors of the proton*”, Phys. Rev. Lett., **82** 1096–1100, 1999, (arXiv:nucl-ex/9810012).

28. N. Falletto et al., [HAPPEX], “Compton scattering off polarized electrons with a high finesse Fabry-Perot cavity at JLab”, Nucl. Instrum. Meth., **A459** 412–425, 2001.
29. K. A. Aniol et al., [HAPPEX], “New measurement of parity violation in elastic electron - proton scattering and implications for strange form-factors”, Phys. Lett., **B509** 211–216, 2001, (arXiv:nucl-ex/0006002).
30. K. A. Aniol et al., [HAPPEX], “Parity violating electroweak asymmetry in polarized-e p scattering”, Phys. Rev., **C69** 065501, 2004, (arXiv:nucl-ex/0402004).
31. K. A. Aniol et al., [HAPPEX], “Parity-violating electron scattering from He-4 and the strange electric form-factor of the nucleon”, Phys. Rev. Lett., **96** 022003, 2006, (arXiv:nucl-ex/0506010).
32. K. A. Aniol et al., [HAPPEX], “Constraints on the nucleon strange form-factors at $Q^{*2} = 0.1-1 \text{ GeV}^{*2}$ ”, Phys. Lett., **B635** 275–279, 2006, (arXiv:nucl-ex/0506011).
33. A. Acha et al., [HAPPEX], “Precision Measurements of the Nucleon Strange Form Factors at $Q^2 \sim 0.1 \text{ GeV}^2$ ”, Phys. Rev. Lett., **98** 032301, 2007, (arXiv:nucl-ex/0609002).
34. Z. Ahmed et al., [HAPPEX], “New Precision Limit on the Strange Vector Form Factors of the Proton”, Phys. Rev. Lett., **108** 102001, 2012, (arXiv:1107.0913 [nucl-ex]).
35. D. S. Armstrong et al., [G0], “Strange quark contributions to parity-violating asymmetries in the forward $G0$ electron-proton scattering experiment”, Phys. Rev. Lett., **95** 092001, 2005, (arXiv:nucl-ex/0506021).
36. David S. Armstrong et al., [G0], “Transverse Beam Spin Asymmetries in Forward-Angle Elastic Electron-Proton Scattering”, Phys. Rev. Lett., **99** 092301, 2007, (arXiv:0705.1525 [nucl-ex]).
37. D. Androic et al., [G0], “Strange Quark Contributions to Parity-Violating Asymmetries in the Backward Angle $G0$ Electron Scattering Experiment”, Phys. Rev. Lett., **104** 012001, 2010, (arXiv:0909.5107 [nucl-ex]).
38. D. Androic et al., [G0], “The $G0$ Experiment: Apparatus for Parity-Violating Electron Scattering Measurements at Forward and Backward Angles”, Nucl. Instrum. Meth., **A646** 59–86, 2011, (arXiv:1103.0761 [nucl-ex]).
39. D. Androic et al., [G0], “Transverse Beam Spin Asymmetries at Backward Angles in Elastic Electron-Proton and Quasi-elastic Electron-Deuteron Scattering”, Phys. Rev. Lett., **107** 022501, 2011, (arXiv:1103.3667 [nucl-ex]).
40. D. Androic et al., [G0], “Measurement of the parity-violating asymmetry in inclusive electroproduction of π^- near the Δ^0 resonance”, Phys. Rev. Lett., **108** 122002, 2012, (arXiv:1112.1720 [nucl-ex]).
41. M. J. Musolf, T. W. Donnelly, J. Dubach, S. J. Pollack, S. Kowalski and E. J. Beise, “Intermediate-energy semileptonic probes of the hadronic neutral current”, Phys. Rept., **239** 1–178, 1994, (arXiv:nucl-th/9307022).
42. K. S. Kumar and P. A. Souder, “Strange quarks and parity violation”, Prog. Part. Nucl. Phys., **45** S333–S395, 2000.
43. V. E. Lyubovitskij, P. Wang, T. Gutsche and Amand Faessler, “Strange nucleon form-factors in the perturbative chiral quark model”, Phys. Rev., **C66** 055204, 2002, (arXiv:hep-ph/0207225).
44. K. S. Kumar, S. Mantry, W. J. Marciano and P. A. Souder, “Low Energy Measurements of the Weak Mixing Angle”, Ann. Rev. Nucl. Part. Sci., **63** 237–267, 2013, (arXiv:1302.6263 [hep-ex]).
45. F. E. Maas and K. D. Paschke, “Strange nucleon form-factors”, Prog. Part. Nucl. Phys., **95** 209–244, 2017.
46. S. Abrahamyan et al., “Measurement of the Neutron Radius of ^{208}Pb Through Parity-Violation in Electron Scattering”, Phys. Rev. Lett., **108** 112502, 2012, (arXiv:1201.2568 [nucl-ex]).
47. S. Abrahamyan et al., [HAPPEX, PREX], “New Measurements of the Transverse Beam Asymmetry for Elastic Electron Scattering from Selected Nuclei”, Phys. Rev. Lett., **109** 192501, 2012, (arXiv:1208.6164 [nucl-ex]).
48. P. L. Anthony et al., [SLAC E158], “Observation of parity nonconservation in Moller scattering”, Phys. Rev. Lett., **92** 181602, 2004, (arXiv:hep-ex/0312035).
49. P. L. Anthony et al., [SLAC E158], “Precision measurement of the weak mixing angle in Moller scattering”, Phys. Rev. Lett., **95** 081601, 2005, (arXiv:hep-ex/0504049).
50. D. Wang et al., [PVDIS], “Measurement of parity violation in electronquark scattering”, Nature, **506**(7486) 67–70, 2014.
51. J. Benesch et al., [MOLLER], “The MOLLER Experiment: An Ultra-Precise Measurement of the Weak Mixing Angle Using Møller Scattering”, 2014, (arXiv:1411.4088 [nucl-ex]).
52. J. P. Chen, H. Gao, T. K. Hemmick, Z. E. Meziani and P. A. Souder, [SoLID], “A White Paper on SoLID (Solenoidal Large Intensity Device)”, 2014, (arXiv:1409.7741 [nucl-ex]).
53. R. Milner, R. Carlini and F. Maas, “Proceedings, Workshop to Explore Physics Opportunities with Intense, Polarized Electron Beams up to 300 MeV”, AIP Conf. Proc., **1563** pp.1–280, 2013.
54. R. Carlini, “The Qweak Experiment at JLab”, Conference Talk, PANIC2017, Beijing, Sept. 1 - 5, 2017.
55. J. Erler, C. J. Horowitz, S. Mantry and P. A. Souder, “Weak Polarized Electron Scattering”, Ann. Rev. Nucl. Part. Sci., **64** 269–298, 2014, (arXiv:1401.6199 [hep-ph]).
56. M. N. Rosenbluth, “High Energy Elastic Scattering of Electrons on Protons”, Phys. Rev., **79** 615–619, 1950.
57. M. Gorchtein, H. Spiesberger and X. L. Zhang, “How strange is pion electroproduction?”, Phys. Lett., **B752** 135–145, 2016, (arXiv:1509.08780 [nucl-th]).
58. J. C. Bernauer, “Measurement of the elastic electron-proton cross section and separation of the electric and magnetic form factor in the Q^2 range from 0.004 to $1(\text{GeV}/c)^2$ ”, PhD thesis, JGU Mainz, 2010.
59. M. A. El Yakoubi, “Contribution du quark étrange à la structure électromagnétique du nucléon: Les résultats de l’expérience PVA4 à $Q^2 = 0.23 (\text{GeV}/c)^2$ ”, PhD thesis, Université Paris Sud - Paris XI, 2007.
60. S. Galster, H. Klein, J. Moritz, K. H. Schmidt, D. Wegener and J. Bleckwenn, “Elastic electron-deuteron scattering and the electric neutron form factor at four-momentum transfers $5\text{fm}^{-2} < q^2 < 14\text{fm}^{-2}$ ”, Nucl. Phys., **B32** 221–237, 1971.
61. P. Wang, D. B. Leinweber, A. W. Thomas and R. D. Young, “Strange magnetic form factor of the proton at $Q^{*2} = 0.23-1 \text{ GeV}^{*2}$ ”, Phys. Rev., **C79** 065202, 2009, (arXiv:0807.0944 [hep-ph]).
62. P. Larin, “Voruntersuchungen für ein Präzisionsexperiment zur Messung der schwachen Ladung des Protons”, Bachelor thesis, JGU Mainz, 2011.

63. B. Kubis and R. Lewis, “*Isospin violation in the vector form factors of the nucleon*”, Phys. Rev., **C74** 015204, 2006, (arXiv:nuc1-th/0605006).
64. D. Androic et al., [QWeak], “*First Determination of the Weak Charge of the Proton*”, Phys. Rev. Lett., **111**(14) 141803, 2013, (arXiv:1307.5275 [nucl-ex]).
65. V. Tioukine and K. Aulenbacher, “*Operation of the MAMI accelerator with a Wien filter based spin rotation system*”, Nucl. Instrum. Meth., **A 568** 537–542, 2006.
66. J. Grames et al., Two Wien filter spin flipper, In *Proceedings of 2011 Particle Accelerator Conference, New York, NY, USA*, pages 862–865, (2011).
67. S. Friederich and K. Aulenbacher, Test electron source for increased brightness emission by near band gap photoemission, In *Proceedings of IPAC2015, Richmond, VA, USA*, pages 1512–1514. JACOW, 2015.
68. K. Aulenbacher et al., “*The MAMI source of polarized electrons*”, Nucl. Instrum. Meth., **A 391** 498–506, 1997.
69. K. Aulenbacher, “*Polarized beams for electron accelerators*”, Eur. Phys. J. Special topics, **198** 361–380, 2011.
70. K. Aulenbacher, *Erzeugung intensiver hochpolarisierter Elektronenstrahlen mit hoher Symmetrie unter Helizitätswechsel*. Shaker Verlag Aachen, 2006.
71. K. Aulenbacher, I. Alexander, E. Riehn and V. Tioukine, “*High average photocurrent research at MAMI*”, J. Phys. Conf. Ser., **298** 012019, 2011.
72. K. Aulenbacher, I. Alexander and V. Tioukine, “*The polarimetry chain for the P2 experiment*”, Nuovo Cim., **C035N04** 186–191, 2012.
73. A. Gellrich, K. Jost and J. Kessler, “*Elimination of instrumental asymmetries in electron polarization analysis*”, Review of Scientific Instruments, **61**(11) 3399–3404, 1990.
74. A. Gellrich and J. Kessler, “*Precision measurement of the Sherman asymmetry function for electron scattering from Gold*”, Phys. Rev. A, **43** 204–216, 1991.
75. S. Mayer, T. Fischer, W. Blaschke and J. Kessler, “*Calibration of a Mott electron polarimeter: Comparison of different methods*”, Review of Scientific Instruments, **64**(4) 952–957, 1993.
76. M. Steigerwald, *Polarisationsanalyse des Elektronenstrahls der MAMI-Quelle polarisierter Elektronen mittels Mott-Streuung*, Diploma thesis, JGU Mainz, 1994.
77. M. Molitor, *Präzisionsmessung der Strahlpolarisation für das P2 Experiment an MESA mittels Doppel-Mott-Streuung*, Phd thesis (in preparation), JGU Mainz, 2018.
78. H. Hopster and D. L. Abraham, “*New method for accurate calibration of an electron-spin polarimeter*”, Review of Scientific Instruments, **59**(1) 49–51, 1988.
79. V. Tioukine, K. Aulenbacher and E. Riehn, “*A Mott polarimeter operating at MeV electron beam energies*”, Review of Scientific Instruments, **82**(3) 033303, 2011.
80. M. A. Khakoo, D. Roundy, C. Hicks, N. Margolis, E. Yeung, A. W. Ross and T. J. Gay, “*Monte Carlo studies of Mott scattering asymmetries from gold foils*”, Phys. Rev. A, **64** 052713, Oct 2001.
81. K. Aulenbacher and V. Tioukine, Ab initio calculations of effective Sherman functions in MeV Mott scattering, In D.G. Crabb, D.B. Day, S. Liuti, X Zheng, M. Poelker and Y. Prok, editors, *AIP conference proceedings 1149: 18th International Spin Physics Symposium, Charlottesville Virginia 6.- 11. October 2008*, pages 1155–1159, Berlin, Heidelberg, New York, (2008). Springer.
82. X. Roca-Maza, “*Theoretical calculations for precision polarimetry based on Mott scattering*”, ArXiv 1710.0863, 2017.
83. M. Steigerwald, MeV Mott polarimetry at Jefferson Lab, In Nakano T., I. K. Hatanaka K., editor, *AIP Conference Proceedings 570: 14th International Spin Physics Symposium, Osaka, Japan 16-21 October 2000*, page 935, Berlin, Heidelberg, New York, (2001). AIP.
84. E. Chudakov and V. Luppov, “*Møller polarimetry with atomic hydrogen targets*”, IEEE Trans. Nucl. Sci., **51** 1533–1540, 2004.
85. M. Mertig et al., “*Continuous density measurements of atomic hydrogen by means of a bolometer*”, Rev. Sci. Instrum., **62**,1 251–252, 1991.
86. M. Hauger et al., “*A High precision polarimeter*”, Nucl. Instrum. Meth. A, **462** 382, 1994.
87. L.G. Levchuk, “*The Intraatomic motion of bound electrons as a possible source of a systematic error in electron beam polarization measurements by means of a Moller polarimeter*”, Nucl. Instrum. Meth. A, **345** 496, 1994.
88. S. Baunack, *Einzelspin-Asymmetrien in der elastischen Elektron-Proton-Streuung und die Beiträge der Strange-Quarks zu den Formfaktoren des Nukleons*, PhD thesis, JGU Mainz, 2006.
89. S. D. Covrig et al., “*The Cryogenic target for the G0 experiment at Jefferson Lab*”, Nucl. Instrum. Meth., **A551** 218–235, 2005, (arXiv:nuc1-ex/0502019).
90. S. D. Covrig, “*Cryotargets for PVES Experiments*”, invited talk, Physics beyond SM Workshop, ECT-Trento, 2016.
91. S. Agostinelli et al., [GEANT4], “*GEANT4: A Simulation toolkit*”, Nucl. Instrum. Meth., **A506** 250–303, 2003.
92. J. Allison et al., “*Geant4 developments and applications*”, IEEE Trans. Nucl. Sci., **53** 270, 2006.
93. J. Allison et al., “*Recent developments in GEANT4*”, Nucl. Instrum. Meth., **A835** 186–225, 2016.
94. C. M. Poole, I. Cornelius, J. V. Trapp and C. M. Langton, “*A CAD interface for GEANT4*”, Australas. Phys. Eng. Sci. Med, **35**(3) 329–334, Sep 2012.
95. J. Ritman, [FOPI], “*The FOPI detector at SIS/GSI*”, Nucl. Phys. Proc. Suppl., **44** 708–715, 1995.
96. M. Hoek, [PANDA Cherenkov], “*Tailoring the radiation hardness of fused silica*”, Nucl. Instrum. Meth., **A639** 227–230, 2011.
97. M. Hoek et al., “*Radiation hardness study on fused silica*”, Nucl. Instrum. Meth., **A595** 190–193, 2008.
98. T. Allison et al., [QWeak], “*The Q_{weak} experimental apparatus*”, Nucl. Instrum. Meth., **A781** 105–133, 2015, (arXiv:1409.7100 [physics.ins-det]).
99. I. Peric, “*A novel monolithic pixelated particle detector implemented in high-voltage CMOS technology*”, Nucl. Instrum. Meth., **A582** 876–885, 2007.
100. I. Peric and C. Takacs, “*Large monolithic particle pixel detector in high-voltage CMOS technology*”, Nucl. Instrum. Meth., **A624**(2) 504 – 508, 2010.
101. I. Peric, C. Kreidl and P. Fischer, “*Particle pixel detectors in high-voltage CMOS technology—New achievements*”, Nucl. Instrum. Meth., **A650** 158–162, 2010.
102. I. Peric, “*Active pixel sensors in high-voltage CMOS technologies for ATLAS*”, JINST, **7** C08002, 2012.
103. I. Peric et al., “*High-voltage pixel detectors in commercial CMOS technologies for ATLAS, CLIC and Mu3e experiments*”, Nucl. Instrum. Meth., **A731** 131–136, 2013.

104. A. Blondel et al., “*Research Proposal for an Experiment to Search for the Decay $\mu \rightarrow eee$* ”, 2013, (arXiv:1301.6113 [physics.ins-det]).
105. S. Shrestha, “*The High-Voltage Monolithic Active Pixel Sensor for the Mu3e Experiment*”, PoS, **TIPP2014** 047, 2014.
106. H. Augustin et al., “*The MuPix high voltage monolithic active pixel sensor for the Mu3e experiment*”, JINST, **10**(03) C03044, 2015.
107. H. Augustin et al., “*The MuPix System-on-Chip for the Mu3e Experiment*”, Nucl. Instrum. Meth., **A845** 194–198, 2017, (arXiv:1603.08751 [physics.ins-det]).
108. H. Augustin et al., “*Irradiation study of a fully monolithic HV-CMOS pixel sensor design in AMS 180 nm*”, 2017, (arXiv:1712.03921 [physics.ins-det]).
109. M. Müller, *Effizienz eines HV-MAP Sensoren auf niederenergetische Photonen*, Bachelor thesis, JGU Mainz, 2017.
110. N. Berger, S. Dittmeier, L. Henkelmann, A. Herkert, F. Meier Aeschbacher, Y. W. Ng, L. O. S. Noehte, A. Schöning and D. Wiedner, “*Ultra-low material pixel layers for the Mu3e experiment*”, JINST, **11**(12) C12006, 2016, (arXiv:1610.02021 [physics.ins-det]).
111. M. Oinonen et al., ALICE Silicon Strip Detector module assembly with single-point TAB interconnections, In *Proceedings, eleventh Workshop on Electronics for LHC and Future Experiments, Heidelberg, Germany, 12-16 September 2005*, page 15, 2005.
112. L. Feld, M. Fleck, M. Friedrichs, R. Hensch, W. Karpinski, K. Klein, D. Rittich, J. Sammet and M. Wlochal, “*DC-DC powering for the CMS pixel upgrade*”, Nucl. Instrum. Meth., **A732** 493–496, 2013.
113. R. Schwemmer, J. P. Cacheriche, N. Neufeld, C. Soos, J. Troska and K. Wylie, “*Evaluation of 400 m, 4.8 Gbit/s Versatile Link lengths over OM3 and OM4 fibres for the LHCb upgrade*”, JINST, **9** C03030, 2014.
114. R. Martin Lesma, F. Alessio, J. Barbosa, S. Baron, C. Caplan, P. Leitao, C. Pecoraro, D. Porret and K. Wylie, “*The Versatile Link Demo Board (VLDB)*”, JINST, **12**(02) C02020, 2017.
115. C. Soós, S. Détraz, L. Olanterä, C. Sigaud, J. Troska, F. Vasey and M. Zeiler, “*Versatile Link PLUS transceiver development*”, JINST, **12**(03) C03068, 2017.
116. I. Sorokin, “*Parameterization-based tracking for the P2 experiment*”, EPJ Web Conf., **150** 00012, 2017.
117. V. Blobel, C. Kleinwort and F. Meier, “*Fast alignment of a complex tracking detector using advanced track models*”, Comput. Phys. Commun., **182** 1760–1763, 2011, (arXiv:1103.3909 [physics.ins-det]).
118. C. Kleinwort, “*General Broken Lines as advanced track fitting method*”, Nucl. Instrum. Meth., **A673** 107–110, 2012, (arXiv:1201.4320 [physics.ins-det]).
119. N. Berger, A. Buniatyan, P. Eckert, F. Förster, R. Gredig, O. Kovalenko, M. Kiehn, R. Philipp, A. Schöning and D. Wiedner, “*Multiple Coulomb Scattering in Thin Silicon*”, JINST, **9** P07007, 2014, (arXiv:1405.2759 [physics.ins-det]).
120. M. Gorchtein, C. J. Horowitz and M. J. Ramsey-Musolf, “*Model-dependence of the γZ dispersion correction to the parity-violating asymmetry in elastic ep scattering*”, Phys. Rev., **C84** 015502, 2011, (arXiv:1102.3910 [nucl-th]).
121. J. Erler and S.-F. Su, “*The Weak Neutral Current*”, Prog. Part. Nucl. Phys., **71** 119–149, 2013, (arXiv:1303.5522 [hep-ph]).
122. J. Erler, A. Kurylov and M. J. Ramsey-Musolf, “*The Weak charge of the proton and new physics*”, Phys. Rev., **D68** 016006, 2003, (arXiv:hep-ph/0302149).
123. J. Erler and M. J. Ramsey-Musolf, “*The Weak mixing angle at low energies*”, Phys. Rev., **D72** 073003, 2005, (arXiv:hep-ph/0409169).
124. J. Erler and R. Ferro-Hernández, “*Weak Mixing Angle in the Thomson Limit*”, 2017, (arXiv:1712.09146 [hep-ph]).
125. A. Czarnecki and W. J. Marciano, “*Polarized Moller scattering asymmetries*”, Int. J. Mod. Phys., **A15** 2365–2376, 2000, (arXiv:hep-ph/0003049).
126. W. J. Marciano and A. Sirlin, “*Radiative corrections to atomic parity violation*”, Phys. Rev., **D27** 552, 1983.
127. W. J. Marciano and A. Sirlin, “*On Some General Properties of the $O(\alpha)$ Corrections to Parity Violation in Atoms*”, Phys. Rev., **D29** 75, 1984, [Erratum: Phys. Rev. D31,213(1985)].
128. M. J. Musolf and B. R. Holstein, “*Electroweak corrections to parity violating neutral current scattering*”, Phys. Lett., **B242** 461–466, 1990.
129. M. Gorchtein and C. J. Horowitz, “*Dispersion gamma Z-box correction to the weak charge of the proton*”, Phys. Rev. Lett., **102** 091806, 2009, (arXiv:0811.0614 [hep-ph]).
130. A. Sibirtsev, P. G. Blunden, W. Melnitchouk and A. W. Thomas, “*gamma-Z corrections to forward-angle parity-violating e-p scattering*”, Phys. Rev., **D82** 013011, 2010, (arXiv:1002.0740 [hep-ph]).
131. B. C. Rislow and C. E. Carlson, “*Contributions from γZ box diagrams to parity violating elastic ep scattering*”, Phys. Rev., **D83** 113007, 2011, (arXiv:1011.2397 [hep-ph]).
132. P. G. Blunden, W. Melnitchouk and A. W. Thomas, “*New formulation of gamma-Z box corrections to the weak charge of the proton*”, Phys. Rev. Lett., **107** 081801, 2011, (arXiv:1102.5334 [hep-ph]).
133. N. L. Hall, P. G. Blunden, W. Melnitchouk, A. W. Thomas and R. D. Young, “*Quark-hadron duality constraints on γZ box corrections to parity-violating elastic scattering*”, Phys. Lett., **B753** 221–226, 2016, (arXiv:1504.03973 [nucl-th]).
134. H. Q. Zhou, C. W. Kao, S. N. Yang and K. Nagata, “*On the two-boson exchange corrections to parity-violating elastic electron-proton scattering*”, Phys. Rev., **C81** 035208, 2010, (arXiv:0910.3307 [nucl-th]).
135. M. Gorchtein and H. Spiesberger, “*Hadronic weak charges and parity-violating forward Compton scattering*”, Phys. Rev., **C94**(5) 055502, 2016, (arXiv:1608.07484 [nucl-th]).
136. M. E. Peskin and T. Takeuchi, “*A New constraint on a strongly interacting Higgs sector*”, Phys. Rev. Lett., **65** 964–967, 1990.
137. M. E. Peskin and T. Takeuchi, “*Estimation of oblique electroweak corrections*”, Phys. Rev., **D46** 381–409, 1992.
138. C. P. Burgess, S. Godfrey, H. König, D. London and I. Maksymyk, “*A Global fit to extended oblique parameters*”, Phys. Lett., **B326** 276–281, 1994, (arXiv:hep-ph/9307337).

139. H. Davoudiasl, H.-S. Lee and W. J. Marciano, “‘Dark’ Z implications for Parity Violation, Rare Meson Decays, and Higgs Physics”, *Phys. Rev.*, **D85** 115019, 2012, ([arXiv:1203.2947 \[hep-ph\]](#)).
140. X. Roca-Maza, M. Centelles, X. Vinas and M. Warda, “Neutron skin of ^{208}Pb , nuclear symmetry energy, and the parity radius experiment”, *Phys. Rev. Lett.*, **106** 252501, 2011, ([arXiv:1103.1762 \[nucl-th\]](#)).
141. B.P. Abbott et al., [Virgo, LIGO Scientific], “*GW170817: Observation of Gravitational Waves from a Binary Neutron Star Inspiral*”, *Phys. Rev. Lett.*, **119**(16) 161101, 2017, ([arXiv:1710.05832 \[gr-qc\]](#)).
142. A. Carbone, G. Colo, A. Bracco, L.-G. Cao, P. F. Bortignon, F. Camera and O. Wieland, “Constraints on the symmetry energy and on neutron skins from the pygmy resonances in ^{68}Ni and ^{132}Sn ”, *Phys. Rev.*, **C81** 041301, 2010, ([arXiv:1003.3580 \[nucl-th\]](#)).
143. A. Tamii et al., “Complete electric dipole response and the neutron skin in ^{208}Pb ”, *Phys. Rev. Lett.*, **107** 062502, 2011, ([arXiv:1104.5431 \[nucl-ex\]](#)).
144. C. M. Tarbert et al., “Neutron skin of ^{208}Pb from Coherent Pion Photoproduction”, *Phys. Rev. Lett.*, **112**(24) 242502, 2014, ([arXiv:1311.0168 \[nucl-ex\]](#)).
145. J. Zenihiro et al., “Neutron density distributions of Pb-204 , Pb-206 , Pb-208 deduced via proton elastic scattering at $E_p=295\text{ MeV}$ ”, *Phys. Rev.*, **C82** 044611, 2010.
146. B. Klos et al., “Neutron density distributions from antiprotonic Pb-208 and Bi-209 atoms”, *Phys. Rev.*, **C76** 014311, 2007, ([arXiv:nucl-ex/0702016](#)).
147. C. Garcia-Recio, J. Nieves and E. Oset, “Neutron distributions from pionic atoms”, *Nucl. Phys.*, **A547** 473–487, 1992.
148. C. J. Horowitz, S. J. Pollock, P. A. Souder and R. Michaels, “Parity violating measurements of neutron densities”, *Phys. Rev.*, **C63** 025501, 2001, ([arXiv:nucl-th/9912038](#)).
149. C. J. Horowitz, K. S. Kumar and R. Michaels, “Electroweak Measurements of Neutron Densities in CREX and PREX at JLab, USA”, *Eur. Phys. J.*, **A50** 48, 2014, ([arXiv:1307.3572 \[nucl-ex\]](#)).
150. C. J. Horowitz and Z. Lin, private communication, 2015.
151. P. A. Souder et al., PREX-II: Precision parity-violating measurement of the neutron skin of lead, <http://hallaweb.jlab.org/parity/prex/prexII.pdf>, Proposal to Jefferson Lab PAC 38.
152. S. Gardner, W. C. Haxton and B. R. Holstein, “A New Paradigm for Hadronic Parity Nonconservation and its Experimental Implications”, *Ann. Rev. Nucl. Part. Sci.*, **67** 69–95, 2017, ([arXiv:1704.02617 \[nucl-th\]](#)).
153. J. de Vries and U.-G. Meißner, “Violations of discrete space-time symmetries in chiral effective field theory”, *Int. J. Mod. Phys.*, **E25**(05) 1641008, 2016, ([arXiv:1509.07331 \[hep-ph\]](#)).
154. Jiunn-Wei Chen and Xiang-Dong Ji, “Parity violating pion nucleon coupling $h^{*(1)}(\pi N N)$ from π^+ electroproton production near the threshold”, *Phys. Lett.*, **B501** 209–215, 2001, ([arXiv:nucl-th/0011100](#)).
155. Jiunn-Wei Chen and Xiang-Dong Ji, “Measuring the P odd pion nucleon coupling $h_1(\pi NN)$ in π^+ photoproton production near the threshold”, *Phys. Rev. Lett.*, **86** 4239–4242, 2001, ([arXiv:hep-ph/0011230](#)).
156. B. Pasquini and M. Vanderhaeghen, “Resonance estimates for single spin asymmetries in elastic electron-nucleon scattering”, *Phys. Rev.*, **C70** 045206, 2004, ([arXiv:hep-ph/0405303](#)).